An Experimental Study of Aerodynamics and Tip Vortex Generated by Different Wing Platforms under Stationary Ground Proximity

Ge Lin

Supervisor: Prof. Tim Lee

Department of Mechanical Engineering

McGill University

Montreal, Quebec

February 2023

A thesis submitted to McGill University

in partial fulfillment of the requirement of the degree of

Master of Science

Acknowledgements

First of all, I will not proceed so far without Prof. Tim Lee, my supervisor. I would like to thank Prof. Tim Lee for his many advice and guidance. His invaluable knowledge, patience and motivation help me during all times of the research and will greatly influence me in my future career.

Also, I would like to thank my lab mates, James Ni and Tony Yang, for their support and discussion. Last but not least, I am grateful to my parents, my family and my girlfriend, as well as all the friends I met in Canada, for their continuous support and love.

Abstract

The growth and development of the two energetic counterrotating wingtip-generated vortices and their impact on the lift-induced drag and flight hazards are of both fundamental and practical importance. Meanwhile, the large lift increase and lift-induced drag reduction produced by aircraft flying close to the ground, especially during takeoff and landing, have long been recognized. Various ground-effect vehicles utilizing this ground proximity-induced aerodynamic benefits have been designed and constructed. To better understand the impact of ground effect, the aerodynamics and near-field tip vortex flow field behind a rectangular wing (RW), tapered backward swept wing (BSW), and forward swept wing (FSW) in stationary ground effect were investigated experimentally at $Re = 2.48 \times 10^5$, 1.81×10^5, and 1.81×10^5, respectively. The results showed significant lift increase and drag reduction with the reduced ground distance. For the RW and BSW, there was the appearance of a multiple vortex system consisting of a tip vortex, a co-rotating ground vortex, and a counter-rotating secondary vortex. The ground vortex strengthens the tip vortex, whereas the secondary vortex negates its vorticity and causes its rebound. For the FSW, the multiple vortex system was not readily identifiable due to its unique geometry, which always kept the inboard region of the wing in close ground effect while leaving the tip region less affected by the ground effect. The impact of the ground proximity on the trailing vortical flow and the associated lift-induced drag were also discussed in this report. The lift force was computed through the integration of the spanwise circulation distribution, inferred from the crossflow measurement, at selected ground distances, and was found to be in good agreement with the direct wind-tunnel force-balance data, except at $h/c_r < 10\%$, where a significant discrepancy existed due to the secondary vortex. h is the ground distance and c_r is the root chord. Considering its contribution additive, the discrepancy between the lift forces computed and measured with the force balance in close ground proximity became marginal. The aerodynamics and tip vortex measurements of all wing models outside the ground effect were also acquired to serve as a comparison.

Abrégé

La croissance et le développement des deux tourbillons énergétiques contrarotatifs générés en bout d'aile et leur impact sur la traînée induite par la portance et les risques de vol sont d'une importance fondamentale et pratique. Parallèlement, l'augmentation importante de la portance et la réduction de la traînée induite par la portance produites par les aéronefs volant près du sol, en particulier pendant le décollage et l'atterrissage, sont reconnues depuis longtemps. Divers véhicules à effet de sol utilisant ces avantages aérodynamiques induits par la proximité du sol ont été conçus et construits. Afin de mieux comprendre l'impact de l'effet de sol, l'aérodynamique et le champ d'écoulement des tourbillons de bout de champ proche derrière une aile rectangulaire (RW), une aile en flèche vers l'arrière (BSW) et une aile en flèche vers l'avant (FSW) dans un effet de sol stationnaire ont été étudiés expérimentalement à $Re = 2.48 \times 10^5$, 1.81×10^5 et 1.81×10^5, respectivement. Les résultats ont montré une augmentation significative de la portance et une réduction de la traînée avec la réduction de la distance au sol. Pour le RW et le BSW, on a constaté l'apparition d'un système tourbillonnaire multiple composé d'un tourbillon de pointe, d'un tourbillon de sol en co-rotation et d'un tourbillon secondaire en contre-rotation. Le tourbillon de sol renforce le tourbillon de pointe, tandis que le tourbillon secondaire annule sa vorticité et provoque son rebond. Dans le cas du FSW, le système tourbillonnaire multiple n'était pas facilement identifiable en raison de sa géométrie unique, qui maintenait toujours la région intérieure de l'aile dans un effet de sol proche, tout en laissant la région d'extrémité moins affectée par l'effet de sol. L'impact de la proximité du sol sur l'écoulement tourbillonnaire de fuite et la traînée associée induite par la portance ont été examinés dans ce rapport. La force de portance a été calculée par l'intégration de la distribution de la circulation dans le sens de l'envergure, déduite de la mesure de l'écoulement transversal, à des distances choisies du sol, et s'est avérée en bon accord avec les données directes du bilan de force en soufflerie, sauf à $h/c_r < 10\%$, où un écart significatif existait en raison du tourbillon secondaire. h est la distance au sol et c_r est la corde d'ancrage. Si l'on considère que sa contribution est additive, l'écart entre les forces de portance calculées et mesurées avec la balance de force à proximité du sol devient marginal. Les mesures de l'aérodynamique et du tourbillon de pointe de tous les modèles d'ailes hors effet de sol ont également été acquises pour servir de comparaison.

Table of Contents

List of Symbols

AR = aspect ratio

AR_{eff} = effective aspect ratio

b = wing span

b' = distance between center of vortices

c = wing chord

C_D = total drag coefficient

C_{Di} = lift-induced drag coefficient

C_{Dp} = form drag coefficient

C_L = total lift coefficient

c_t = tip chord

c_r = root chord

D = total drag

D_i = lift-induced drag

h = ground distance

L = total lift

r = vortex radius

r_c = vortex core radius

Re = chord Reynolds number, = cU/ν

S = wing surface

u, v, w = mean axial, transverse, and spanwise velocity

u_c = mean core axial velocity

U = freestream velocity

x, y, z = streamwise, transverse, and spanwise direction

y_c, z_c = vertical and spanwise vortex core location

α = angle of attack

α_{ss} = static-stall angle

Γ = circulation or vortex strength

Γ_c = core circulation

Γ_o = total circulation

ζ = mean streamwise vorticity

ζ_{peak} = peak mean streamwise vorticity

Λ = sweep angle

$\Lambda_{1/4c}$ = sweep angle at a quarter chord

Λ_{LE} = leading edge sweep angle

Λ_{TE} = trailing edge sweep angle

ν = kinematic viscosity

ϕ = velocity potential

Ψ = stream function

v_θ = tangential velocity

$v_{\theta peak}$ = peak tangential velocity

List of Figures

List of Tables

1 Introduction

Energy saving has become increasingly important as global climate change raises concerns to the public. The international council on clean transportation (ICCT) predicted that carbon emissions from commercial flights will triple by 2050, which urges the need for more efficient and greener aircraft designs. In aviation, a majority of the fuel is consumed to overcome drag and provide enough lift to take off. Therefore, the aviation industry has long focused on maximizing lift and minimizing drag in order to increase aircraft efficiency. Lift-induced drag, generated by two energetic counterrotating wingtip vortices, has already been demonstrated to be a significant component of the total drag, placing a particular emphasis on the study of the wingtip vortex.

Significant lift-induced drag reduction and lift increase have long been recognized by pilots flying aircraft close to the ground during takeoff and landing. These ground proximity-induced aerodynamic benefits are referred to as ground effects which are generally categorized as chord-dominated ground effect (CDGE) and span-dominated ground effect (SDGE). The CDGEs reduce air passage under the wing, thereby increasing the wing's sectional lift by creating ram pressure. While the SDGE (the main contributor to lift-induced drag reduction) is concentrated on moving the wingtip vortices outboard and reducing the vortex strength, thus reducing the lift-induced drag. The combination of the CDGE and SDGE led to a significant increase in aerodynamic efficiency.

Various ground-effect vehicles (GEVs) or wing-in-ground effect (WIG) craft have been designed and constructed utilizing the ground effect. Among the most famous WIG crafts is the Russian ekranoplan, also known as the Caspian Sea Monster, which has a rectangular wing platform with a small aspect ratio. Another outstanding WIG craft was designed by German engineer Alexander Lippisch, which has a reverse delta wing (RDW) and a huge T-shape tail. The air-cushion formed underneath the wing builds up the pressure increasing the lift consequently.

In light of these ground effect-induced aerodynamic benefits, the current study focused on the impact of the ground effect on aerodynamics and tip vortices generated behind finite wings. Meanwhile, to explore the feasibility of different wing platforms in WIG craft designs, three conventional wing platforms were adopted in this study: 1) the rectangular wing, 2) the backward swept wing, and 3) the forward swept wing. Rectangular wings are popular among researchers because of their simplicity and abundance of data. They tend to exhibit a root-stall characteristic because the downwash from the wingtip vortex reduces the local effective angle of attack in the tip region. The rectangular wing was, therefore, selected and treated as a baseline wing for the current study. Swept wings have been employed in many modern high-speed aircraft. For transonic flight (in the vicinity of the speed of sound), forward and backward swept wings are employed to delay the onset of drag rise, resulting in an effective decrease in drag divergence. Additionally, many aerial animals sweep their wings forward to produce large lift during slow flights (Thomas and Taylor 2001). It is also common for many species to display forward wings during high-α perching and snatching maneuvers (Manchester et al. 2017). In the case of the backward swept wing (BSW), the outward flowing spanwise flow tends to build up the boundary layer, thereby promoting flow separation in the direction of the wingtips, resulting in highly undesirable tip stalls. (Black 1956, Harper and Maki 1964, El-Ramly et al. 1976, Nangia 1982, Naik and Ostowari 1990, Zhang et al. 2020, and Zhang and Taira 2022). The tip stall-caused separated flow over the ailerons also results in a loss of aileron control, making the design of backward swept wings considerably more challenging than the straight wings.

Compared to a BSW, air flowing over a forward swept wing (FSW) tends to flow inward toward its root rather than outward toward its tip. As demonstrated by the Grumman X-29 experimental aircraft, the stall starts at the inboard region of the FSW, ensuring that the ailerons are effective at a high angle of attack. These characteristics provide high maneuverability and lateral controllability. The forward swept wing, however, suffers from inherent wing structural divergence when operating under a high dynamic pressure condition. This problem can be alleviated via the use of composite materials.

Furthermore, in addition to providing better maneuverability and controllability than the BSW at high speeds, the FSW also offers better aerodynamic performance at very low air speeds. Due to the inboard flow of the FSW, its wingtip vortices are weaker than on the BSW, rendering a lower lift-induced drag. The root stall over the FSW also generates a higher maximum lift coefficient as compared to the BSW. The root stall of the FSW enables a more efficient active control technology using, for example, outboard flaps, compared to its BSW counterpart. In short, even though the swept wings are employed at high-speed flights, the low-speed aerodynamics of such wings during takeoff and landing also demand attention because a large amount of fuel is consumed during these processes.

The next chapter will review the study and works conducted on the wingtip vortices and ground effects (CDGE and SDGE) generated by the three wing platforms, which leads to the objectives of the current research topic.

2 Literature Review

2.1 Wingtip Vortex

The growth and development of the two energetic counterrotating wingtip-generated vortices as well as their impact on the lift-induced drag and flight hazards, are both of fundamental and practical importance. The finite wing is designed to accelerate the viscous fluid flows over the top surface (suction side) and decelerate those on the bottom surface (high-pressure side). Due to this pressure difference, the fluid on the bottom surface separates and escapes from the finite wing's free end (wingtip) and gets sucked into the suction side, which generates a circulatory motion, as shown in Fig. 2-1. As more and more fluid separates from the boundary layer, the rotational field, moving downstream, grows in size and strength, eventually emerging and detaching near the wing's trailing edge, becoming a free vortex (tip vortex). In the event that the fluid flows over the wing surface and passes the trailing edge, the fluid will inevitably separate from the wing, forming a wake behind the wing, and the boundary layer will become a shear layer, which contains a certain level of vorticity. It is the shear layer and the wake that feed the free vortex continuously until its circulation constitutes the majority of the wing’s circulation. By generating a downwash of fluid behind the wing, the tip vortex deflects the total aerodynamic forces rearward, increasing the drag component (lift-induced drag). The lift-induced drag is the most significant impact from the wingtip vortex and is the major concern in aircraft since it generally accounts for 30-40% of the total drag.

Even though the wingtip vortex slowly diffuses with time and distance, it generally persists in hundreds of chord lengths until the effect becomes negligible. However, the vortex parameter and velocity field change significantly in this rollup region, called the near-field region. Consequently, most relevant studies have emphasized the vortex characteristics and velocity field of the wingtip vortex in the near-field region. The most commonly reported vortex parameters are core axial velocity u_c, peak tangential velocity $v_{\theta\text{peak}}$, core radius r_c, vortex radius r_o, peak vorticity ζ_{peak}, core circulation Γ_c, and vortex circulation Γ_o. The typical tangential and axial velocity distributions across the wingtip vortex in the spanwise direction are shown in Fig. 2-2. Among these parameters, the results about the axial velocity u_c showed particular controversy. Experiments demonstrated that the extremum at the core centerline ranged from 0.6 to 1.8. The vortex flow with maximum u_c/U that appeared at the center was defined as jet-like flow (or velocity excess), whereas those with minimum u_c/U at the center were defined as wake-like flow (or velocity deficit).

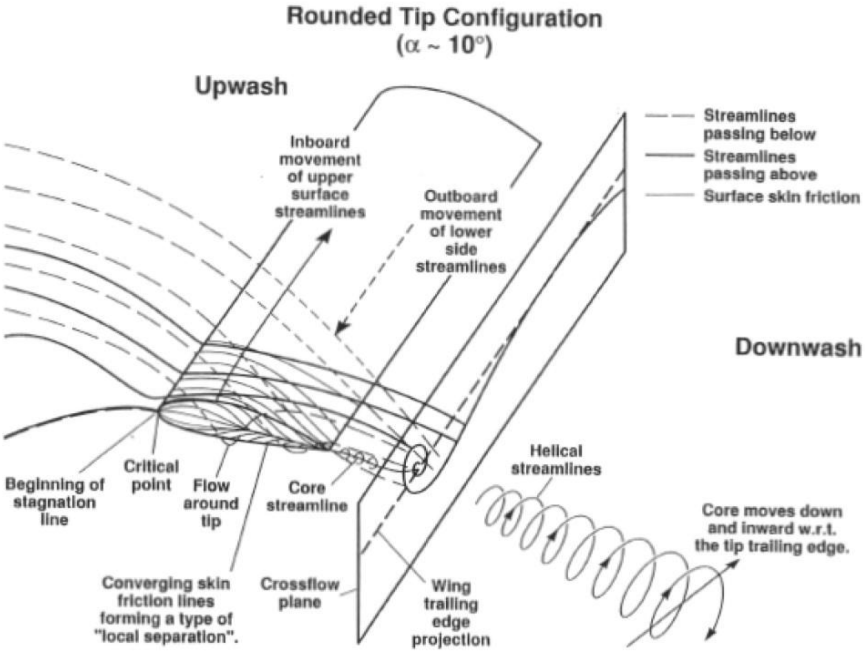

Figure 2-1 Details of formation and development of a wingtip vortex. (Chow et al. 1997)

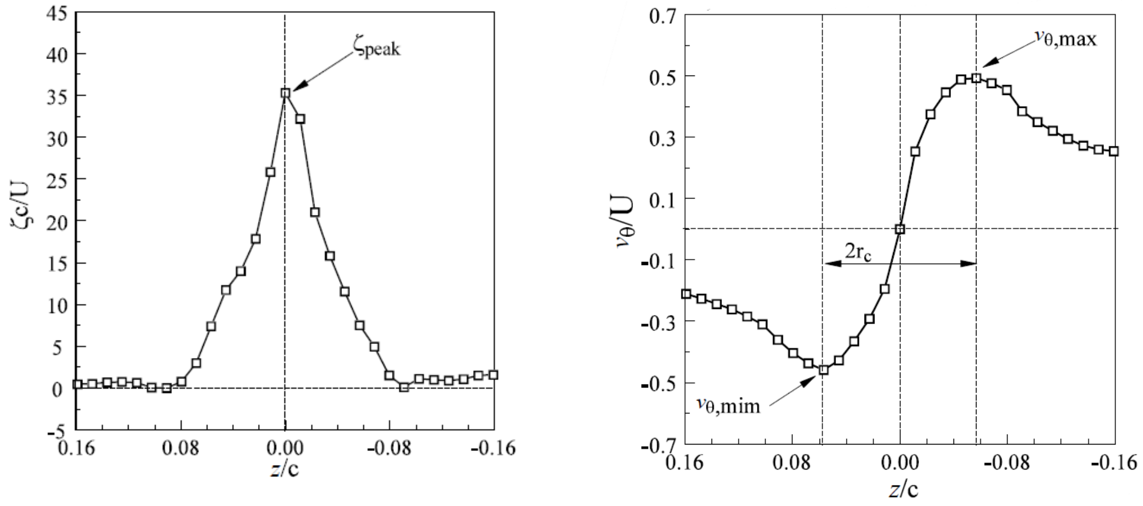
(a) (b)

Figure 2-2 Typical (a) vorticity and (b) tangential velocity distributions across the vortex core.

The following sections will review some of the works conducted regarding the formation and development of the wingtip vortex behind the RW, BSW, and FSW in the near-field region.

2.1.1 Rectangular Wing

Chigier and Corsiglia (1971) conducted an experimental study on the downstream development of the wingtip vortex generated behind a NACA 0015 rectangular wing with AR = 5.33 at Re = 9.53×10^5 and $\alpha = 12°$. The surface pressure measurement showed that the suction from the wingtip vortex shifted the span loading from a nearly elliptic distribution to a more rectangular distribution. The velocity field was measured by a triple-sensor hot-wire probe at several discrete locations starting from x/c = 0 to 5 aft the wing leading edge. The maximum circumferential velocity at midchord (x/c = 0.5) was found to decay rapidly from $v_{\theta\mathrm{peak}}/U = 0.42$ to 0.24 at x/c = 5. Also, the axial velocity u_c peaked ($u_c/U = 1.39$) at x/c = 0.25, followed by a sharp drop to $u_c/U = 1.2$ at x/c = 5, with the core radius expanded from 1.3% c to 7.1% c. The findings demonstrated that the interaction between the wingtip vortex and wake slows down the axial and rotational velocity of the tip vortex in the near-field region. Furthermore, as a result of the inboard movement on the top surface, the vortex moved from the tip toward the root and became axisymmetric at x/c = 5. Later, Corsiglia et al. (1973) measured the velocity field behind a smaller wing with the same airfoil profile and AR from x/c = 0 to 108 aft the wing leading edge at Re = 3×10^5 and $\alpha = 8°$. The maximum tangential velocity $v_{\theta\mathrm{peak}}/U$ dropped from 0.448 to 0.336. However, no significant change in the $u_c/U = 0.8$ was noticed. Ramaprian and Zheng (1973) also studied the wingtip vortex development using a NACA 0015 rectangular wing in the rollup region ($1.33 < x/c < 4.33$) at Re = 1.8×10^5 and $\alpha = 10°$. The velocity components were measured by a three-component Laser Doppler Velocimetry (LDV). Velocity deficit was found at all downstream locations across the tip vortex, which was recovered rapidly from $u_c/U = 0.68$ to 0.74 within one-third of the chord distance. However, the increase slowed down afterward. The axial velocity contour downstream of the trailing edge revealed that the center low-velocity region became increasingly axisymmetric while the outer high-velocity region remained spiral. The vorticity decreased gradually from the maximum at the vortex center to zeros at the outer region with a short distance r = 0.15c, which implied a strong turbulence diffusion at the inner region. As the shear layer continued to feed the wingtip vortex, the combined effect resulted in a small increase in the peak vorticity. Like Chigier and Corsiglia (1971), Ramaprian and Zheng (1973) recognized an inboard and upward movement of the tip vortex.

Following Chigier and Corsiglia, Orloff (1974) investigated the effect of α on the wingtip vortex at a fixed downstream location and Re = 7×10^5. The rectangular wing model tested had a NACA 0015 airfoil with AR = 5.33. The velocity components were measured by a 2D laser velocimeter located at x/c = 3 starting from the wing leading edge. In comparison to hot-wire measurement, the experimental results were more accurate and repeatable due to the high-speed scanning capability and finer grid resolution. It was found that the peak circumferential velocity $v_{\theta\text{peak}}$/U raised linearly with the increasing angle of attack (4° to 12°) from 0.19 to 0.56. Since the core circulation is directly correlated to the tangential velocity, it naturally follows the same trend. Similarly, the tip vortex's core axial velocity u_c/U increased from 0.85 to 1.15 with α from 8° to 12°, which shifted the axial velocity profile from a wake-like profile to a jet-like profile. The point where this shift happens is commonly termed the crossover point. Similarly, McAlister and Takahashi (1991) examined the influence of the angle of attack based on both the pressure and velocity measurement using a NACA 0015 wing at x/c = 7 and Re = 1.5×10^6 with AR = 6.6. u_c/U increased from 0.23 to 0.62, whereas the axial velocity profile behaved as wake-like for all $\alpha < 12°$ with r_c varied from 4 to 5% c. The velocity excess only occurred at $\alpha = 12°$. Birch et al. (2003) also reported that, at Re = 3.25×10^5 and x/c = 1.5, the peak tangential velocity, vorticity and axial velocity increased with increasing incidence from 2 to 16° for both a rectangular wing and a high-lift Bombardier Research and Development wing. The crossover point occurred at $\alpha = 8°$. As the vortex grew spatially in size, the centerline of the vortex core was found to move outboard toward the tip.

McAlister and Takahashi (1973) also studied the effect of Re on the wingtip vortex at three selected Reynolds number conditions: Re = 3.0×10^6, 1.7×10^6, and 1.1×10^6. At x/c = 1.01, the circumferential and axial velocity components increased with the decreasing Re, which consequently changed the axial velocity profile from a wake-like profile to a jet-like profile at x/c = 4. Except that, no significant difference was noticed in the vortex core parameters, which did not prove any dependence on the variation of Re. Similarly, Anderson and Lawton (2003) demonstrated that for NACA 0015 wings with both square and rounded tips at Re = 0.75×10^6, 1×10^6, and 1.25×10^6, the results seemed inconsistent; hence no conclusive statement was made.

In contrast, Birch et al. (2003) spotted that at $\alpha = 12°$, the vortex strength was attenuated, the peak tangential velocity was decreased, and r_c was expanded with an increasing Re from 6.7×10^3 to 3.25×10^5. The vortex strength (Γ/cU) dropped from 0.4 to 0.23.

2.1.2 Backward Swept Wing

Gerontakos and Lee (2006) investigated the near-field wingtip vortex behind a NACA 0015 sweptback and tapered wing with AR = 3.654, taper ratio $\lambda = 0.375$, and swept angle at 1/4 chord location $\Lambda_{1/4c} = 24°$ using the miniature seven-hole pressure probe at Re = 1.81×10^5 and $\alpha = 8°$ for $x/c_r = 1.625 - 4.5$, where c_r is the chord length at the root. For $x/c_r < 1.625$, the vortex was skewed and asymmetric by virtue of the strong spanwise flow. Moving downstream, the degree of axisymmetry became more and more pronounced with nearly unchanged normalized total and core circulation $\Gamma_o/c_rU = 0.11$ and $\Gamma_c/c_rU = 0.07$. The peak vorticity and tangential velocity dropped when the rollup was nearly completed from $x/c_r = 2$ to 4.5, while the core axial velocity deficit fluctuated around $u_c/U = 0.7$. The wake-like axial velocity profile was believed to be caused by the strong spanwise and outboard flow over the upper surface. Gerontakos and Lee (2006) also presented that, at $x/c_r = 3.75$, the normalized peak vorticity and tangential velocity increased moderately from 0.27 to 0.4 and from 32 to 42, respectively, for $4 \le \alpha \le 8$, followed by a drop for $\alpha > 8°$. With the incidence increased, the velocity deficit was first enhanced for $\alpha < 8°$ and reduced for $\alpha \ge 8°$. This was accompanied by the outer vortex size following the same trend while the core vortex size remained unchanged.

A more recent experiment from Skinner et al. (2020) showed similar results with a NACA 63-412 sweptback and tapered wing with AR = 4.12, $\lambda = 0.21$, and $\Lambda = 30°$, attached to a fuselage fairing at Re = 1.5×10^6 and $\alpha = 8°$. The stereoscopic particle image velocimetry (sPIV) was implemented to obtain the velocity field. The peak tangential velocity and vorticity decayed continuously and linearly with the downstream distance from $x/\bar{c} = 1.35$ to 5.418 starting from the aerodynamic center, where $\bar{c}$ is the mean aerodynamic chord length. When moving downstream, the velocity deficits persisted, while the core axial velocity and the total circulation plateaued, in agreement with Gerontakos and Lee's results. At $x/\bar{c} = 2.5$, the peak axial velocity dropped significantly from $u_c/U = 0.39$ at $\alpha = 0°$ to only 0.08 at $\alpha = 4°$ and the deficit recovered for $\alpha > 4°$. At $\alpha < \alpha_{ss} = 8°$, the peak vorticity and tangential velocity increased linearly and levelled off when close to stalling, followed by a rapid drop with ever-increasing α. After stalling, the drop can be attributed to the disorganized and indiscernible tip vortex. Differently, the core vortex size kept increasing with the incidences.

2.1.3 Forward Swept Wing

Breitsamter and Laschka (2001) studied the vortical flow field behind a NACA 64A010 forward swept wing with leading-edge sweep $\Lambda_{LE} = -40°$, trailing-edge sweep $\Lambda_{TE} = -52.2°$, AR = 3.81, and $\lambda = 0.4$ at Re = 0.46×10^6 and $\alpha = 20°$. The velocity field was measured using dual-sensor hot-wire probes at a distance $x/l_w = 0.2$, 0.5, 0.8, and 1.1 downstream from the tip of the leading edge, where l_w is the distance between the two apexes of the wing in the streamwise direction. A jet-like axial velocity profile across the wingtip vortex was found at all downstream locations where the maximum core axial velocity $u_c/U = 1.75$ showed up at $x/l_w = 0.2$. The velocity excess slightly recovered to 1.65 at $x/l_w = 0.5$ and plateaued afterward. Induced by the strong spanwise flow towards the root, the wingtip vortex moved inboard with the vortex size expanded, whereas over a backward swept wing, this deflection is outward. No vorticity and circulation level were reported in the article. Interestingly, a significant, counter-rotating leading-edge vortex was presented next to the wingtip vortex. The formation of the leading-edge vortex can be attributed to the large leading-edge swept angle, which made the forward swept wing behave as a half delta-wing. Breitsamter and Laschka (2001) also illustrated the root-mean-square (rms) values of the axial velocity fluctuation at three different $\alpha = 10°$, 20°, and 30° at $x/l_w = 0.8$. The rms values rose rapidly with the increasing α indicating a strengthened turbulence intensity. The vortex size was also enlarged accordingly.

Lee and Ko (2009) investigated the tip vortex generated behind a NACA 0015 forward swept wing with $\Lambda_{1/4c} = -24°$, AR = 3.654, and $\lambda = 0.375$ at Re = 1.81×10^5 using a miniature seven-hole pressure probe. At $\alpha = 9.6°$, the maximum tangential velocity and peak vorticity remained unchanged ($u_c/U = 0.31$ and $\zeta_{peak}c_t/U = 14.9$) between $x/c_t = 2$ and 5, followed by a slight drop progressing downstream with no noticeable change in the total and core circulation of the tip vortex. Different from Breitsamter and Laschka's result, an axial velocity deficit was found at all downstream locations. Lee and Ko also showed the effect of α on the vortical flow field for $\alpha = 2 - 14°$. Unlike BSW, due to the root stalling mechanism that left the tip vortex unaffected after stalling, the maximum tangential velocity, peak vorticity, core, and total circulation were continuously increased with increasing angle of attack while maintaining a spatially constant core vortex size, leading to persistently increasing lift-induced drag. The core axial velocity dropped slightly from 0.91 at $\alpha = 2°$ to 0.84 at $\alpha = 6°$ and increased very slowly between $\alpha = 6°$ and 12°.

Many experimental studies have recognized and called attention to a major source of error in the result, which is the meandering(wandering) of the wingtip vortex. The wandering was acknowledged to be blamed on either the wing vibration (Westphal and Mehta 1989) or the freestream turbulence intensity (Chigier and Corsiglia 1973, Zheng and Ramaprian 1991, and Devenport et al. 1996). Westphal and Mehta investigated the meandering of the wingtip vortex generated behind a half delta-wing using hot-wire anemometer at $Re = 6.15 \times 10^4$ and $\alpha = 12°$. For the stationary wing, the vorticity contour appeared circular, and no significant wandering was observed at $x/c = 26.3$. When the vortex generator was forced to oscillate linearly in the spanwise direction, the time-averaged vertical velocity increased by a factor of 2 and the vorticity contour was distorted dramatically. However, at a further downstream distance ($x/c = 65.8$), the difference between the two cases was not observable due to the diffusion. Whereas, in 1973, Chigier and Corsiglia examined the wingtip vortex movement behind a stationary NACA 0015 wing by analyzing each frame from the movie film of the smoke visualization. No dominant frequency was found in the wandering, which led to the conclusion that the meandering resulted from the freestream turbulence. Recent research on the isolated wingtip vortex showed that the wandering can be due to the instability of the vortex itself. Adam et al. suggested that the transverse velocity at the centerline of the vortex was not zero due to its azimuthal instability, which displaced the trailing vortex in the radial direction regardless of the wind-tunnel condition. While the underlying mechanism of the meandering remained unclear, the method to correct the error is urged. In 1996, Devenport et al. first proposed a theoretical method to take the time mean average of the velocity components to smoothen the meandering effect resulting in a Gaussian distribution using which to analyze the laminar q-vortex. With modern technology, for example, particle image velocimetry (PIV), the wandering effect can be diminished by localizing the instantaneous vortex core and spatially adjusting the velocity vector field accordingly (Ramasamy et al. 2009 and Skinner et al. 2020).

2.2 Chord-dominated Ground Effect (CDGE)

As mentioned in the introduction, the pilots have observed a significant lift increase and lift-induced drag reduction during takeoff and landing. It is the chord-dominated ground effect that causes the large lift increase by increasing the ram pressure built-up underneath the airfoil. Extensive investigations have been conducted on the aerodynamics of 2D airfoils in ground effect (IGE). Some of the studies and works are summarized in the following.

Hsiun and Chen (1996) reported the aerodynamic characteristic of a NACA 4412 airfoil at $\alpha = 5°$ and 10° with the stationary ground condition. Surprisingly, for $\alpha = 5°$ at $Re = 2 \times 10^6$, $C_l = 0.86$ (far above the ground) continuously rose to 0.97 at $h/c = 0.25$, whereas, at $\alpha = 10°$, the increase was very gradual and ended at $h/c = 1$. For both cases, C_l dropped significantly at $h/c = 0.05$ after reaching the peak. The increase in C_l mainly resulted from the enhanced positive pressure on the bottom side. By examining the flow field around the airfoil at the extreme ground distance ($h/c = 0.05$), it was found that there existed a recirculation zone under the leading edge of the wing due to the stationary ground condition. A convergent-divergent passage formed between the wing’s bottom surface and the ground as a result of the recirculation zone, causing the pressure on the lower surface to decrease, which is one of the main reasons for the reduction of C_l. The other factor was the increasing adverse pressure in ground proximity which pushed the separation point toward the leading edge and decreased the suction force on the upper surface. The difference between cases with $\alpha = 5°$ and 10° was because the loss in the suction force at $\alpha = 10°$ was more significant. The ground effect also reduced C_d continuously for both α. Above $h/c = 0.05$, the pressure on the top surface increased with reduced ground clearance. Consequently, C_d was reduced. For extreme ground distance, the reduced pressure on the bottom surface further minimized the pressure difference between the two surfaces resulting in a sharp reduction in C_d. The effect of Re on the airfoil in the ground effect was also investigated by Hsiun and Chen. It was found that the increasing Re improved C_l while decreasing C_d continuously, with the effect being more apparent when the ground distance was small.

Ahmed et al. (2007) also conducted an experimental study on the aerodynamic characteristics of a NACA 4412 airfoil in ground effect but with a moving ground achieved by a moving belt system. The flow field measurements were taken using a YAG laser-based PIV system in a wind tunnel at $Re = 3.0 \times 10^5$ for various $\alpha = 0° - 10°$. For low angle of attack ($\alpha \leq$

4°), C_l decreased gradually with the reducing ground clearance. The pressure on the lower surface indeed increased when approaching the ground. However, a more significant loss in the suction force on the upper surface eventually led to a reduction in C_l value. For higher $\alpha \geq 6°$, the blockage started to produce a much more considerable pressure increase on the pressure side in ground proximity which prevailed over the loss on the suction side, resulting in C_l increase. The sectional drag C_d was reported to increase for all α with reducing ground distance and the slopes were found to be shaper at higher $\alpha = 6° - 10°$ in close ground proximity due to the stronger pressure build-up on the lower surface.

Qu et al. (2015) further investigated the effect of various $\alpha = -4°$ to 20° on the aerodynamic performance of a NACA 4412 airfoil in ground effect numerically with moving ground at $Re = 6 \times 10^6$ and for h/c = 0.05, 0.1, 0.2, 0.4, 0.6, 0.8, 1, and ∞. For low-to-moderate $\alpha = 2°$ to 12°, in general, C_l first decreased gradually with reducing ground distance (region II), followed by a sharp increase in C_l value (region I; see Fig. 2-3). Qu et al. (2015) attributed the changes in C_l to the decrease in the effective α (increased the pressure on the suction side and decreased the pressure on the lower side) and the blockage effect (increased the pressure on the lower surface). In region II, the reduction in the effective α dominated the airflow blockage effect resulted in a negative lift increment. When the airfoil moved closer to the ground entering region I, the blocking effect became much stronger, contributing to a positive lift increment. The higher the α was, the smaller the ground distance that switched from region II to region I was. For high $\alpha > 12°$, the airflow started to separate, and the separated region expanded as the adverse pressure gradient increased with reducing ground distance. The pressure increased on the upper surface due to the flow separation being so huge that the C_l increment was found to be negative for all ground distances resulting in a decreasing C_l value when the airfoil was approaching the ground. Also, the wing stalling was observed to be earlier and steeper in closer h/c because of the stronger adverse pressure gradient in ground proximity.

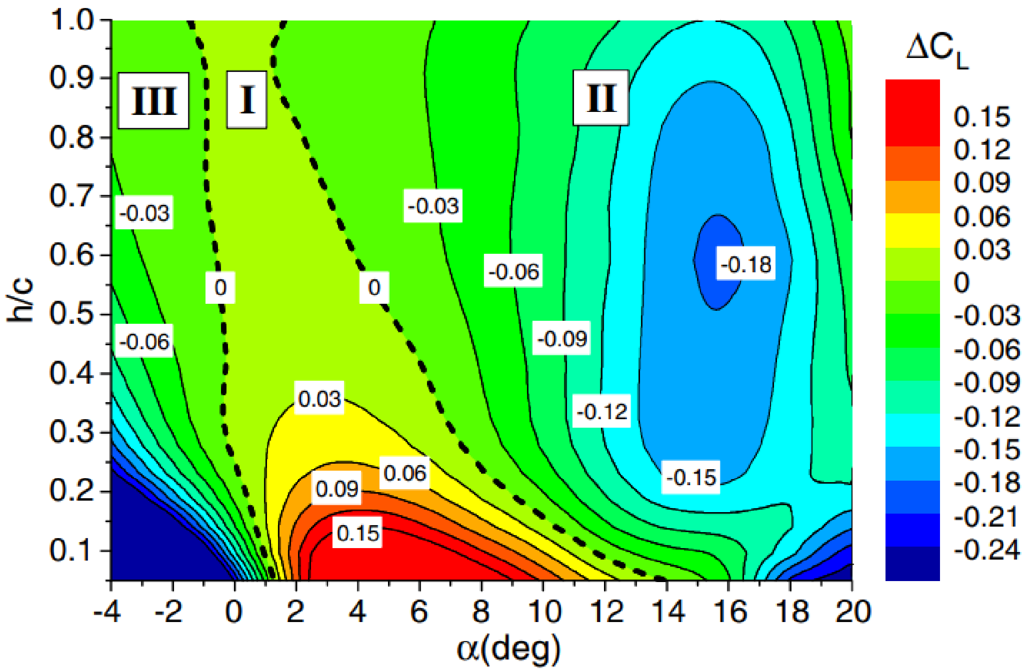

Figure 2-3 Lift increment contour based on total airfoil surface. (Qu et al. 2015)

The enlarged separation region was reported in Hayashi and Endo (1978)'s work as well. They investigated the wake of a NACA 4412 airfoil at α = 15° (post-stalling) and Re = 3.2×10^5 both experimentally and numerically. The wake region expanded massively as the ground approached, and the stalling occurred much earlier than the outside ground effect (OGE) counterpart, which matched the results from Qu et al. (2015).

In light of the discrepancies in ground effect results presented in previous studies with different ground conditions, Barber et al. (2002) investigated four ground conditions. Besides the stationary ground and moving ground conditions, another two conditions were 1) zero shear stress at the boundary, also known as the 'slip' boundary condition, and 2) 'image' ground condition where two identical bodies were modelled with a plane of symmetry which represented the ground. In order to validate Hsiun and Chen (1996)'s work, numerical and experimental works were carried out adopting the same NACA 4412 airfoil with α = 2.9° at Re = 8.2×10^6. The velocity profile with stationary boundary condition at h/c = 0.025 clearly showed a recirculation zone underneath the leading edge (Fig. 2-4), which matched the observation from Hsiun and Chen's work. Similar effects were found using the image boundary condition, which resulted from the stagnation points at the flow field intersection. No recirculation zone was found in the slip or moving ground conditions (Fig. 2-4). Above h/c = 0.25, all conditions showed similar sectional lift coefficient C_l increase. The discrepancy appeared below h/c = 0.1, in which C_l value started to drop with the stationary ground while the value from the rest three models continued to rise with a slight difference in the peak values. As for the drag curve, the sectional drag coefficient C_d with fixed ground dropped continuously same as the results presented in the previous work. On the contrary, C_d for the remaining models began to increase below h/c = 0.1 after a gradual decrease. Another important result reported was the sectional lift-to-drag ratio l/d curve, where the ratio continuously rose in the ground stationary model while the rest models predicted a slight decrease after the peak value at h/c = 0.05. The numerical results were supported by the PIV measurements at $Re = 6.1 \times 10^4$ in a channel flow.

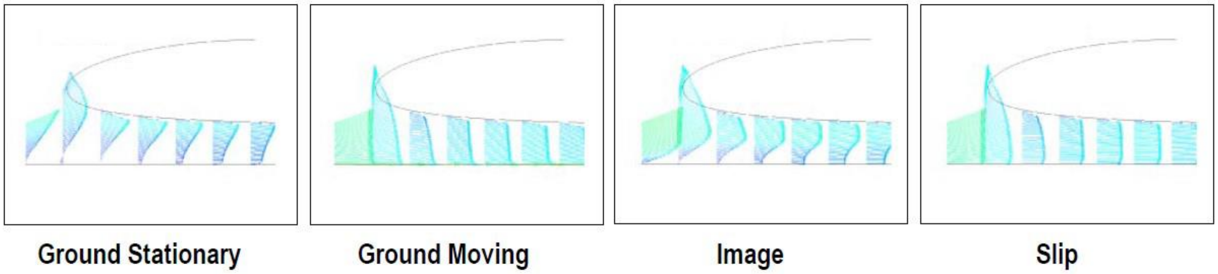

Figure 2-4 Simulated velocity profile around NACA 4412 airfoil under different boundary conditions, h/c = 2.5%, $Re = 8.2 \times 10^6$. (Barber et al. 2002)

Tremblay-Dionne and Lee (2021) measured the flow field around a NACA 0012 airfoil and the associated aerodynamic characteristics in ground effect using a PIV system at $Re = 9.2 \times 10^4$ and from $\alpha = 1°$ to 9°. Two different ground conditions were tested: stationary ground and moving ground simulated using a moving belt system. By examining the velocity contour at $\alpha = 9°$ and h/c = 5%, a recirculation zone was clearly observed in the fixed ground test, whereas it was absent in the moving ground test (Figs. 2-5a-e). For $\alpha > 3°$, both grounds increased C_l value by approaching the wing. For h/c > 15%, the fixed ground produced higher C_l due to the longitudinal boundary layer roll-up on the stationary ground surface, further blocking the airflow and increasing the flow deceleration underneath the airfoil. However, for h/c < 15%, as a result of the formation of the ground vortex (recirculation zone) with the stationary ground, the flow was accelerated due to the convergent-divergent passage, decreasing the pressure on the lower surface, resulting in a lower C_l value than with the moving ground. As for $\alpha < 3°$, C_l started to drop below h/c = 15% in both ground conditions, which was attributed to the airfoil-shape-induced convergent-divergent passage leading to an unusual suction pressure on the lower surface. Similar to Qu et al. (2015)'s result, in ground proximity, the suction peak at the leading edge increased while the suction pressure at the trailing edge decreased, which promoted an earlier flow separation. The moving ground effect generated a larger near wake and C_d than the stationary ground effect, suggesting an earlier flow separation. Both moving and stationary

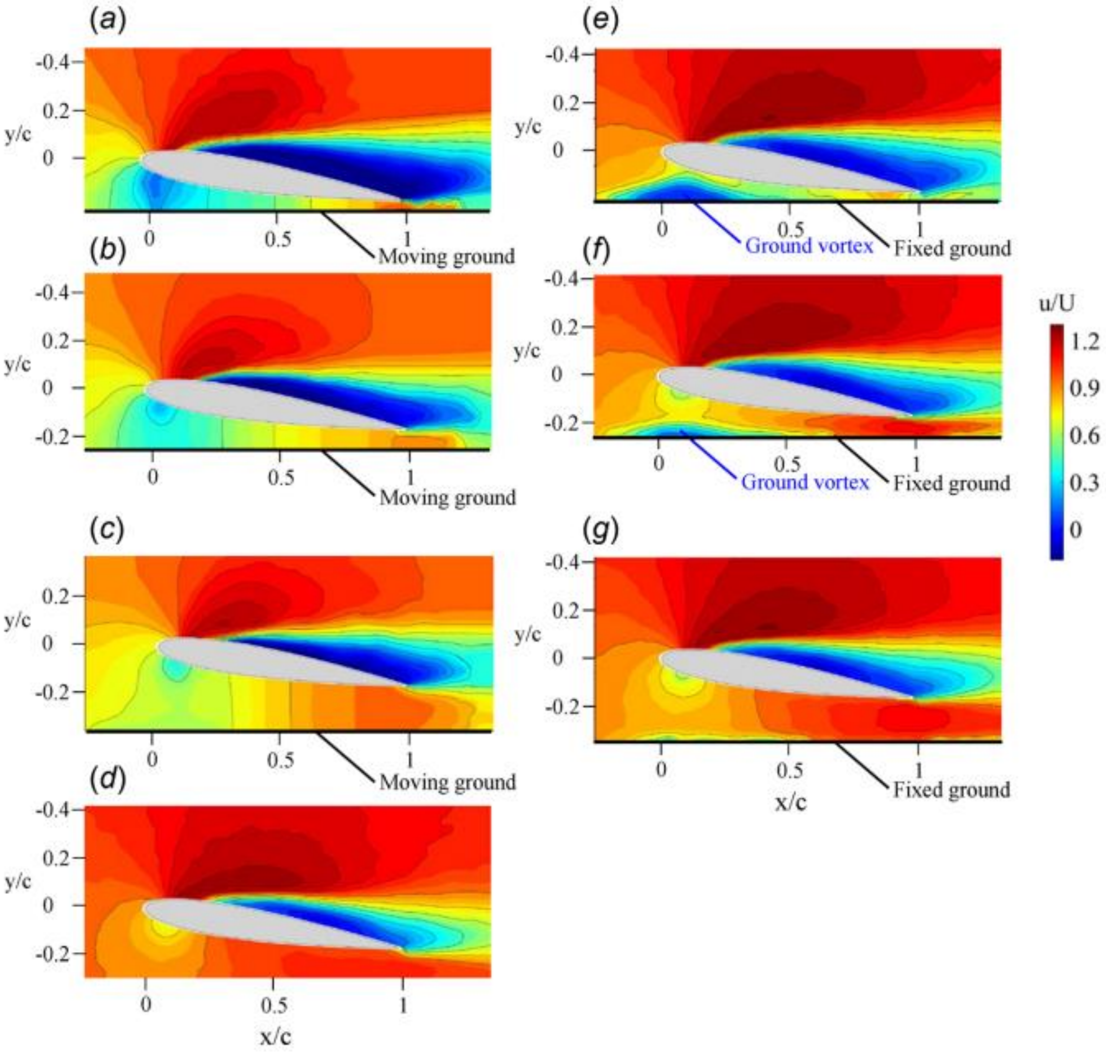

Figure 2-5 Impact of ground boundary condition on the iso-u/U contour at α = 9°. Moving ground: (a) h/c = 5%, (b) h/c = 10%, and (c) h/c = 20%. Fixed ground: (e) h/c = 5%, (f) h/c = 10%, and (g) h/c = 20%. (d) OGE. (Tremblay-Dionne and Lee 2021)

ground proximity pushed the stagnation point on the lower surface toward the trailing edge, with a larger movement found in the moving ground case. C_d was found to continuously increase when approaching the ground for all α due to the increased ram pressure and increase significantly when h/c is lower than 20%. At low $\alpha \leq 3°$, both grounds produced similar C_d. For $3° < \alpha < 9°$, C_d value was slightly higher in the fixed ground condition for h/c > 10%, while it was the opposite for h/c ≤ 10%.

2.3 Span-dominated Ground Effect (SDGE)

Now, after understanding the impact of the ground effect on the 2D airfoil, it is of interest to extend it to the impact of the ground effect on a finite wing. The wingtip vortices are found to be displaced outboard and be suppressed by interacting with the ground surface, which is caused by the so-called span-dominated ground effect. The most significant impact of the SDGE is a large reduction in the lift-induced drag and, consequently, a great improvement in the lift-to-drag ratio. This section will demonstrate some previous works on the impact of the SDGE on the aerodynamics and tip vortices generated by the rectangular, backward, and forward swept wings.

2.3.1 Rectangular Wing

Harvey and Perry (1971) pioneered the experimental research on the flow field induced by a descending trailing vortex generated behind a rectangular half wing with moving ground condition at $Re = 3.47 \times 10^5$, which simulated the evolution of wingtip vortices during takeoff. As the trailing vortex moved downstream and descended close to the ground, the main vortex induced a spanwise crossflow, resulting in a suction peak underneath the vortex core. When the spanwise boundary layer passed under the vortex, an adverse pressure gradient was formed to accommodate the suction. As the vortex moved further close to the ground, the strong pressure gradient separated and rolled up the spanwise boundary layer into a bubble which had opposite vorticity with respect to the main vortex (Fig. 2-6). The bubble grew rapidly downstream and eventually detached from the ground surface, forming a secondary vortex (SV). The formation of the SV was found to not only spiral around and merge with the tip vortex but also cause it to rebound from the ground. However, no quantitative data about the impact of the secondary vortex was reported.

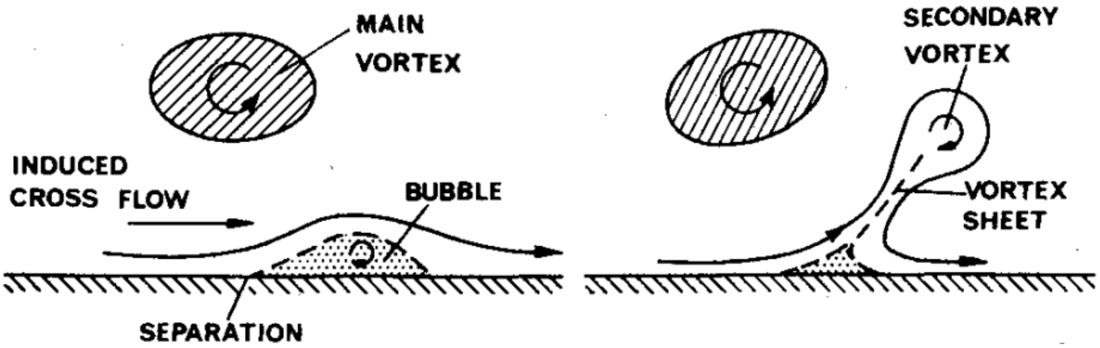

Figure 2-6 The development of secondary vortex and vortex rebound. (reproduced from (Harvey and Perry 1971))

The existence of SV and rebound movement of the main vortex were proved by Corjon and Poinsot (1997)'s work using direct numerical simulation of a pair of descending vortices at a circulation-based Reynolds number $Re_\Gamma = \Gamma/\nu = 7.5 \times 10^3$ with moving ground condition. Regardless of the crosswind, the trailing vortex was found to separate the spanwise boundary layer when it was sufficiently close to the ground, and the SV pushed the main vortex upward. However, the height of the rebounded vortex depended on the crosswind velocity.

Chun et al. (1996) further investigated the evolution of trailing vortex in ground effect both numerically and experimentally. Due to the limited space between the wing and the ground surface, the trailing vortices were unable to develop fully, resulting in a weaker vortex than its OGE counterpart. Consequently, the lift-induced drag was reduced. Similarly, Han and Cho (2005) simulated the unsteady evolution of the wingtip vortex generated behind a wing with elliptic loading in ground effect using the discrete vortex method. The ground was simulated using the image method. They reported that when the wingtip vortex approached the ground from h/c = 0.5 to 0.1, the wingtip vortex moved outward in the spanwise direction, accompanied by a significant reduction in the strength and size of the tip vortex. It was also found that with an increase in the wing loading, the tip vortex moved more laterally and downward compared to the OGE case.

In 2010, Lee et al. (2010) performed numerical analysis to study the change of aerodynamic performance as a function of h/c in moving ground effect using a modified Glenn Martin 21 rectangular wing with AR = 1 at $Re = 0.46 \times 10^6$ for a range of α from 0° to 10°. In general, C_L increased gradually with reducing h/c from 0.5 to 0.05. The lift augmentation was enhanced with higher α. At $\alpha = 10°$, C_L increased from 0.72 to 0.88. Owing to the flat bottom surface, no unfavourable suction force was noticed at low α. As for the influence on the drag coefficient C_D, Lee et al. (2010) pointed out that since the total wetted area of the wing surface was nearly constant with a change in height, the total drag can be decomposed into pressure drag and lift-induced drag. For low $\alpha \leq 4°$, C_D began to drop moderately when the wing was below $h/c = 0.3$, whereas at high α, C_D remained almost unaffected. The reduction in drag was believed to be attributed to the weakened lift-induced drag seeing that the increased ram pressure, except around the leading edge, did not contribute to the total pressure drag because of the wing shape. At high α, the pressure drag shot up, cancelling the reduction from the lift-induced drag. In ground effect, the lift-to-drag ratio L/D was found to increase dramatically from 5 to 7 in close ground proximity at $\alpha = 2°$, while the improvement was smaller at higher α.

Qu et al. (2016) showed numerically similar results using a NACA 4412 rectangular wing with AR = 9.49 at $Re = 4.6 \times 10^5$ and $\alpha = 4°$, 6°, 8°, and 10°. With moving ground condition, C_L increased very slowly above $h/c = 1$ for all α and climbed significantly when the ground came into effect ($h/c < 1$). As the ground distance decreased, C_D decreased continuously, and the drop became steeper below $h/c = 2$. Consequently, the lift-to-drag ratio was augmented significantly between $h/c = 0.1$ and 2. At $\alpha = 6°$, the wing was found to benefit the most from the ground effect, with C_L/C_D increased from 20 to 36. Besides that, Qu et al. (2016) also investigated the near-field characteristics of the wingtip vortex in and outside ground effect. Outside ground effect, the two counterrotating tip vortices induced each other, causing a downward and inboard movement toward the wing root. While in ground effect at the fixed downstream location, the tip vortices were reported to move more laterally toward the wingtip with the reduced ground clearance, accompanied by an upward rebound movement caused by the secondary vortex. In general, the smaller the ground clearance, the greater the rebound, since the wingtip vortex-induced secondary vortex becomes stronger as it approaches the ground. Qu et al. (2016) divided the growth of the wingtip vortex in the near-field into three phases, as shown in Fig. 2-7.

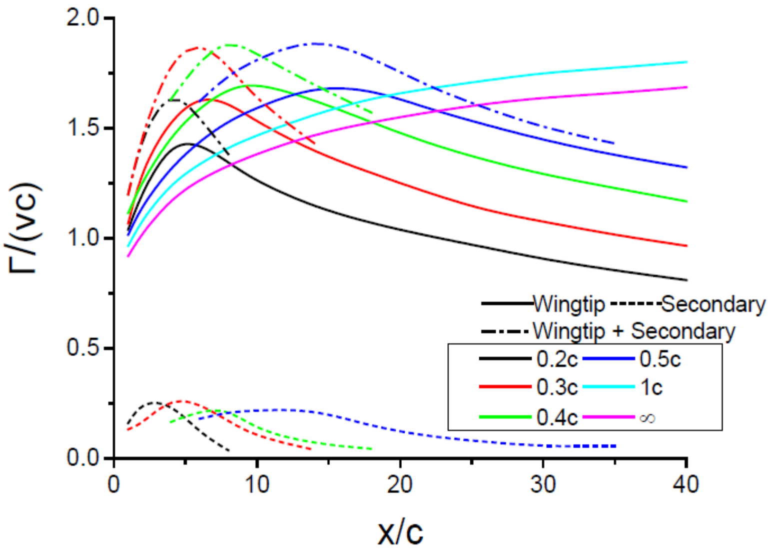

Figure 2-7 Strengths of the wingtip vortex and secondary vortex along the flow direction at α = 6°. (Qu et al. 2016)

As the shear layer continuously feeds vorticity to the tip vortex, the strength of the tip vortex increases monotonically in the first phase. Following that, the formation of the secondary vortex suppressed the main vortex growth and consumed vorticity, slowing down the strengthening and leading to the second phase. In the aftermath of the tip vortex fully developing, the negation from the secondary vortex and the natural dissipation rapidly reduced the main vortex strength. The evolution of the wingtip vortex strength in the downstream direction was summarized into a formula:

$$\Gamma_{\mathrm{x}} = \Gamma_{\mathrm{o}} + \Gamma_{\text{shear layer}} - \Gamma_{\text{secondary vortex}} - \Gamma_{\text{dissipation}}$$

where Γ_x is the tip vortex strength at location x, Γ_o is the initial vortex strength, $\Gamma_{\text{shear layer}}$ is the circulation fed into the tip vortex from the shear layer, $\Gamma_{\text{secondary vortex}}$ is the circulation of the secondary vortex, and $\Gamma_{\text{dissipation}}$ is the dissipation of the vortices due to viscous effect. The negation from the secondary occurred earlier with the reduced height. Meanwhile, the vortex size shrunk spatially.

Bleischwitz et al. (2018) reported the variation of the aerodynamic characteristics of a rectangular flat-plate wing with AR = 2 at Re = 5.6×10^4 in moving ground effect. The moving ground was achieved by a moving-belt system. The wingtip vortices, as many believe, grow both spatially and in strength as the α increased, while the strong induction between the two pull them toward the wing root. When the wing approached the ground from h/c = 2 to 0.1 at $\alpha = 15°$, the tip vortex moved outboard toward the wingtip for 30% chord length, similar to Qu et al. (2016)'s simulation. However, only a very minor rebound movement $\Delta h/c = 0.06$ was found in extreme ground proximity with a moderate drop in circulation from $\Gamma/cU = 0.4$ to 0.35, which can be blamed on the low Re tested. The load-cell data (Bleischwitz 2016) also showed a significant increase in C_L from 0.83 to 1.2, but C_D also rose from 0.28 to 0.39 resulting in a slightly improved aerodynamic efficiency.

More recently, Lu et al. (2019) conducted experimental work to study the stationary ground effect on the near-field development of wingtip vortex through *vw*-crossflow measured with a miniature seven-hole pressure probe in the J.A. Bombardier wind tunnel at McGill University at Re = 2.71×10^5. The stationary ground was simulated by an elevated flat plate with a thin laminar boundary layer of a thickness of 4 mm or equivalently a h/c = 1.6%. Lu et al. (2019) reported a large outboard movement and a reduction of the tip vortex strength, leading to a greatly reduced lift-induced drag for h/c < 20%. There was the appearance of a multiple vortex system (consisting of a tip vortex, co-rotating ground vortex, and counter-rotating secondary vortex) in close stationary ground proximity. The formation of the ground vortex beneath the airfoil's leading-edge region is attributed to the ground effect-produced ram pressure, which pushes the streamwise boundary-layer flow (developed on the stationary ground surface) backwards and towards its leading edge, rolling up into the observed recirculation region. The ground vortex first appeared along the wing's tip region (for $x/c \leq 1$) and continued downstream into the near field (for $1 < x/c \leq 3$), which added vorticity to the tip vortex. In close ground proximity (h/c < 10%), the rotation of the tip vortex also induced a spanwise flow, leading to the formation of the secondary vortex, which negated the vorticity of the tip vortex. The stationary ground effect produced higher C_L and C_D than its OGE counterparts. C_D increase was primarily due to the rise in the pressure drag from the ram pressure accumulated on the wing's lower surface and the flow separation from the wing's upper surface. However, at the same C_L, C_D was found to decrease as the ground clearance was reduced, which can be attributed to the greatly reduced lift-induced drag.

2.3.2 Backward Swept Wing

Coe and Thomas (1979) measured the aerodynamics performance of a low-AR highly swept arrow-wing in ground proximity at $Re_c = 2.0 \times 10^6$ for $h/b = 0.1$ to 1 and α from -2° to 12°. Overall, the SDGE enhanced C_L in ground proximity regardless of the flap angle, whereas C_D was found to only decrease for low α. In addition, C_L increment increased with the reduced ground clearance.

Paulson and Kjelgaard (1982) tested both experimentally and theoretically the effect of aspect ratio and sweep angle on the aerodynamic performance of a NACA 0018 backward swept wing at $Re = 1 \times 10^6$ and $\alpha = 2.78°$ and 0.78° in ground effect. Generally, at $\alpha = 2.78°$, C_L increased, and C_D decreased with reducing ground clearance due to the CDGE and SDGE regardless of sweep angle and aspect ratio. At fixed h/b, the decreased aspect ratio or increased sweep angle caused a gentler lift curve slope $C_{L\alpha}$, consequently reducing C_L, which can be blamed on the enhanced downwash effect from the wingtip vortex. Interestingly, at $\alpha = 0.78°$, C_L decreased remarkably at very low ground clearance, which was attributed to the convergent-divergent passage-induced accelerated flow underneath the wing, causing attenuation of the pressure on the bottom side.

Deng and Agarwal (2022) numerically studied the flow field around a DLR-F6 wing-body configuration in ground effect. The model was made of a fuselage and a compound backward swept wing with $AR = 9.4356$ and $\Lambda_{LE} = 27.1°$ and was tested at three different $\alpha = 0°$, 0.49°, and 1.23° with stationary ground boundary conditions. With the reducing ground clearance (from $h/c = \infty$ to 0.25) at $Re_c = 7 \times 10^5$, the results showed a linear increase in C_L and a constant drop in C_D at $\alpha = 0°$ and 0.49°. At higher $\alpha = 1.23°$, C_L increase plateaued for $h/c < 0.5$ while C_D acted oppositely, showing a minor drop between $h/c = 1$ and 0.5 and a significantly steeper decrease below $h/c = 0.5$. The difference was believed to result from the deformation of the laminar separation bubble in ground proximity at $\alpha = 1.23°$. According to the vorticity contour at all α, the wingtip vortex was found to move outboard toward the tip in ground proximity. Therefore the downwash effect on the effective angle attack was suppressed, resulting in a lower lift-induced drag, which was the main attributor to the change in C_D. The effect of the fuselage on the aerodynamic performance was negligible in ground effect.

Zhang et al. (2022) performed a numerical simulation to study the interaction between the descending wake vortex and the ground behind a half A320 aircraft model consisting of a backward swept wing, a tail wing and a fuselage at $Re_c = 3 \times 10^6$ and $\alpha = 7°$. The model was tested at $h/c_t = 31.4$ and 2.617 with both moving and stationary ground boundary conditions, where c_t is the chord at the wingtip. No significant difference was found between the two boundary conditions at $h/c_t = 31.4$. At fixed $h/c_t = 2.617$, the lift coefficient C_L was found to be lower with moving ground, which was to be blamed on the less air trapped underneath the wing resulting in less pressure on the bottom surface. Behind the wing, the evolution of the two co-rotating vortices, induced by the main and tail wings, was also studied. Before $x/c_t = 91.2$, the tail vortex was pushed downward by the downwash induced by the main vortex, whereas the main vortex moved in the opposite direction. When the tail vortex descended close to the ground, the crossflow separated the spanwise boundary layer leading to a counter-rotating secondary vortex which caused the tail vortex to rebound from the ground surface. The wake vortices diffused faster in the stationary ground condition due to the strong dissipation.

2.3.3 Forward Swept Wing

Curry et al. (1990) investigated the ground effect on the forward-swept X-29A fighter aircraft with $\Lambda_{1/4c} = -33.73°$ and AR = 4. At $\alpha = 8°$, the result showed a minor ground effect on the aircraft above h/b = 0.55 and a very rapid increase in the normal force (17% greater than the outside-ground-effect case). Yang and Wei (2010) simulated the aerodynamic performance of a half WIG craft model consisting of a forward-swept wing, a fuselage body and a PAR engine at $Re_c = 6 \times 10^6$ and $\alpha = 0°$. Without the PAR engine thrust, the combination of the CDGE and SDGE showed a clear improvement in aerodynamic performance. C_L rose proportionally from 0.45 to 0.52 with respect to the decreasing ground distance from h/c = 0.6 to 0.3, accompanied by a very small drop in C_D.

Adhikari et al. (2020) investigated experimentally the ground effect on the aerodynamic characteristics of a swept flat-plate wing undergoing a heaving and pitching motion during deceleration (landing). The swept wing with $\Lambda_{LE} = 20°$ and AR = 3 was tested in a towing tank at $Re = 1.3 \times 10^4$ and $\alpha = 15°$ and the instantaneous force was measured by a six-axis force and torque sensor. The test was categorized into two phases: the steady phase and the growth phase. In the steady phase, which was before the starting of the heaving and pitching motion, the aerodynamic forces remained constant. When the wing approached the ground at h/c = 0.2, the lift force increased dramatically from 0.19 N to 0.6 N, accompanied by a sharp increase in the drag force, which was attributed to both the enhanced pressure on the bottom side due to the decreasing ground distance and the acceleration of the fluid. Both forces dropped gradually after the peak as the wing was decelerating to simulate the landing situation. The experimental results were later proved by CFD simulation with a slight difference in the initial stage.

Doig et al. (2012) conducted numerical experiments to study the aerodynamics performance of an ONERA M6 swept wing, with Λ_{LE} = 30°, Λ_{TE} = 15.8° and AR = 3.8, at high subsonic speed (M_∞ = 0.8395) and α = 3.06° in close ground proximity. Based on the density contour, as the ground clearance decreased from h/c = 1 to 0.1, the high-pressure region underneath the wing was getting obvious, accompanied by a sharp increase in the suck on the upper surface near the leading edge, which indicated a significant increase in the effective angle of attack. C_L was found to increase continuously with the reducing ground clearance from 0.275 at h/c = 1 to 0.32 at h/c = 0.1, and the lift augmentation was stronger in the closer ground distance. However, the wing loading shifted inboard significantly between h/c = 0.25 and 0.1 because the flow near the tip region started to separate due to the ground-induced strong adverse pressure while the boundary layer close to the root remained attached. Consequently, C_D rose very gradually above h/c = 0.25 from 0.017 to 0.021, followed by a sharp increase to 0.037 at h/c = 0.1. At *x*/c = 3, the wingtip vortex was observed to move further outboard, passing the wing tip with reduced ground distance due to the enhanced spanwise flow. Surprisingly, the strength of the tip vortex decreased in close ground proximity while the opposite was expected because of a higher lift generated. It was attributed to the strong low-pressure region on the lower surface near the wingtip due to the formation of the shockwave, which reduced the pressure difference between the top and bottom surfaces.

2.4 Objectives

In spite of the seemingly great number of published studies on the wake flow generated behind the wings, very few reports have been published regarding the near-field tip vortex flow, lift-induced drag, and aerodynamics of the BSWs and FSWs in close ground proximity. This motivated the investigation of the stationary ground effect on the wingtip vortex and its associated lift-induced drag generated behind BSWs and FSWs, as well as their aerodynamics at various fixed ground distances. Furthermore, there has been no calculation of lift force based on the *vw*-crossflow measurements behind finite wings in ground effect. The lift prediction is of critical importance, as if the trailing vortex flow field can be captured, one can approximate the total lift of a wing without the use of a force balance. As a result, one of the key objectives of this study was to calculate the total lift coefficient C_L in ground effect by applying the modified Kutta-Joukowsky theorem as well as by integrating the spanwise circulation distribution based on the trailing vorticity flow field inferred from the *vw*-crossflow measurement. The results were compared against the direct wind-tunnel force balance measurements.

It is anticipated that the present measurements contributed to a better understanding of the tip vortex behaviour and aerodynamic characteristics of the three wing platforms at different ground distances, especially for the forward swept and backward swept wings, which could aid the design of future GEVs. The discussion will include the variation of aerodynamics performance, tip vortex parameters, associated lift-induced drag coefficient C_{Di} computation, and spanwise circulation distribution and its associated C_L computation with different ground distances.

3 Experimental Procedures

The purpose of this section is to summarize the experimental procedures used in this study. To begin with, the structure of the flow facilities and the wing models tested are discussed. Afterwards, a detailed description of the experimental setup, including the wing models and the measurement mechanism, will be provided. Finally, the procedure for data acquisition and analysis will be described. In addition, the associated experimental uncertainties will be discussed.

3.1 Flow Facility

The experimental work was carried out in the J.A. Bombardier low-speed suction-type wind tunnel in the Aerodynamics Laboratory at McGill University (Fig. 3-1). This open-loop wind tunnel is divided into three major sections: flow conditioning section (inlet), test section, and power section (outlet). The 3 m contraction section consists of 10 mm honeycomb straighteners and four 2 mm screens which control the freestream turbulence intensity to be less than 0.05% at 35 m/s. The contraction ratio of the flow conditioning section is approximately 10:1. The middle rectangular section has a dimension of 0.9 m×1.2 m×2.7 m in the vertical (y), horizontal (z), and streamwise (x) directions, respectively. Lastly, the power section is equipped with a 16-blade vibration isolated fan with a 2.5 m diameter, which was controlled by a variable-speed AC motor with an acoustic silencer. The power and test sections are connected with a 9 m-long flow conditioning section to control the flow condition as well. The wind tunnel speeds at different fan rotating speeds were pre-determined using a miniature pitot tube connected with a Honeywell DRAL 501-DN differential pressure transducer with a maximum 50 mm water head. The calibrated transducer has a resolution of 97 Pascal/Volt, and the response was found to be linear with 1% uncertainty.

All tests were conducted at freestream speed U = 13.8 m/s with a turbulence intensity of 0.3%. Depending on the wing model tested, which will be introduced in the following section, Reynolds numbers are 2.48×10^5 and 1.81×10^5 for the rectangular wing and swept wings, respectively. As discussed in Section 2.1, the wingtip vortex flow is not strongly dependent on Reynolds number. Therefore, the selection of Reynolds number was based on the freestream velocity, which was selected to best simulate the flight condition of the ground effect vehicle while concerning the constraints of the operation safety and endurance.

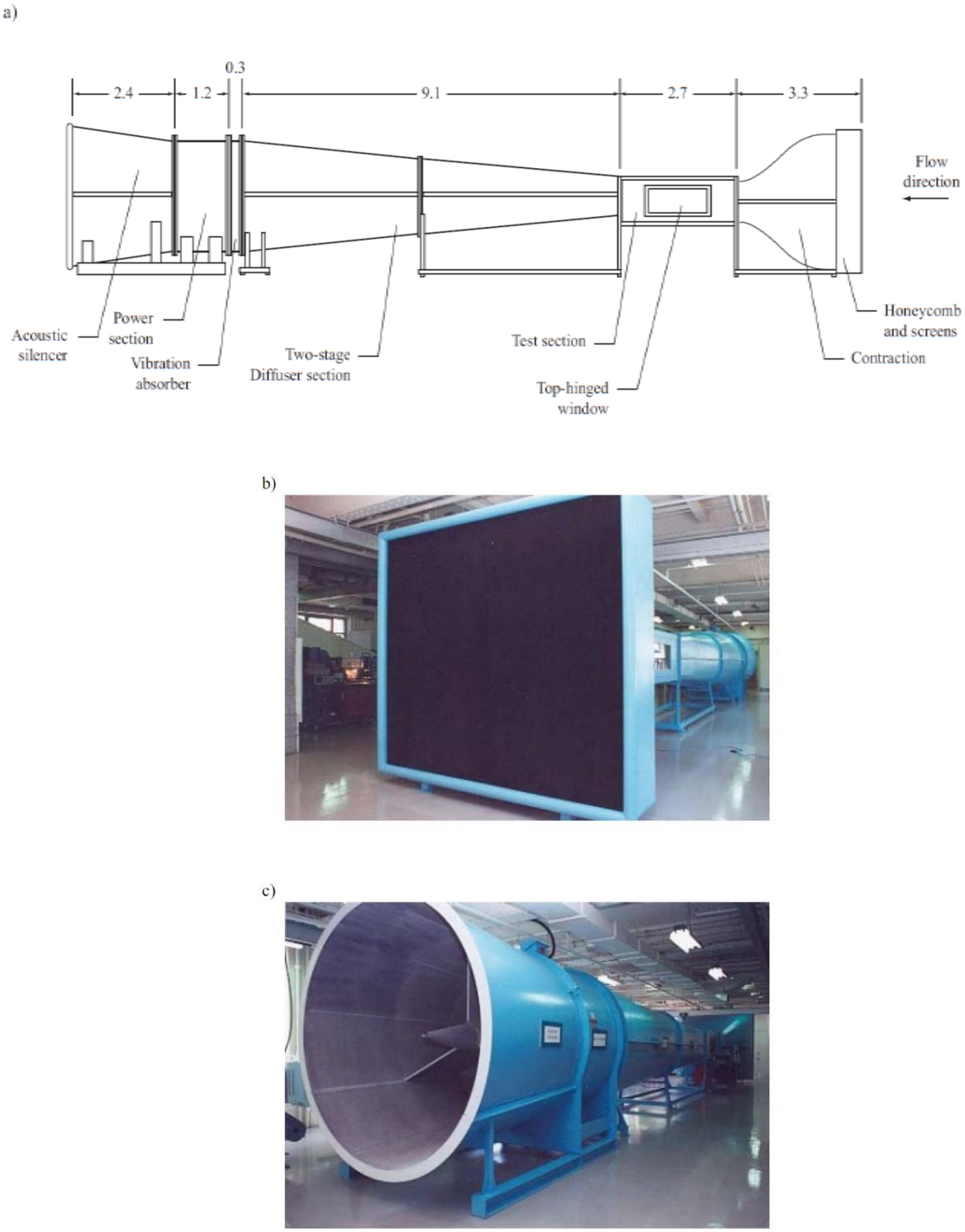

Figure 3-1 Schematic of J.A. Bombardier wind tunnel. (a) schematic diagram, (b) wind tunnel inlet and (c) outlet. (Pereira 2011)

3.2 Wing Models

Three semi-wing models were tested. The first one is an NC-machined square-tip rectangular wing with a chord of c = 28 cm and a semi-span b/2 = 50.8 cm, giving a half-wing AR = 1.81, with 1.5 mm trailing-edge thickness (Fig. 3-2 left). The maximum dimension tolerances were 250 μm. The pitching axis is located at the 1/4-chord location. The NACA 0012 rectangular wing was selected due to its great simplicity and rich research experience from our and other groups.

The second wing model is also an NC-machined, untwisted sweptback and tapered wing with an aspect ratio of AR = 3.654, a taper ratio of $\lambda = 0.375$, and a semi-span b/2 = 50.8 cm, giving a wing area of S = 713 cm^2 (Fig. 3-2 middle). The root chord c_r is 20.3 cm, and the tip chord c_t is 7.6 cm. The 1/4-chord swept angle $\Lambda_{1/4c}$ is 24°, the leading-edge swept angle Λ_{LE} is 26.9°, and the trailing-edge swept angle Λ_{TE} is 14.5°. The cross-section of the wing has a NACA 0015 airfoil profile throughout. The pitching axis is set at the 1/4-chord location as well. The last wing model is an NC-machined untwisted forward swept and tapered wing with identical dimensions as the backward swept wing (Fig. 3-2 right). Except that, the 1/4-chord swept angle $\Lambda_{1/4c}$ is -24°, the leading-edge swept angle Λ_{LE} is -21° and the trailing-edge swept angle Λ_{TE} is -32.3°. The swept wings were selected because of their significant lack of research information, especially in ground effect. To keep consistency, the origin of the coordinates for all three wing models was set at the leading edge of the wing root, with *x*, *y*, and *z* aligned with the streamwise, vertical, and horizontal directions. Also, a majority of the variables were normalized by using the root chord c_r. For the rectangular wing semi-wing, since it has a constant cross-section across the wing span, the root chord c_r of the rectangular wing is the chord c = 28 cm.

Figure 3-2 Three wing models tested. (left) rectangular wing, (middle) backward swept wing, and (right) forward swept wing.

3.3 Experimental Setups

In this research project, the experimental works can be mainly divided into 1) the aerodynamic force measurement and 2) the mean trailing vortical wake flow measurement.

3.3.1 Aerodynamic Force Measurement

For direct lift and drag measurements, the wing model was mounted vertically on an external two-component force balance located below the wind tunnel (Fig. 3-3). The wing model was mounted vertically over a 0.45 × 60 × 60 cm^3 aluminum endplate with sharp leading edges. An aerodynamic fairing was placed around the shaft to isolate it from the tunnel flow. The gap between the wing model and the endplate was kept at less than 1 mm to minimize leakage of flow through the gaps. The schematic of the force balance is shown in Fig. 3-4. The force parallel to the wing chord (T-direction) and normal to the wing chord (N-direction) was captured by two sets of flexures which support the sensor plate of the force balance. The deflection of this cantilever-type spring flexure had a maximum of 4 mm and was independently measured using two Sanborn 7DCDT-1000 linear variable differential transformers (LVDT). The resolutions of the LVDTs were 120, 93 and 0.6 Newtons/Volt in the +N, -N and +T directions, respectively. The calibration of the force balance was also carried out in situ, and a detailed description of the calibration procedures is provided in Appendix A.

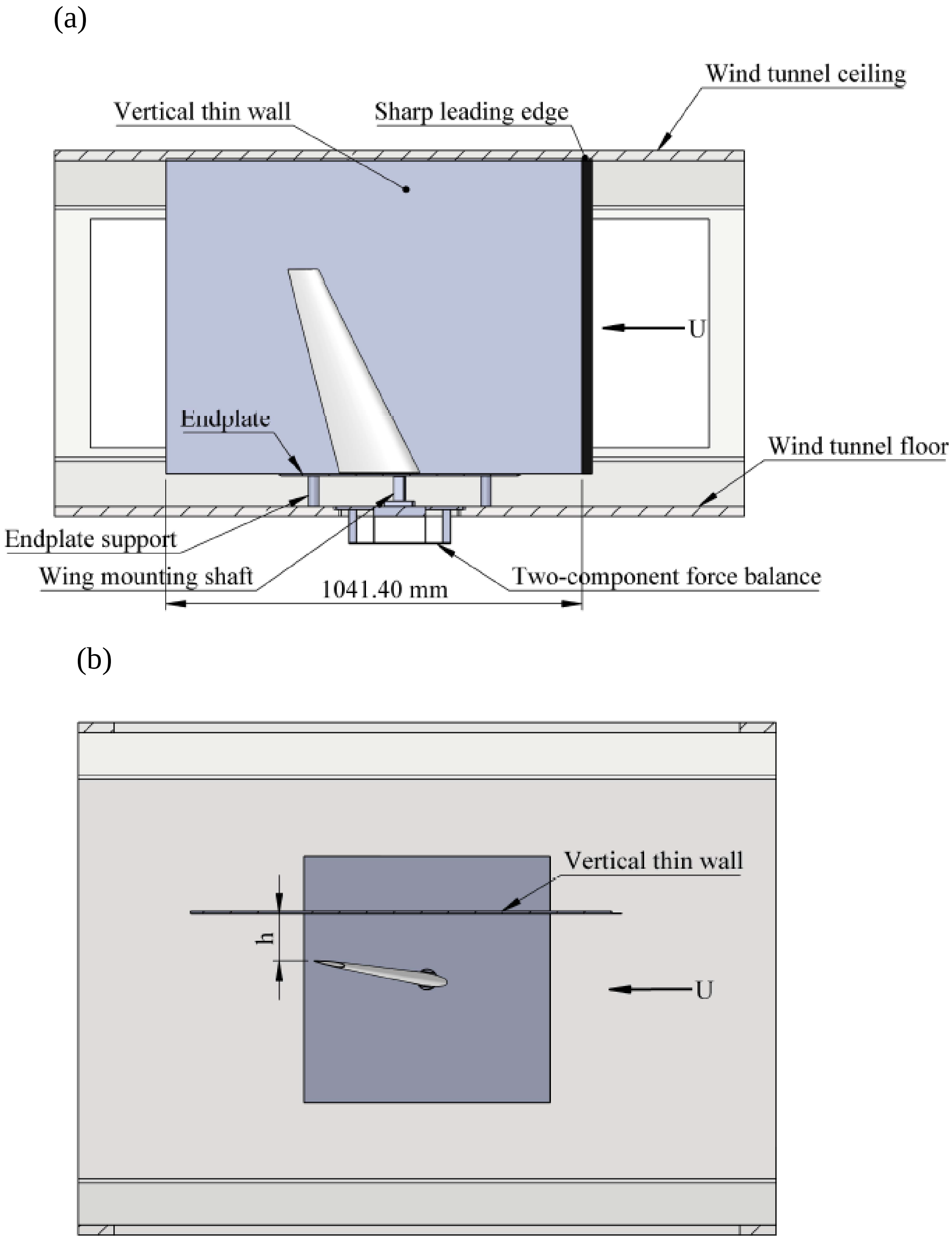

Figure 3-3 Schematic diagram of the force balance measurement setup. (a) side view and (b) top view.

Figure 3-4 Two-component force balance. (Pereira 2011)

A 106 cm × 79 cm thin flat plate equipped with a sharp leading edge was placed vertically on the endplate to simulate the stationary ground (Fig. 3-3). The ground distance was set manually by moving the flat plate in the direction normal to the freestream. The angle of attack of the wing model was adjusted by using the turntable located underneath the wind tunnel.

3.3.2 Mean Trailing Vortical Wake Flow Measurement

In the wake measurement, the semi-wing models were mounted horizontally on a support plate above the stationary ground. A thin 0.16 × 75 × 90 cm^3 iron plate with a sharp leading edge was installed between the support plate and wing model to isolate the free end effects (Fig. 3-5). The stationary ground was simulated by the use of a thin 1.4 m long and 1.2 m wide aluminum flat plate. The leading edge of the flat plate was modified to have an elliptic nose with a major-to-minor axis ratio of 5:1, and the flat plate was also equipped with a trailing edge flap. The laminar boundary layer developed on the flat plate had a thickness δ of 4 mm or a displacement thickness δ^* of 1.33 mm, which translates into a $h/c_r = 1.925\%$ or $\delta^*/c_r = 0.654\%$, where h is the ground distance, and c_r is the root chord of the swept wings. The flat plate was also elevated 15 cm above the tunnel floor to eliminate the effects of the wind tunnel boundary layer (Fig. 3-5). Note that, to be realistic, a moving ground should be adopted to perform the ground effect analyses, but the long wake scanning hour prohibited us from using a high-speed moving belt to simulate the ground. The discrepancies between the usage of a stationary ground and a moving ground in ground effect analyses were first investigated numerically by Barber et al. (2002), as reviewed in Section 2.2. The major discrepancies were that a recirculation zone/ground vortex existed in the fixed ground effect analyses, while the ground vortex was absent when the moving ground was adopted. Consequently, the fixed ground induced a slightly higher lift than the moving ground because the presence of the ground vortex further blocked the flow. However, in extreme ground proximity, a convergent passage was formed between the wing's lower surface and the ground vortex, which accelerated the flow on the bottom side and, thus, decreased the lift force. These discrepancies were confirmed later by the experimental work from Tremblay-Dionne and Lee (2021), and Lu and Lee (2020). It is also noteworthy that Shi et al. (2022) performed numerical simulations of the feasibility of fixed ground on the wind-tunnel experiments and concluded that a fixed plate could reproduce the lift and pitching moment induced by the moving ground effect accurately, but it failed in drag due to the inaccurate modelling of shear stress distribution. To avoid confusing the reader, the data at $h/c_r \leq 5\%$ presented in this study should be treated as references.

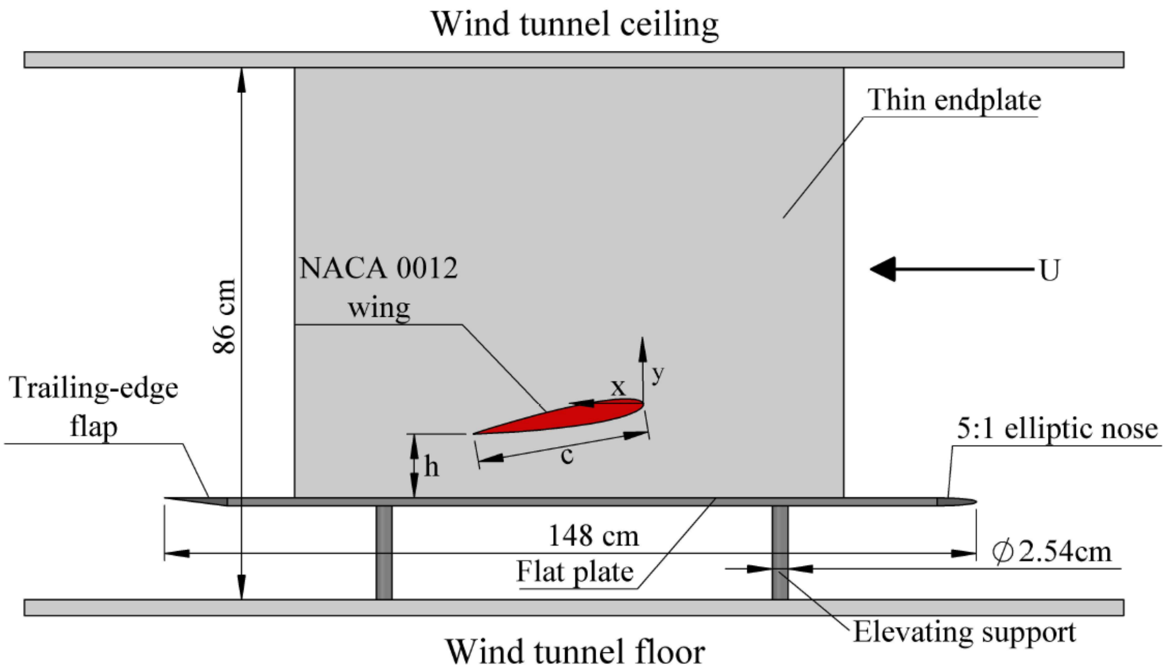

Figure 3-5 Schematic of the trailing vortical wake measurement setup.

For the rectangular wing, the ground distance h was defined as the distance between the wing's trailing edge and the ground surface. However, for the backward and forward swept wing, due to the nonzero Λ_{TE}, for any nonzero α, the distance between the wing's trailing edge and the ground varies linearly across the wing span (Fig. 3-6).

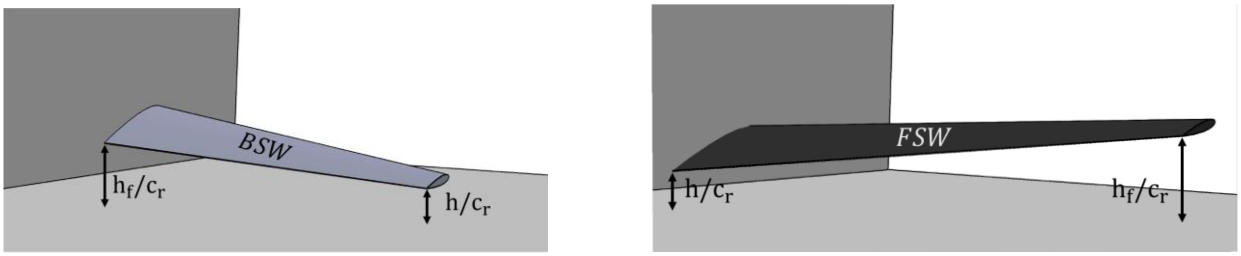

Figure 3-6 Definition of ground distance for the BSW and FSW.

For the FSW and at any positive α, the closest (h) and the farthest (h_f) ground distance are located at the root and the tip, respectively (see Fig. 3-6). The situation is the opposite for the BSW. To keep consistency and avoid any part of the wing interfering with the ground boundary layer, the normalized ground distance (h/c_r) referred to in this article used the closest distance between the wing's trailing edge and the ground surface, as indicated in Fig. 3-6 and is normalized by the root chord c_r. For the BSW, it is thus the distance between the wingtip's trailing edge and the ground, whereas, for the FSW, it is referred to the distance between the trailing edge at the root and the ground. A more direct presentation of this difference can be seen in Table 3-1, which shows the farthest ground distance (h_f/c_r) of both wings at fixed h/c_r = 10% at different α. The ground distance was adjusted by mounting the wing to a series of pre-drilled holes (corresponding to a set of h/c_r from 4% to 100%) on the support plate.

Table 3-1 Ground distance at the root and tip as a function of α

location	BSW		FSW	
	Root (h_f/c_r)	Tip (h/c_r)	Root (h/c_r)	Tip (h_f/c_r)
α				
2^o	12.2%	10%	10%	15.5%
4^o	14.5%	10%	10%	21%
6^o	16.7%	10%	10%	26.5%
8^o	19%	10%	10%	32%
10^o	21.2%	10%	10%	37.4%
12^o	23.4%	10%	10%	42.9%
14^o	25.6%	10%	10%	48.2%

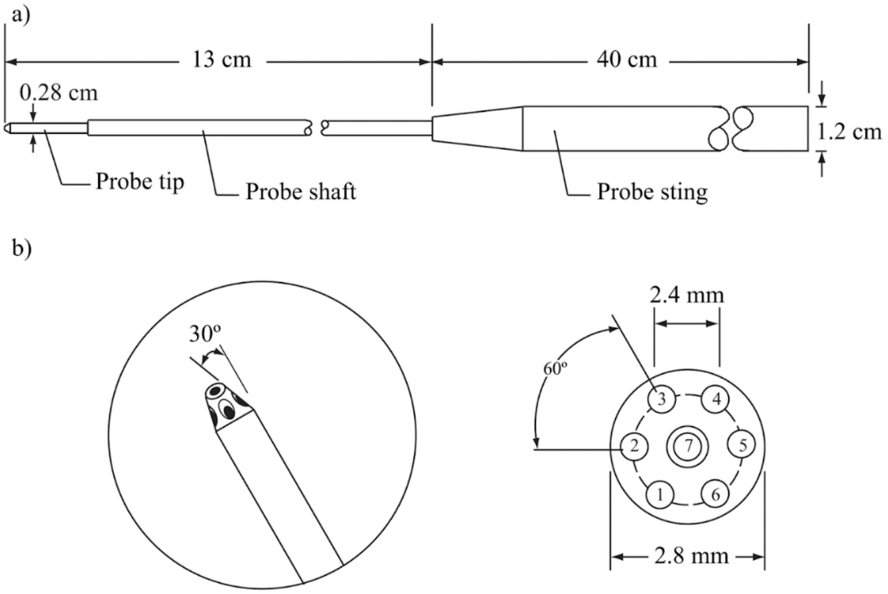

Figure 3-7 Schematic of the seven-hole pressure probe. (Pereira 2011)

Mean tip-vortex flow velocities (*u*, *v*, and *w*) were measured using a miniature 2.6-mm-diameter seven-hole pressure probe. Figure 3-7 dedicates the schematic diagram of the seven-hole pressure probe. The probe consisted of three parts: 1) probe tip, 2) probe shaft, and 3) probe sting. The probe tip, made from brass, was machined to have a cone angle of 30°. The outer diameter of the tip was 2.8 mm, and seven 0.5 mm diameter holes were drilled parallel to the sting axis, with one hole placed at the center and six arranged on a 2.4 m diameter circle. The probe shaft has a length of 13 cm and was connected to a 40 cm long probe sting with a diameter of 1.2 cm. The seven holes at the probe tip were connected with 1.6 mm diameter, 550 mm length tygon tubes which passed through the probe sting. The tygon tubes were connected to an aluminum transducer array box which contained seven Honeywell DC002NDR5 differential pressure transducers with a maximum head of 50 mm. The reference pressure was the ambient atmosphere pressure. The output of the transducer array was amplified with a gain of 5:1 through a custom-built seven-channel analogue signal differential amplifier. The average resolution of the signal was 61 Pascals/Volt, and the linearity of the response was 2%. The signal was connected to a data acquisition system which will be introduced in the later section. Prior to the installation of the wing model, the probe was first calibrated in situ and mounted on a three-degree-of-freedom custom-made traverse, as shown in Fig. 3-8. Details of the seven-hole pressure probe calibration can be referred to in the previous thesis work conducted in the same laboratory by Pereira (2011).

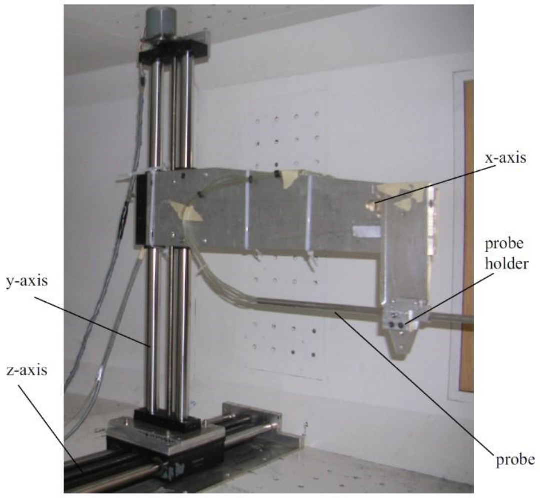

Figure 3-8 Three-degree-of-freedom traverse mechanism. (Pereira 2011)

The *y* and *z*-axis movement was achieved by the lead screw mechanism. The *z* direction was powered by a Biodine 2013MK2031 stepper motor, and the *y* direction was powered by Sanyo-Denki 103-718-0140 stepper motor. The stepper motors were controlled by a NI PCI-7344 4-axis motion controller through Labview, which was synchronized with the data acquisition. The positioning accuracy was 60 μm for the *z* axis and 20 μm for the *y* axis. The movement in the *x* direction was done manually. The blockage due to the traverse was estimated to be 8%. The present traverse system was adequate to capture the vortex flow at any Trefftz plane downstream of the wing.

3.4 Data acquisition and Reduction

For both the seven-hole pressure probe and force balance measurement, the data was obtained using a 16-channel and 16-bit NI-6259 A/D board, which was powered by a Dell Dimension E100 PC. The pressure voltage signals were sampled at 300 Hz, with a sampling time of 5s. The voltage signals of the force balance were sampled at 500 Hz, with a sampling time of 10s. A set of frequencies and sampling times was tested to ensure convergence; however, only minor discrepancies were observed. Only the mean voltage output was recorded and used for calculation because of the high linearity of the calibration curve. A detailed flowchart diagram of the data acquisition process is described in Fig. 3-9.

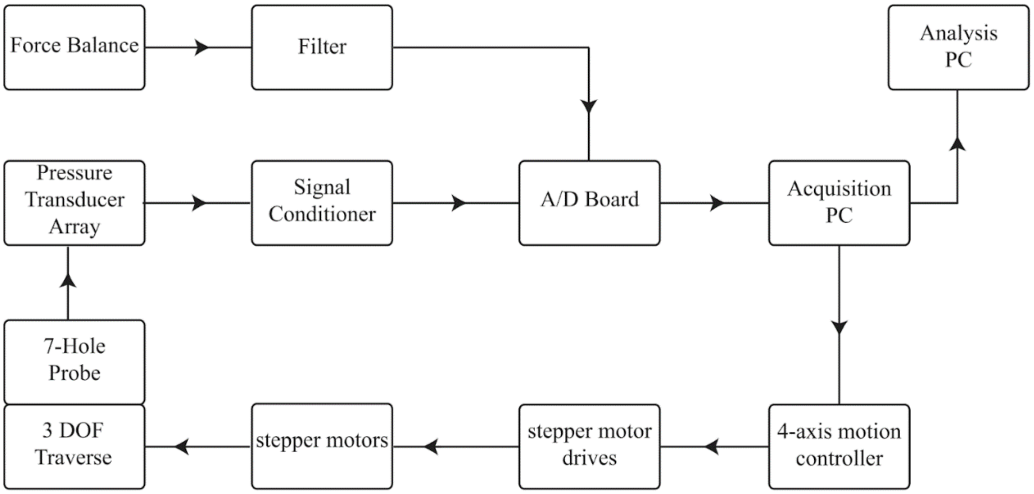

Figure 3-9 Flowchart diagram of the data acquisition process. (Pereira 2011)

Due to the traverse mechanism adopted, the static flow field measurement at the cross-stream plane downstream of the wings leading edge at $x/c_r = 2.5$ was obtained in the form of a grid of mean velocity (u, v, and w). An adaptive grid system was employed due to the large scanning hour. A fine grid with an increment of $\Delta y = \Delta z = 1.6$ mm was used in the determination of the vortex-core characteristics, and a coarser grid with an increment of $\Delta y = \Delta z = 3.2$ mm was used for the outer flow. For the remaining wake, a grid step of $\Delta y = \Delta z = 6.4$ mm was used. A sample adaptive grid system is shown in Fig. 3-10a. The location and size of the fine grid were determined by conducting preliminary tests with coarse grid size. The grid was generated using MATLAB scripts and imported to the PC for the automatic scan.

A consequence of using the adaptive grid was that all the low-resolution grids needed to be resampled to the high resolution, which was achieved by linear interpolation. The mean velocity measurements were used to calculate vortex flow properties, for example, vorticity, circulation, and tangential velocity.

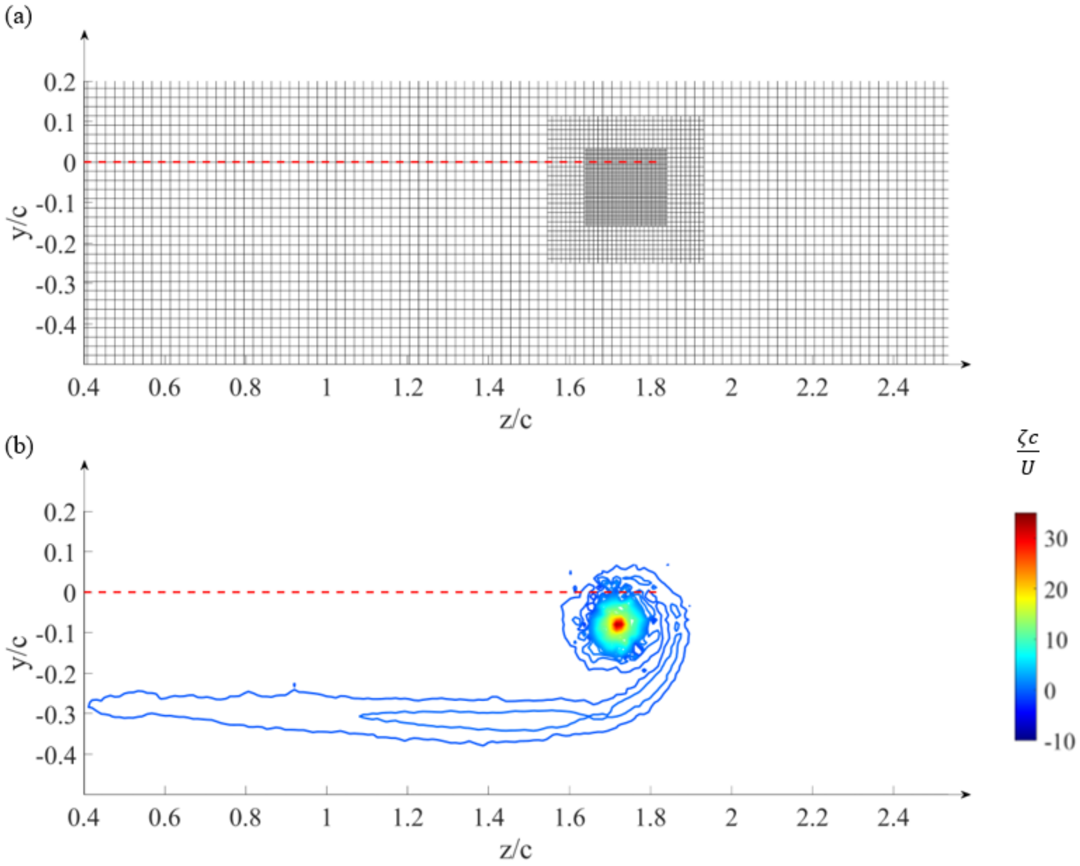

Figure 3-10 A sample of (a) adaptive grid and (b) iso-vorticity contour. The red dashed line denotes the wing's leading edge.

The vorticity was calculated based on the second-order difference scheme as the following:

$$\zeta_{i,j} = -\left(\frac{\partial v}{\partial z} - \frac{\partial w}{\partial y}\right) \approx -\left(\frac{v_{j+1,i}-v_{j-1,i}}{2\Delta z} - \frac{w_{j,i+1}-w_{j,i-1}}{2\Delta y}\right) \qquad (3.1)$$

where i = 1, 2, 3, …m and j = 1, 2, 3, …n. n and m are the number of grid points in the vertical and horizontal directions, respectively. A central difference scheme was used for interior data points only, whereas, for the measurement points at the edge, forward and backward differences were used correspondingly.

The circulation was computed via the Stokes theorem by summing the vorticity multiplied by the incremental area of the scanning grid as the following:

$$\Gamma_c = \sum\sum \zeta_{i,j} \times \Delta y \Delta z \quad r_{i,j} < r_c \qquad (3.2)$$

$$\Gamma_o = \sum\sum\zeta_{i,j} \times \Delta y \Delta z \quad r_{i,j} < r_o \tag{3.3}$$

where

$$r_{i,j} = \sqrt{\left(z_j - z_c\right)^2 + (y_i - y_c)^2} \tag{3.4}$$

$$r_o = r(\zeta = 0.01\zeta_{i,jmax}) \tag{3.5}$$

and the core radius, r_c, as defined by Hoffmann and Joubert (1963), was the radius at which the tangential velocity was maximum. The tangential velocity was calculated from the polar coordinates with the origin located at the vortex center as the following:

$$v_{\theta i,j} = \left(v_{i,j} - v_c\right)sin\theta - \left(w_{i,j} - w_c\right)cos\theta \tag{3.6}$$

where θ is the polar angle relative to the vortex core.

3.5 Experimental Uncertainty

The uncertainty of the variables reported in this thesis was mainly calculated based on the jitter program suggested by Moffat (1982). Moffat described that the uncertainty of any variable is dependent on several parameters that were inter-related. The source of error and their associated experimental uncertainty are mainly from two parts: 1) force balance measurements and 2) seven-hole pressure probe measurement.

3.5.1 Force Balance Measurement

Table 3-2 Uncertainty of experimental parameters

Quantity	Uncertainty (dimensional)	(non-dim)	Notes
Freestream velocity (13.8 m/s)	$\pm 0.05\ m/s$	0.36%	(1)
Freestream turbulence intensity (35 m/s)	$\pm 1.75\ m/s$	0.05%	(2)
Model profile (11 inches NACA 0012)	$\pm 0.06\ mm$	0.03%	(3)
Maximum Uncertainty		0.365%	(4)

The force balance measurement has two outputs in the N-direction and T-direction, respectively, and the lift amd drag coefficients were calculated as follows:

$$C_L = C_N cos\alpha + C_T sin\alpha$$

$$C_D = C_N sin\alpha - C_T cos\alpha$$

where C_N and C_T are the normalized force in N-direction and T-direction

Table 3-3 Uncertainty of force balance measurement

Quantity	**Uncertainty (dimensional)**	**(non-dim)**	**Notes**
Resolution in N-direction	$\pm 0.09\ N$	± 0.00544	(5)
Resolution in T-direction	$\pm 0.05\ N$	± 0.003	(5)
Angular position (ϵ_α)	$\pm 0.25°$		
Transducer calibration linearity (N-direction)		0.1%	
Transducer calibration linearity (T-direction)		0.7%	
A/D conversion	$\pm 1\ mV$		(6)
Transducer uncertainty in N-direction	$\pm 0.12\ N$	± 0.0072	(7)
Transducer uncertainty in T-direction	$\pm 0.006\ N$	± 0.00036	(7)
Total uncertainty in N-direction (ϵ_N)	$\pm 0.15\ N$	± 0.0091	(8)
Total uncertainty in T-direction (ϵ_T)	$\pm 0.051 N$	± 0.0031	(8)
Maximum C_L uncertainty (ΔC_L)		± 0.025	(9)
Maximum C_D uncertainty (ΔC_D)		± 0.005	(9)

Notes:

1. Calculated based on the pitot tube probe uncertainty analysis from Barlow et al. (1999).
2. Hot-wire anemometer measurement
3. 0.0025” machining accuracy
4. Using constant odds combination suggested by Moffat (1982) using free stream velocity, turbulence intensity and model profile uncertainties as variables
5. Minimum mass the transducer can sense
6. Minimum voltage reading
7. Calculated from A/D conversion uncertainty and calibration sensitivity as follow:
    - 7.1. Minimum force in N-direction $\pm 1\ mV$ (A/D conversion uncertainty)$\times$ 120 N/V (calibration sensitivity) $= \pm 0.12\ N$
    - 7.2. Minimum force in T-direction $\pm 1\ mV$ (A/D conversion uncertainty)$\times$ 0.6 N/V (calibration sensitivity) $= \pm 0.006\ N$

   7.3. Corresponding normalized force uncertainty in N-direction = ± 0.0072

   7.4. Corresponding normalized force uncertainty in T-direction = ± 0.00036

8. Constant odds combination using transducer and resolution uncertainties as variables
9. Using constant odds combination error procedure

   9.1. $\Delta C_L = \sqrt{\left(\frac{\partial C_L}{\partial C_N}\delta C_N\right)^2 + \left(\frac{\partial C_L}{\partial C_T}\delta C_T\right)^2 + \left(\frac{\partial C_L}{\partial C_\alpha}\delta\alpha\right)^2} =$

   $\sqrt{(cos\alpha\epsilon_N)^2 + (sin\alpha\epsilon_T)^2 + (C_T\cos\alpha\epsilon_\alpha - C_N sin\alpha\epsilon_\alpha)^2}$

   9.2. $\Delta C_D = \sqrt{\left(\frac{\partial C_L}{\partial C_N}\delta C_N\right)^2 + \left(\frac{\partial C_L}{\partial C_T}\delta C_T\right)^2 + \left(\frac{\partial C_L}{\partial C_\alpha}\delta\alpha\right)^2} =$

   $\sqrt{(cos\alpha\epsilon_N)^2 + (sin\alpha\epsilon_T)^2 + (C_N\cos\alpha\epsilon_\alpha + C_T sin\alpha\epsilon_\alpha)^2}$

3.5.2 Seven-hole Pressure Probe Measurement

The seven-hole pressure probe measurement uncertainty mainly came from three parts: 1) traverse movement, 2) pressure probe measurement, and 3) Data acquisition and calculation.

Table 3-4 Uncertainty of traverse movement

Quantity	**Uncertainty (dimensional)**	**(non-dim)**	**Notes**
Angular position		0.2%	
Traverse x position	$\pm 0.254\ mm$	0.09%	
Traverse y position	$\pm 0.254\ mm$	0.09%	(1)
Traverse z position	$\pm 0.762\ mm$	0.27%	(1)
Maximum traverse position uncertainty		0.36%	(2)
Grid resolution (y direction)	$3.175\ mm$	1.14%	
Grid resolution (z direction)	$3.175\ mm$	1.14%	
Vortex center location (y direction)	$\pm 3.241\ mm$	1.16%	(3)
Vortex center location (z direction)	$\pm 3.325\ mm$	1.19%	(3)
Vortex radius	$2.319\ mm$	0.83%	(4)

Table 3-5 Uncertainty of pressure probe measurement

Quantity	**Uncertainty (dimensional)**	**(non-dim)**	**Notes**
Reference pressure		0.13%	
Transducer accuracy		0.25%	(5)
Transducer sensitivity	$\pm 0.032\ mm\ H_2O$	0.18%	(6)
Transducer calibration (linearity)		0.02%	(6)

Table 3-6 Uncertainty of data acquisition and calculation

Quantity	**Uncertainty (dimensional)**	**(%)**	**Notes**
Amplifier reference voltage		0.05%	
16-bit A/D conversion	$\pm 1\ mV$	0.02%	(7)
Total pressure uncertainty	$\pm 0.06\ mm\ H_2O$	0.34%	(8)
Second-order grid interpolation		1.46%	(9)
Filtering		0.5%	(10)
Total data reduction uncertainty		1.54%	(11)
u uncertainty	$\pm 0.475\ m/s$	2.8%	(12)
v uncertainty	$\pm 0.254\ m/s$	1.5%	(12)
w uncertainty	$\pm 0.254\ m/s$	1.5%	(12)
v_θ uncertainty	$\pm 0.359\ m/s$	2.1%	(13)
Second-order finite differences	$\pm 0.762\ Hz$	3.85%	(14)
Vorticity		8.21%	(15)
Total vorticity uncertainty		9.07%	(16)
Total circulation uncertainty		11.14%	(17)

Notes:

1. Minimum step of the motor
2. Constant odd combination using x, y, z and angular position uncertainties as variables
3. Constant odd combination using traverse position uncertainty and grid resolution
4. Constant odd combination
5. Product specification

6. Calculated based on pressure transducer sensitivity(rated; $\pm 5\ mV$), calibration sensitivity (worst-case scenario; $62.2\ Pa/V$), and calibration fitted curve linearity (99.8%)
7. Standard deviation of $3.5V$ reading with a sampling frequency of 500 Hz and $10\ s$ total sampling time
8. Constant odd combination using reference pressure, transducer accuracy, transducer sensitivity, transducer calibration, amplifier reference voltage, and A/D conversion uncertainties
9. Calculated from the difference between the adjacent data point
10. The average difference using a 25-pt Gaussian smoothing field
11. Constant odd combination using interpolation and filtering uncertainties as variables
12. Using jitter program suggested by Moffat (1982) and set pressure and data reduction uncertainty as variables
13. Constant odd combination using v and w uncertainties as variables
14. Average error compared to cubic spline curve fitting
15. Jitter program using v, w, y, z uncertainties as variables
16. Constant odd combination using second-order finite difference and vorticity uncertainties as variables
17. Jitter program using vortex center, core radius and vorticity uncertainties as variables.

4 Results and Discussion

The impact of normalized ground distance h/c_r on C_L and C_D of the three wing models is described first in Section 4.1, followed by the discussion of the tip vortex and the lift-induced drag computation in Sections 4.2 & 4.3. In Section 4.4, the spanwise circulation distributions inferred from the *vw*-crossflow measurements were used to compute the lift force and were compared against the wind-tunnel force balance data. The aerodynamics and tip vortex flow characteristics outside the ground effect were also included to serve as a comparison.

4.1 Variation of Aerodynamic Coefficients with h/c_r

4.1.1 OGE

Figure 4-1 shows the variation of C_L and C_D with α of the RW at $Re = 2.48 \times 10^5$ and of the BSW and FSW at $Re = 1.81 \times 10^5$ outside ground effect (or equivalently at $h/c_r = 100\%$). The RW was found to stall at $\alpha_{ss} = 14^o$ with a maximum lift coefficient $C_{L,max} = 0.87$ in comparison to 11° (or 12.5°) and 0.70 (or 0.729) of the BSW (or FSW). The outboard-moving spanwise flow weakened the boundary-layer flow in the tip region, leading to a gradual tip stall of the BSW, whereas, for the FSW, the inboard-moving spanwise flow accelerated the flow on the root region, leading to a root stall.

At the same α, SWs stalled earlier due to their leading edge sweep angle Λ_{LE} causing a larger maximum local effective α. Among the SWs, the BSW showed an even earlier stall as a result of its larger $\Lambda_{LE} = 26.9°$ when compared to the FSW's $\Lambda_{LE} = -21°$. Since most of the lift of the BSW is produced close to the root rather than the tip, it also resulted in a lower $C_{L,max}$ than the FSW. The force-balance measurement further indicated that as a result of the larger maximum local effect α-induced larger form drag, the BSW produced the highest C_D among the three wing platforms for $\alpha > 4°$ (Fig. 4-1b). Outside ground effect, there was a sharp increase in C_D of the RW and FSW for $\alpha > \alpha_{ss}$. Owing to its unique tip-stall characteristics, the increase of the BSW was, however, much more gradual for $\alpha > \alpha_{ss}$.

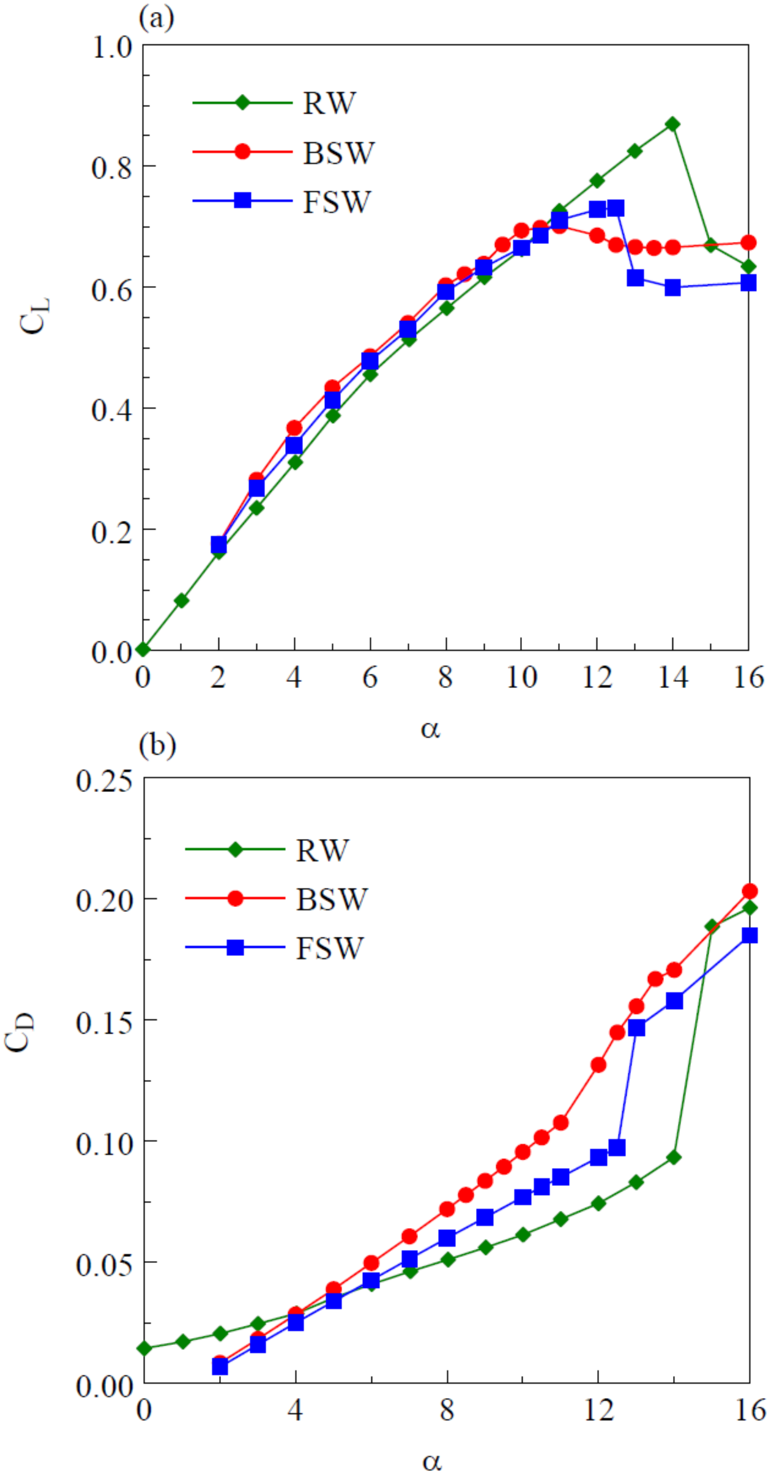

Figure 4-1 Variation of (a) C_L and (b) C_D with α outside ground effect.

4.1.2 IGE

The effect of ground proximity on the aerodynamic characteristics of the three wing platforms was summarised in Fig. 4-2. The ground effect on the aerodynamic characteristics of the RW (Figs. 4-2a-b) was previously investigated by Lu et al. (2019) in the same laboratory using the same wing model. In ground effect, all wings showed an increase in C_L with a reduction in h/c_r. Lift augmentation was primarily caused by chord-dominated ground effect-induced ram pressure increase on the lower surface of the wings. In general, the smaller the ground distance, the greater the accumulation of ram pressure and the larger the lift increase. Compared to FSW, the RW and BSW produced larger C_L. The smaller C_L of the FSW can be attributed to the fact that, at the same h/c_r, the tip of the FSW was located further away from the ground in comparison to the BSW and RW due to its unique geometry as shown in Table 3-1, resulting in a smaller ram pressure build-up.

In the present experiment, the smallest ground distance at the root of the FSW at $\alpha = 10.5°$ can only be $h/c_r = 7.5\%$, which translates into $h_f/c_r = 36.3\%$ at the wing's tip. At $h/c_r = 10\%$, a maximum of 26.7% and 33.4% C_L increase was observed for BSW (at $\alpha = 12.5^o$) and RW ($\alpha = 10°$), respectively, whereas only a maximum of 12.3% C_L increment was found for the FSW at $\alpha = 10.5°$. Figures 4-2 a,c&e also show that the ground effect has taken into effect much earlier in the RW as compared to the SWs, which also resulted from the geometry difference that, at the same ground distance, the entire RW was in ground effect, while only the tip (or the root) of the BSW (or FSW) was in ground proximity. In addition, there existed a persistent stall promotion of the RW and FSW to $\alpha_{ss} = 9°$ and 12°, respectively, for $h/c_r \leq 60\%$ due to the ground effect-induced increase in the dp/dx gradient, which caused an earlier flow separation over the upper surface of the RW and FSW. In contrast, the gradual stall of the BSW remained effective under the ground proximity, and no change to the stalling angle was observed for $h/c_r \geq 12.5\%$ (Fig. 4-2c). Nevertheless, in close ground proximity ($h/c_r < 12.5\%$), the BSW was however characterized by a delayed but steeper stall as compared to its outside ground effect (OGE) counterpart. The smaller h/c_r was, the larger α_{ss} and $C_{L,max}$ became. Special attention should also be given to the lower-than-OGE C_L value observed in close ground proximity for $\alpha < 3.5°$ of the RW and for $\alpha < 6°$ of the SWs, which can be attributed to the convergent-divergent flow passage developed underneath the wing causing an undesired suction pressure on the

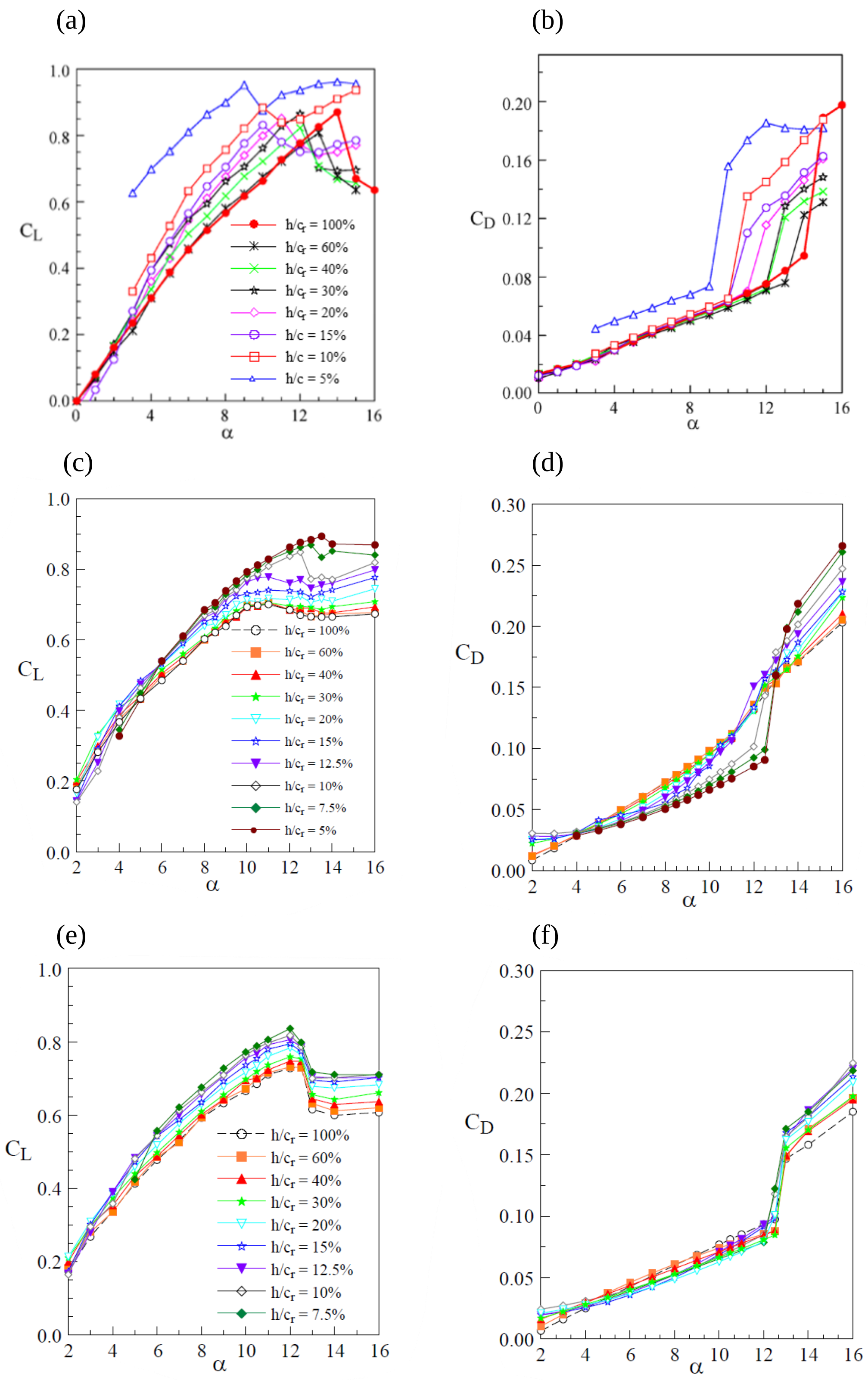

Figure 4-2 Variation of C_L and C_D with h/c_r. (a)-(b): RW (Lu et al. 2019). (c)-(d): BSW. (e)-(f): FSW.

wing's lower surface. However, for the FSW, the extent of the C_L reduction was smaller than that of the BSW and RW (Figs. 4-2 a,c&e) due to the geometry difference shown in Table 3-1. That is, at low α, the ground distance varied significantly across the span of the FSW, suggesting that the convergent-divergent passage formed only underneath the inboard region of the FSW, leading to the smaller change in lower-than-OGE C_L as compared to the RW and BSW.

Figures 4-2b,d&f further indicate that there is no significant change in C_D of the RW and FSW before stalling, except for a slight increase in C_D at $h/c_r = 5\%$ for the RW. Significant C_D shoot-up was observed in the post stall-α regime at all ground distances for the RW and FSW, and the stall promotion matched the results shown in the C_L curves. On the contrary, Figure 4-2d shows a persistent C_D decrease with the reducing ground distance for the BSW at $4° < \alpha < \alpha_{ss}$. At $\alpha = \alpha_{ss}$, as compared to its OGE counterpart, the C_D increase became steeper in close proximity to the ground. Additionally, C_D was found to increase with the reducing h/c_r for $\alpha > \alpha_{ss}$.

Lastly, Figure 4-3 shows the drag polar as a function of h/c_r of the three wing platforms. In close ground effect ($h/c_r < 12.5\%$), C_D of all wing models dropped considerably at the same lift condition for $C_L > 0.45$. Before stalling and at $h/c_r = 10\%$, a maximum 47% C_D decrease was found at $C_L = 0.62$ (or equivalently $\alpha = 8.5°$) for the BSW, whereas a maximum 28% C_D drop was obtained at $C_L = 0.68$ (or equivalently $\alpha = 10.5°$) for the FSW. For the RW, only a maximum 25% C_D reduction was observed at $C_L = 0.665$ (or equivalently $\alpha = 10°$) and at $h/c_r = 10\%$. The C_D presented in this report mainly consists of C_{Dp} (form drag coefficient) and C_{Di} (lift-induced drag coefficient). The observed C_D reduction for the RW in close ground proximity can be attributed to the C_{Di} reduction due to the enlarged AR_{eff} and weakened tip vortex caused by the span-dominated ground effect. However, for the SWs, because of their relatively small tip vortex size, C_{Di} only accounted for a tiny portion of the total drag. Thus, the reduction in C_D for the SWs in close ground effect could be credited to the reduction in the form drag. The variation of C_D and C_{Di} will be calculated and discussed in Section 4.3.

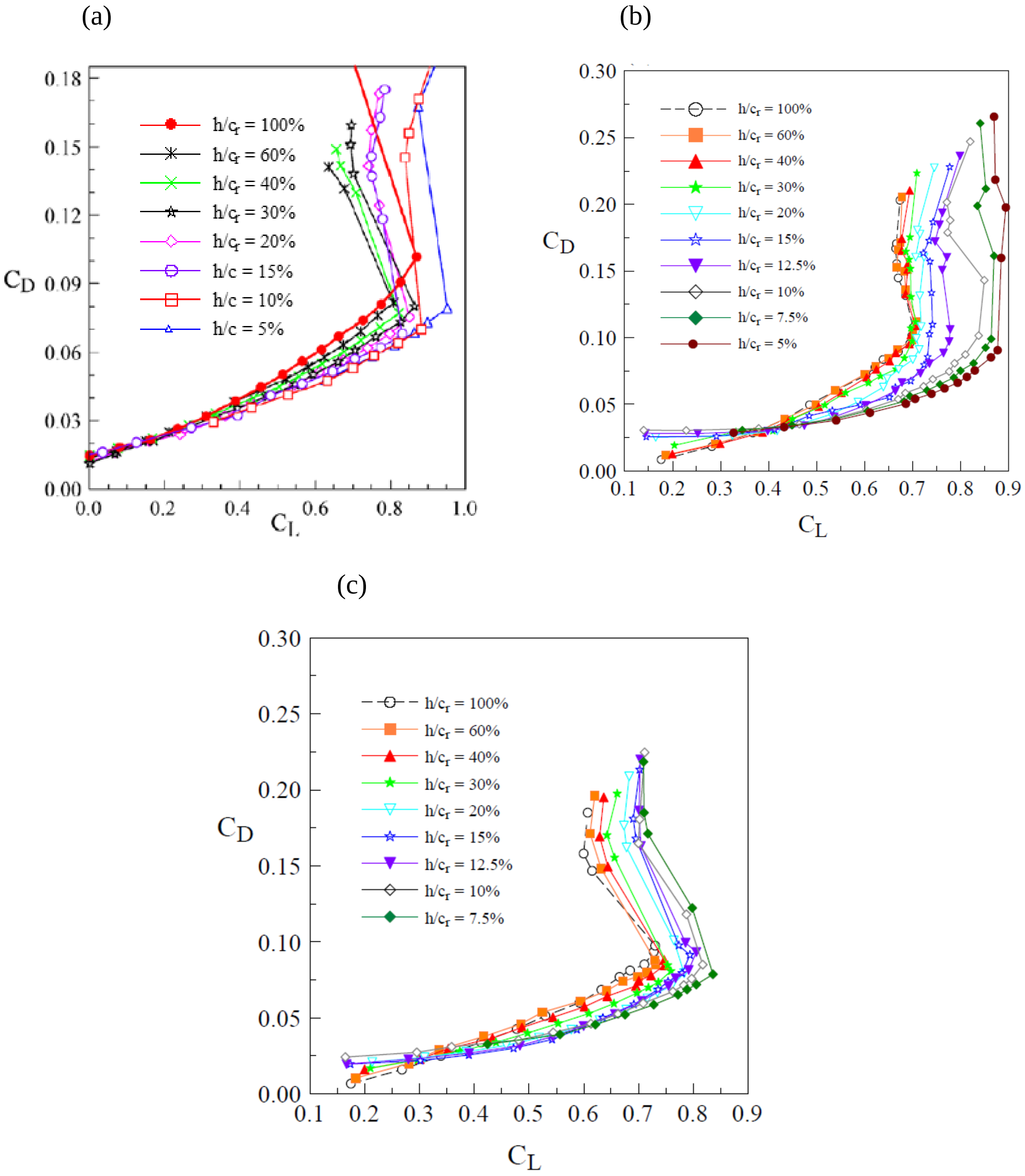

Figure 4-3 Drag polar as a function of h/c_r. (a) RW (Lu et al. 2019), (b) BSW, and (c) FSW.

4.2 Variation of Vortex Parameters with h/c_r

This section discusses the behaviour of the wake vortices generated by the three wings for h/c_r = 5% to 100% at $x/c_r = 2.5$ and fixed angle of attack ($\alpha = 10°$ for RW, 8.5° for BSW, and 10.5° for FSW). The angles of attack were selected based on the analysis of the aerodynamic characteristics in ground effect discussed in Section 4.1. Figure 4-2 demonstrates that, for the RW and FSW, the lift augmentation and drag reduction at h/c_r = 10% was the maximum at the selected angle of attack as compared to their OGE counterpart. For the BSW, the maximum lift increase was observed at $\alpha = 12.5°$. However, the tip vortex is largely diffused at $\alpha = 12.5°$ as a result of the flow separation, making it difficult to illustrate the ground effect on the tip vortex flow. Thus, to maintain an intact tip vortex and, in the meanwhile, maximize the ground effect, $\alpha = 8.5°$ was selected for the BSW. Furthermore, the fixed downstream distance $x/c_r = 2.5$ was selected to allow the tip vortex to become nearly axisymmetric (or nearly completely developed) (Lee and Choi 2015, Lee and Ko 2009, and Gerontakos and Lee 2006). To better illustrate the effect of ground proximity on the tip vortex, the wingtip vortex generated behind the wings positioned at h/c_r = 100% (or equivalently OGE) was discussed first to serve as a comparison.

4.2.1 OGE

Figure 4-4 depicts the normalized iso-vorticity ($\zeta c_r/U$) and iso-axial velocity (u/U) contours of the vortical wake behind the RW, BSW, and FSW at selected α for h/c_r = 100%. The streamwise vorticity ζ ($= \partial w/\partial y - \partial v/\partial z$) was calculated from the crossflow *vw*-measurements by using a central differencing scheme to evaluate the derivatives. For $\alpha \leq \alpha_{ss}$, both vorticity and axial flow field of the three wings were characterized by a small wake flow and a concentrated tip vortex. In addition, the SWs produced smaller and weaker tip vortices than the RW. This can be attributed to the swept and tapered wings shifting spanwise loading inboard resulting in lower lift generated in the tip region and, therefore, smaller tip vortices (Vijgen et al. 1989). Besides, the tip vortex was found to always form above the wing's trailing edge at the tip. The variation in the critical tip vortex parameters, such as total circulation Γ_o, vortex center (y_c and z_c), peak tangential velocity $v_{\theta peak}$, peak vorticity ζ_{peak}, and vortex size r_o, with α was summarized in Fig. 4-5 and will be discussed later.

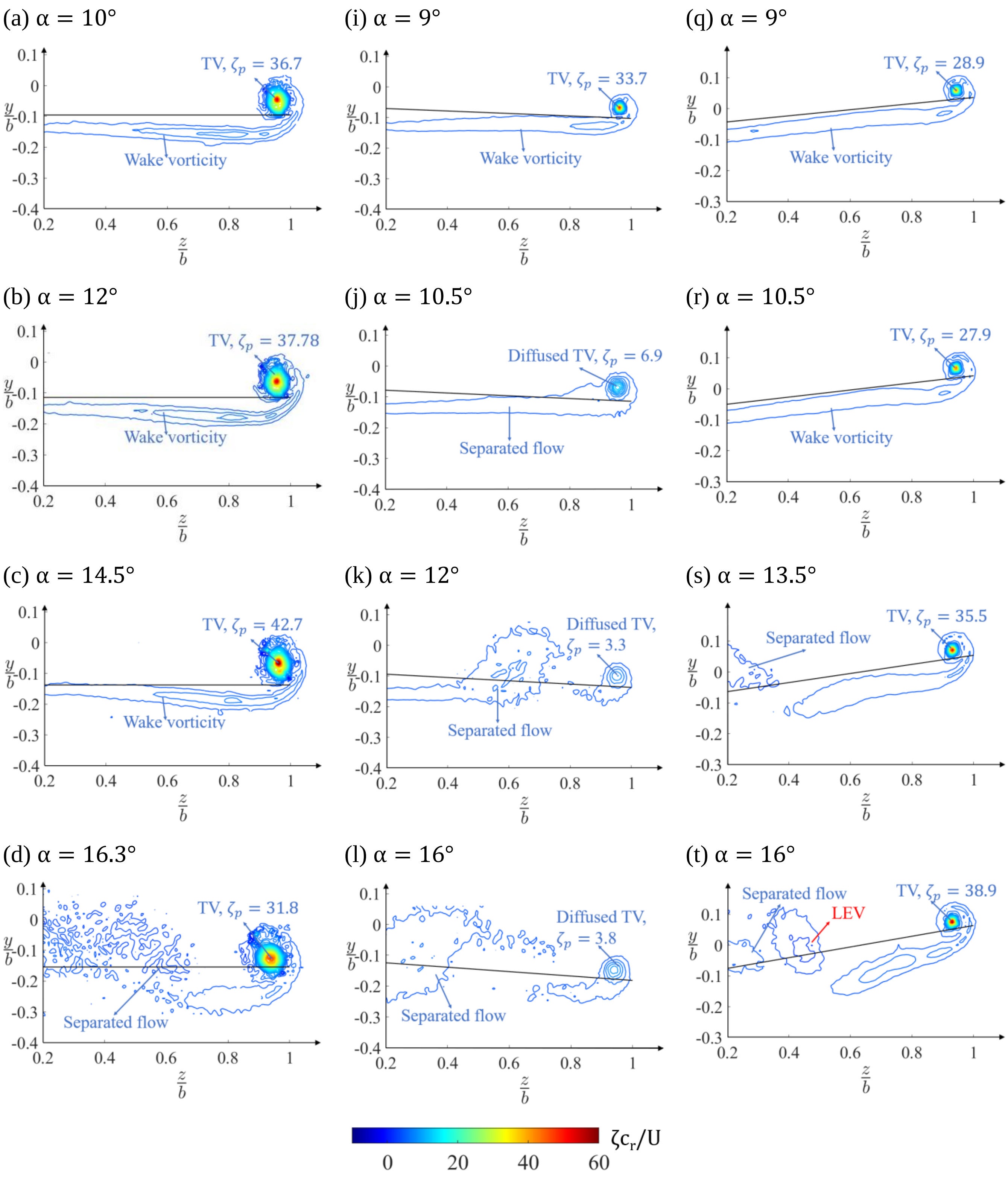

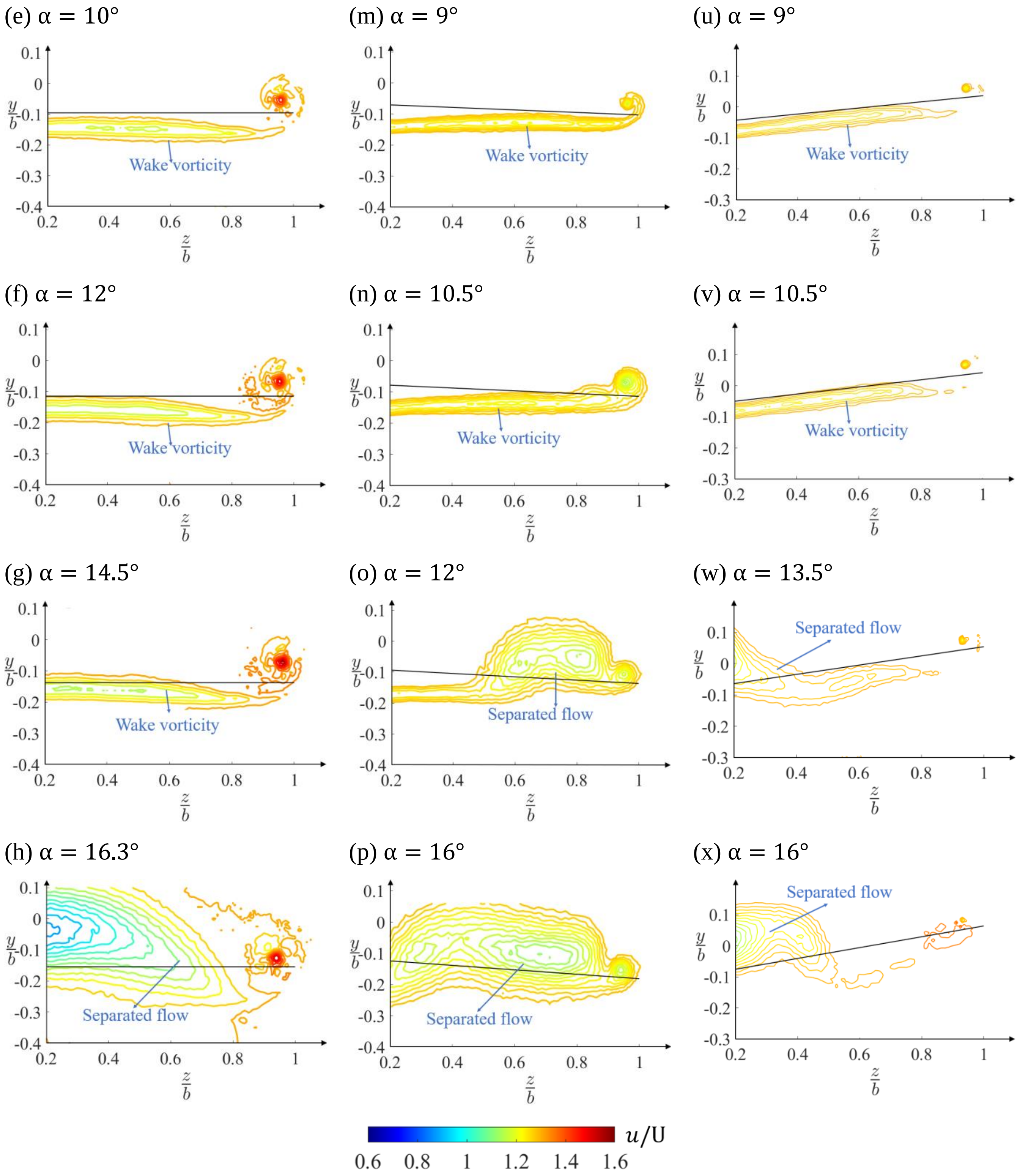

Figure 4-4 Iso-$\zeta c_r/U$ and iso-u/U contours at selected α outside ground effect. RW: (a)-(h). BSW: (i)-(p). FSW: (q)-(x). Solid line denotes wing's trailing edge location. LEV denotes leading edge vortex.

Figures 4-4 k-l&o-p show that, for $\alpha > \alpha_{ss}$, the large flow separation was initiated at the tip or outboard region of the BSW. The tip-region flow separation propagated toward the root of the BSW with increasing α. The tip stall of the BSW also led to a largely diffused tip vortex with normalized peak vorticity ζ_p (= $\zeta_{peak}c_r/U$) around 4 as compared to 33.7 of the concentrated tip vortex at $\alpha = 9°$. In contrast, the FSW's root stall-induced large flow separation in the inboard or root region can be readily identified from the $\zeta c_r/U$ and u/U iso-contours presented in Figs. 4-4s-t &w-x. Additionally, a clockwise-rotating leading-edge vortex (LEV) was observed at around the mid span of the FSW for $\alpha > \alpha_{ss}$. The flow separation grew in size and propagated outboard with a further increase in α. The root stall allowed the outboard and especially the tip region of the FSW to remain attached, resulting in a concentrated counterclockwise-rotating tip vortex with ever-increasing vortex strength and total circulation. The stalling of RW was also initiated in the root or inboard region due to the downwash-induced smaller local effective α in the tip region (Figs. 4-4d&h). However, the large flow separation propagated toward the tip region much faster than the FSW. It can be attributed to the fact that the difference between the local effective α at the tip and the root was marginal for the RW as compared to the difference induced by the spanwise flow of the FSW. The root stalling of the RW resulted in a slightly diffused tip vortex with $\zeta_p = 31.8$ at $\alpha = 16.3°$ as compared to 37.78 at $\alpha = 12°$.

Notably, the wake vorticity sheet of the FSW exhibited an upward tilting behaviour in contrast to a nearly horizontal vorticity sheet of the RW and BSW. Pate and German (2014) suggested that the intersection of the wake with the Treffz plane behind any planar wing with a nonstraight trailing edge (i.e. $\Lambda_{TE} \neq 0°$) will be tilted at any $\alpha > 0°$. Additionally, as the wingtip vortex progress downstream, the rolling up of the tip vortex and the induced downwash skew the vorticity sheet in the same direction as the tip vortex, explaining the difference in the geometry of the vortex shown in Fig. 4-4.

Figure 4-5a demonstrates the variation of the total circulation Γ_o of the tip vortex with α at $h/c_r = 100\%$ (or equivalently OGE). The circulation was computed via the Stokes Theorem by summing the vorticity multiplied by the incremental area of the measuring grid. The total circulation was computed up to the extent where the circulation reached 98% of the total magnitude. Owing to the root stall of the RW and FSW, which allows the flow in the tip or outboard region to remain largely attached or unaffected, the Γ_o of the tip vortex increased

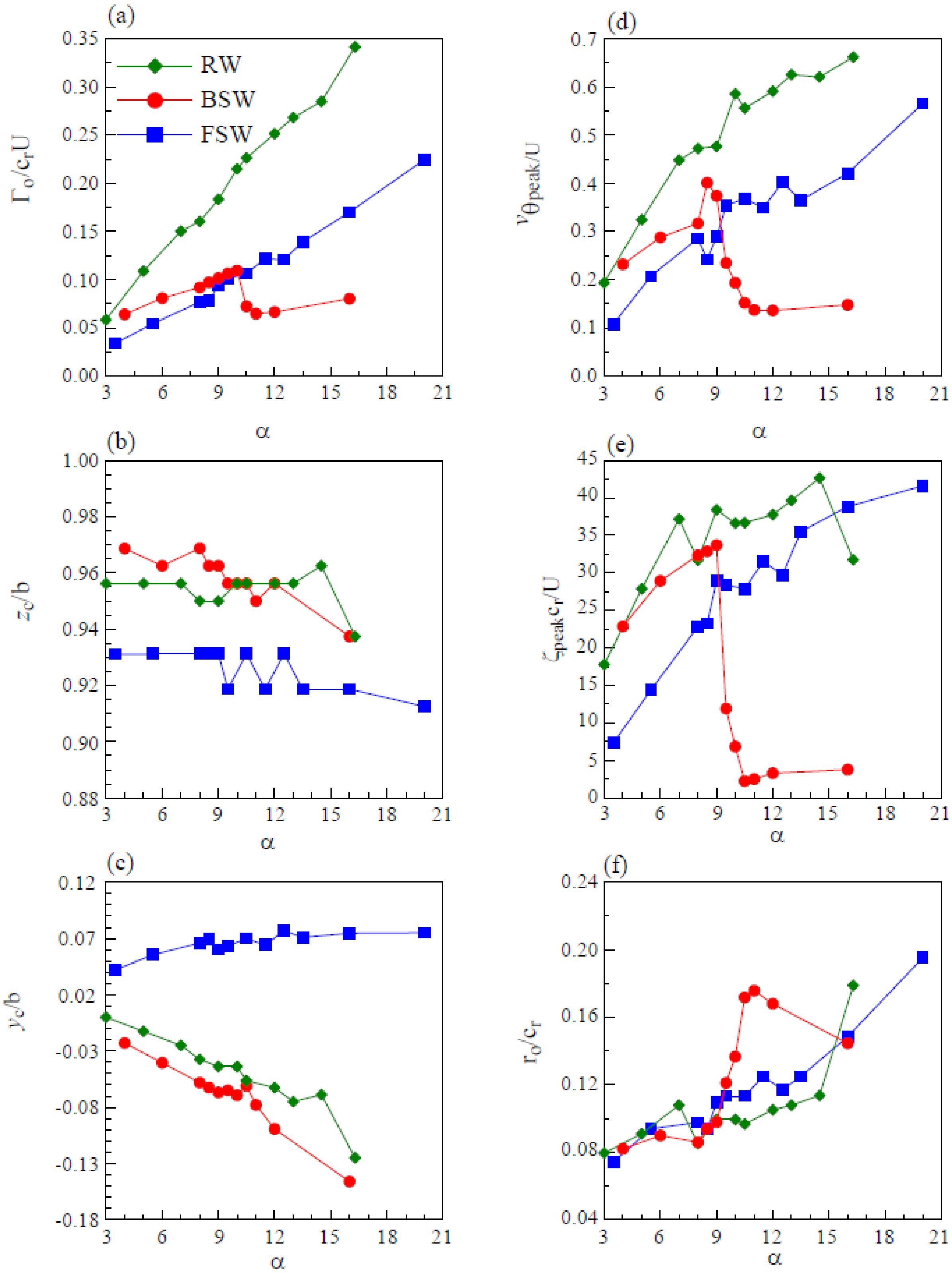

Figure 4-5 Variation of critical vortex parameters with α outside ground effect.

monotonically with increasing α. For the BSW, the Γ_o, however, increased with α for $\alpha < \alpha_{ss}$ and underwent a large decrease for $\alpha \geq \alpha_{ss}$, attributing to the tip-stall-produced diffusion of the tip vortex. In addition, the RW rendered the strongest tip vortex (largest Γ_o) among the three wings as the large and uniform wing surface concentrated the spanwise loading in the tip or outboard region. In the pre stall-α regime, the BSW also generated a stronger vortex than the FSW due to the spanwise flow-induced increased suction pressure on the wing's upper surface at the tip region, which gave rise to a more rigorous rolling up of the shear-layer flow and, thus a stronger tip vortex of the BSW than the FSW.

Outside the ground effect, the spanwise (z_c) and vertical (y_c) locations of the vortex center of all the wing models were found to be always located inboard and above the trailing edge at the tip (Figs. 4-5b-c). The vortex center was identified by the location of ζ_p. The vortex center location of the FSW was found to be insensitive to the change in α. In contrast, the tip vortex center of the BSW was found to move inboard and downward with increasing α. For the RW, the tip vortex center also moved downward with increasing α, but the spanwise location of the tip vortex center remained constant.

The seven-hole pressure measurements further indicate that the variation in $v_{\theta peak}$ and ζ_{peak} with α of all wing models (Figs. 4-5d-e) also followed the trend observed for Γ_o (Fig. 4-5a). The magnitude of $v_{\theta peak}$ and ζ_{peak} of the BSW increased with α up to 9°, followed by a drastic drop for $\alpha > 9°$. For the FSW, both $v_{\theta peak}$ and ζ_{peak} increased continuously with α. For the RW, the peak tangential velocity rose persistently with α, but the ζ_{peak} dropped considerably for $\alpha > \alpha_{ss}$ due to the diffused TV. At last, the vortex outer radius (indicative of vortex size) of the FSW increased rather linearly with increasing α (Fig. 4-5f). For the RW and BSW, the diffusion of the tip vortex beyond the static-stall angle led to a larger increase in the vortex size.

4.2.2 IGE

The impact of ground proximity on the iso-$\zeta c_r/U$ contours of the RW, BSW and FSW was described in Fig. 4-6 at $\alpha = 10°$, 8.5°, and 10.5°, respectively. For each wing under ground proximity, no significant discrepancy in the vortex flow was noticed between the IGE and OGE conditions for $h/c_r \geq 40\%$, with a slight reduction in the peak vortex strength ζ_p and a minor outboard movement of the vortex core. For $40\% > h/c_r > 10\%$, there was the persistent

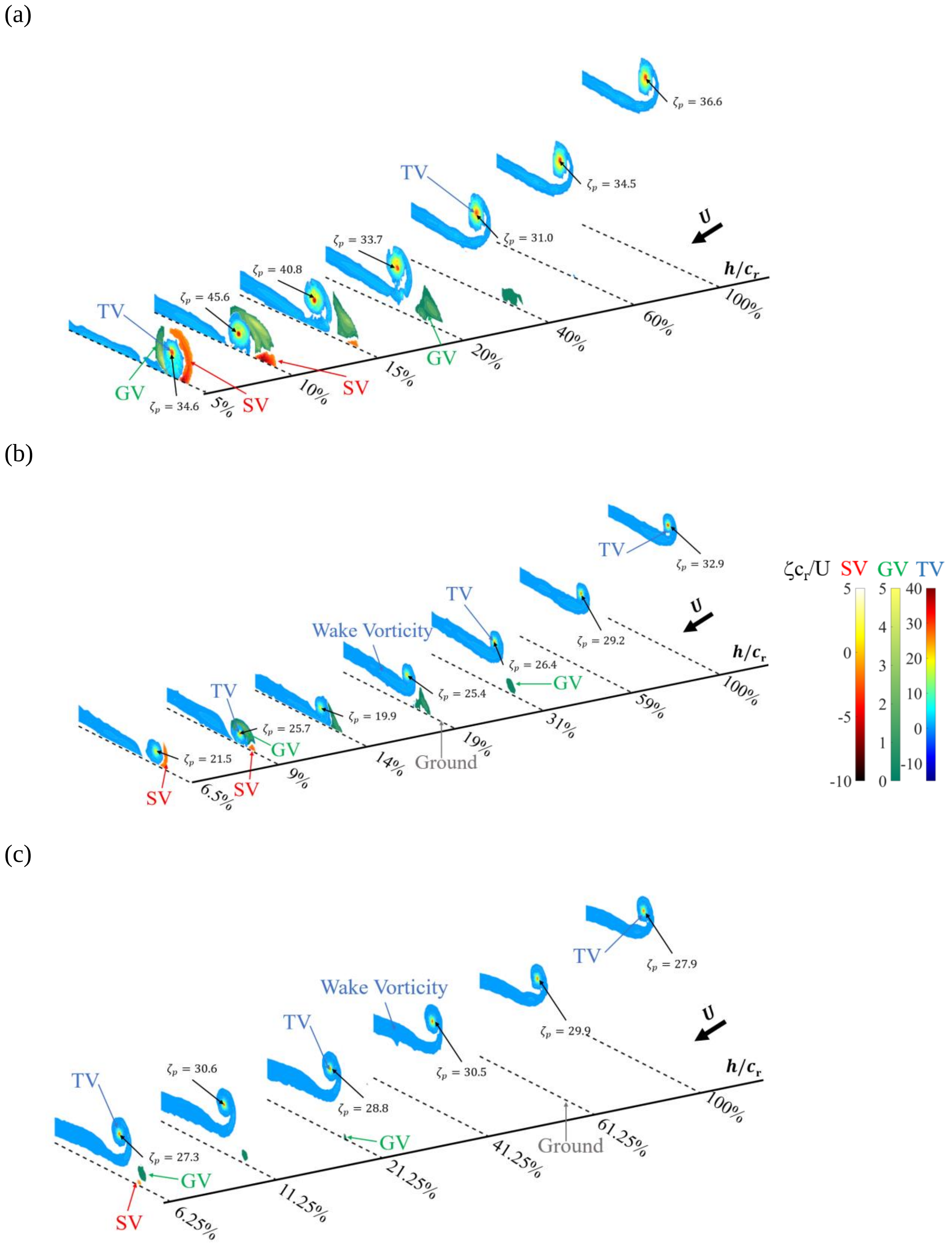

Figure 4-6 3-D presentation of the variation of iso-$\zeta c_r/U$ with h/c_r at fixed α. (a) RW at α = 10°, (b) BSW at α = 8.5°, and (c) FSW at α = 10.5°.

appearance of a co-rotating ground vortex (GV), with respect to the tip vortex (TV), behind all three wing models. Detailed discussions of the formation and behaviour of the GV were given by Lu et al. (2019) and Lu and Lee (2021) in the same laboratory, and will be briefly summarized in the following.

As reviewed in Section 2.2, the experimental results regarding NACA 0012 airfoil under stationary ground effect showed that there existed a recirculation zone or ground vortex underneath the leading edge of the airfoil in close ground proximity, which can be attributed to the ground effect-produced ram pressure pushing the streamwise boundary-layer flow backwards and towards the leading edge. For a finite wing, the recirculation zone persisted in the spanwise direction forming the so-called "spanwise ground vortex filament (SGVF)" as shown in Fig. 4-7. Progressing downstream, the SGVF escaped from the free end at the wing tip and was swept downstream developing into the observed co-rotating GV at the fixed downstream location. The co-rotating GV moves closer to the TV and merges with it as the ground is approached, leading to an increased vortex strength as compared to the OGE cases, which can be reflected by the

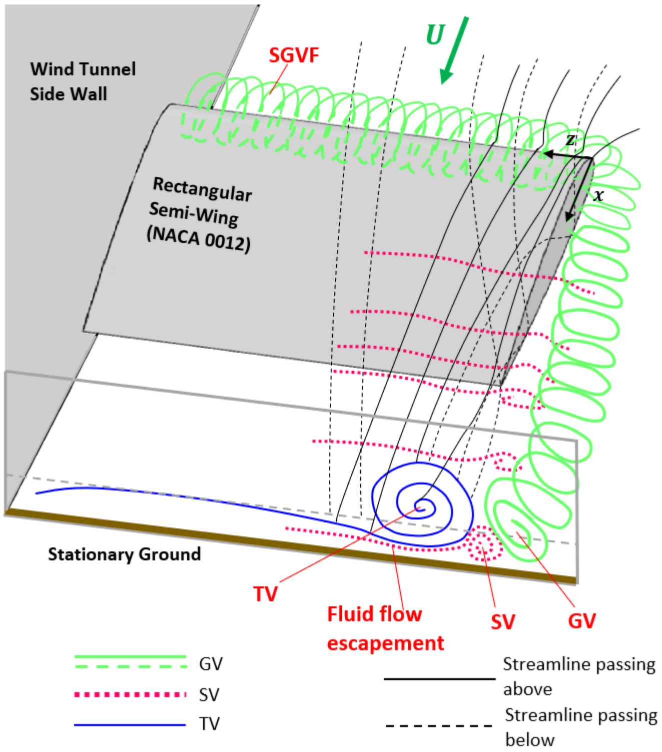

Figure 4-7 Conceptual sketch of the formation of GV and SV under stationary ground effect. (Lu and Lee 2020)

increase in the ζ_p for 40% > h/c_r > 10% as shown in Fig. 4-6. The RW and BSW possessed a stronger GV than the FSW because the FSW's tip was always located outside the close ground proximity (see Table 3-1), indicating that the recirculation zone only formed in the region close to the root or the inboard region. The ground proximity and the resulting ram pressure also caused an outboard movement of the tip vortex core, implying an increased effective AR and, consequently, reduced lift-induced drag. The impact of the ground proximity on the vortex parameters: Γ_o, z_c, y_c, $v_{\theta peak}$, and ζ_{peak} is summarized in Figs. 4-8&4-9 and will be discussed later.

Upon moving closer to the ground, the counter-rotating secondary vortex (SV), with respect to the TV, appeared at $h/c_r < 10\%$. As mentioned in Section 2.3, the formation of the SV was first observed by Harvey and Perry (1971) from a pair of descending vortices produced by aircraft during takeoff and landing. In short, the SV formed due to the roll-up of the spanwise boundary layer caused by the presence of the TV, which eventually detached from the ground, resulting in the counter-rotating SV. It should be noted that the SV associated with the FSW was indiscernible, which can be attributed to the fact that the tip of the FSW is always located outside the close ground effect. Thus, the tip vortex can not induce a significant SV. For RW and BSW, the counter-rotating SV negated the vorticity of the TV resulting in a reduced peak vortex strength for $h/c_r < 10\%$. The TV, co-rotating GV, and counter-rotating SV consisted of the unique multiple vortex system under close ground proximity, which resembled the finding from Lu et al. (2019). The appearance of the multiple vortex system in close ground proximity can also be demonstrated from the spanwise circulation distribution which will be presented in Section 4.4.

The impact of GV and SV on the total circulation of the tip vortex can be readily explained by Fig. 4-8. For the RW, the Γ_o was found to remain unchanged for $h/c_r > 60\%$ and only increased slightly for 60% > h/c_r > 40% (Fig. 4-8a), followed by a sharp increase in Γ_o for 40% > h/c_r > 10%, which can be credited to the presence of GV (Fig. 4-8b) adding vorticity to the TV. For $h/c_r \leq 10\%$, the appearance of the counter-rotating SV (Fig. 4-8b) negated the vortex strength of the TV, showing a significant reduction in the total circulation of the TV. Also shown in Fig. 4-8a is the total circulation of the entire vortex system, which resembled the trend of the Γ_o. The ground proximity, however, decreased the total circulation Γ_o of the BSW for $h/c_r > 9\%$ (Fig. 4-8c), which was attributed to the ground constraining the growth of the TV. Since the TV

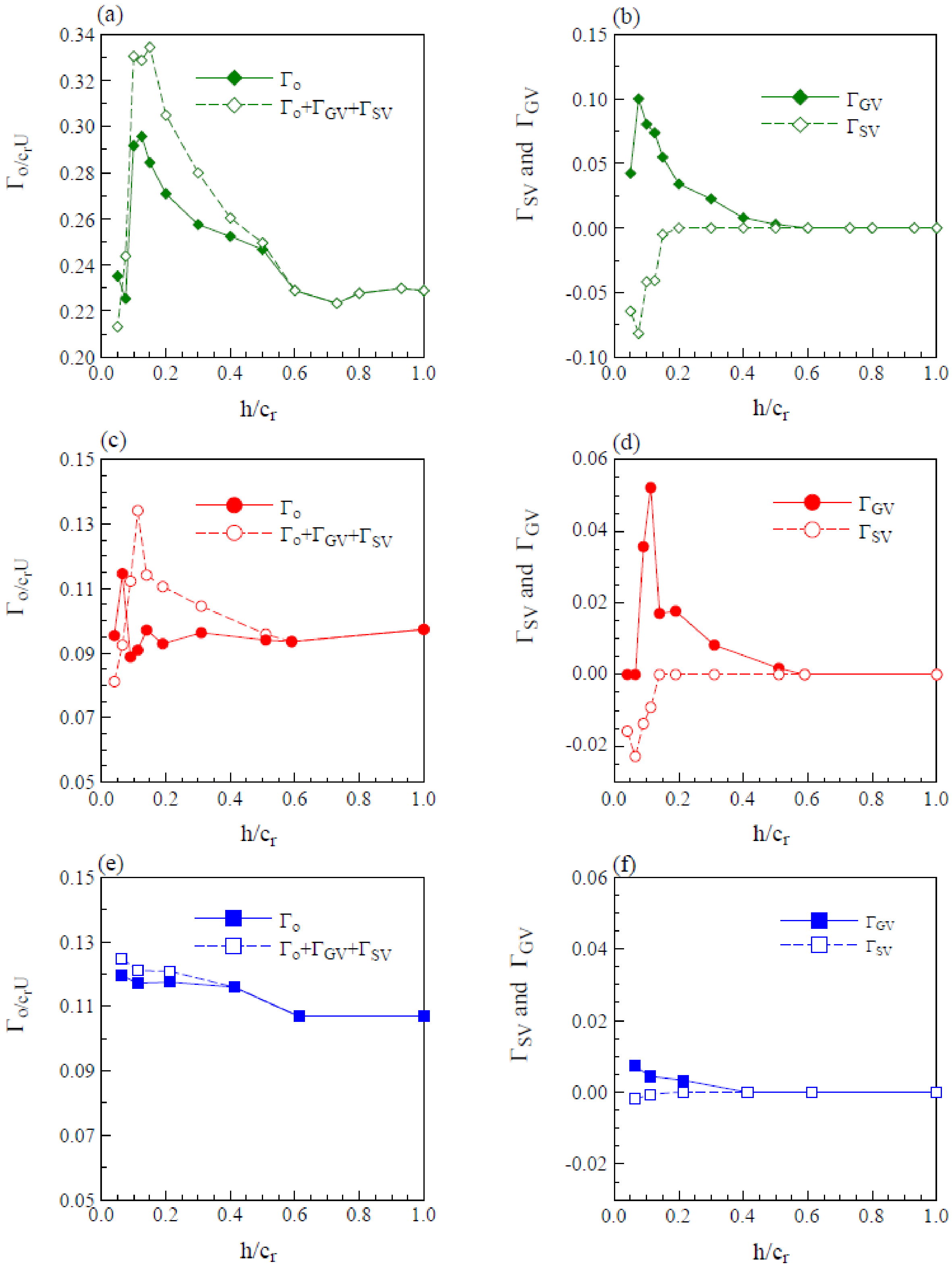

Figure 4-8 Variation of circulation of TV, GV, and SV with h/c_r. (a)-(b): RW at $\alpha = 10°$. (c)-(d): BSW at $\alpha = 8.5°$. (e)-(f): FSW at $\alpha = 10.5°$.

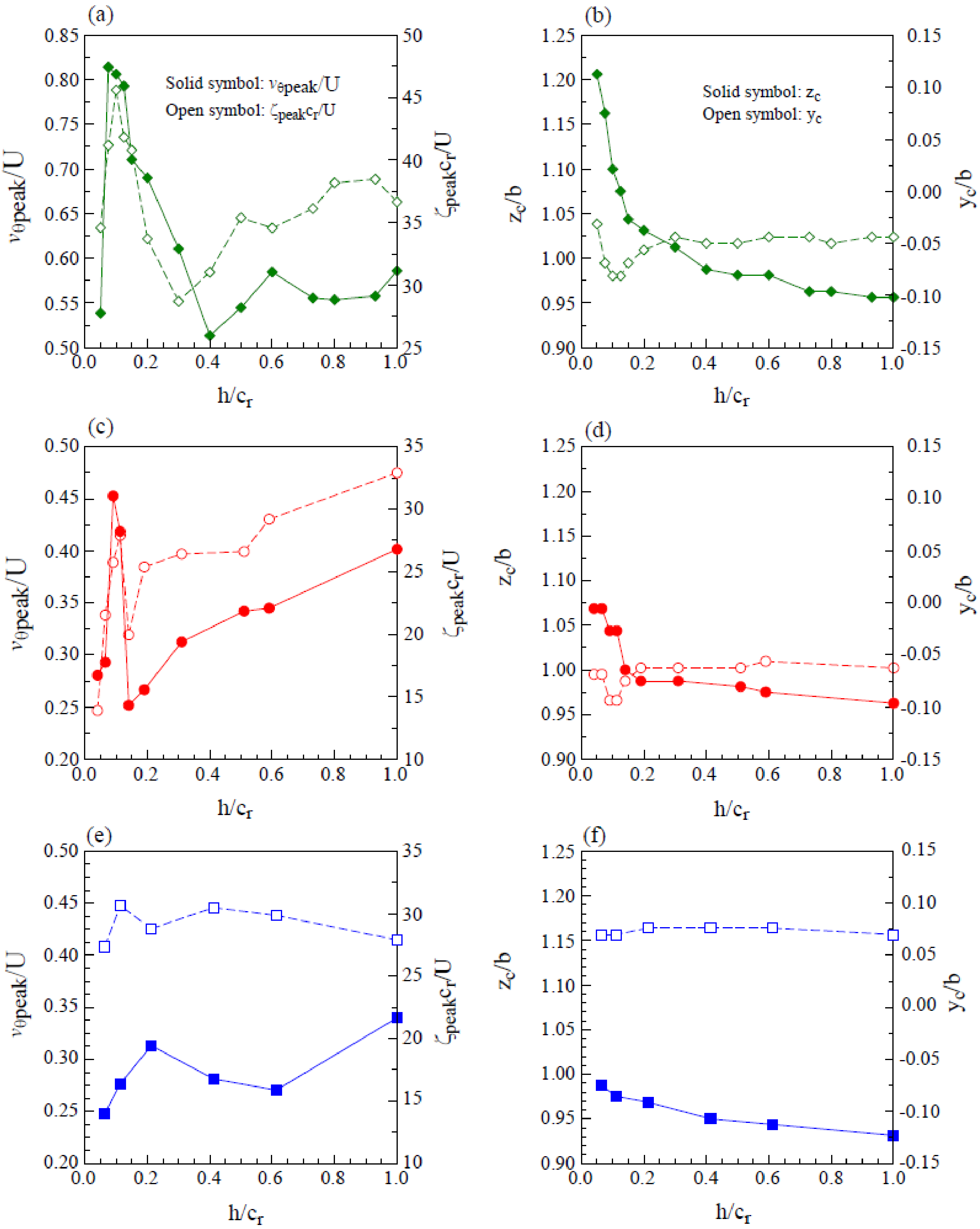

Figure 4-9 Variation of normalized $v_{\theta peak}$, ζ_{peak}, and vortex center (z_c and y_c) with h/c_r. (a)-(b): RW at α = 10°. (c)-(d): BSW at α = 8.5°. (e)-(f): FSW at α = 10.5°.

of the SWs was relatively weaker than the RW, the reduction of Γ_o due to the ground outweighed the aid from the GV.

The sharp increase in Γ_o at $h/c_r = 6.5\%$ was credited to the mergence between the tip and ground vortex. In extreme ground proximity, the GV was blended into the TV, causing it difficult to identify each vortex. Therefore, the combination of the two was simply referred to as the TV. Details of the calculation of the circulation of the multiple vortex system are given in Appendix C. With further approaching the ground, the appearance of the SV (Fig. 4-8d) negated the BSW's tip vortex strength, also leading to a steep drop in the total circulation. Nevertheless, the total circulation of the entire vortex system shows an exponential increase for $100\% > h/c_r > 11.25\%$ as the Γ_{GV} was augmented in ground effect (Figs. 4-8c-d), outweighing the loss in Γ_o. In contrast to the RW and BSW, only small changes were observed in the FSW's vortex parameters (see Figs. 4-8e-f) because a vast majority of the wing was still outside the close ground effect at the same h/c_r due to its unique geometry.

The results further show that the $v_{\theta peak}$ and ζ_{peak} of the three wings varied similarly to the Γ_o (Fig. 4-9). For the RW, the $v_{\theta peak}$ decreased gently for $h/c_r > 40\%$, followed by a sharp increase for $40\% > h/c_r > 7.5\%$ due to the presence of the GV adding vorticity to the TV. A significant reduction was observed for $h/c_r < 7.5\%$ due to the SV negating the vortex strength of the TV (Fig. 4-9a). The influence of the GV and SV on the TV can also be reflected by the variation of the ζ_{peak} (Fig. 4-9a), which peaked at $h/c_r = 10\%$ and dropped dramatically in extreme ground conditions. Outside close ground effect, the ζ_{peak} was found to decrease slightly for $h/c_r > 30\%$. Figure 4-9b further indicates that the ground proximity and the resulting ram pressure also caused a large outboard displacement of the tip vortex, leading to an increased effective aspect ratio AR_{eff} which can translate into an increased C_L and a decreased C_{Di} as compared to their OGE counterpart. In addition, at $h/c_r = 5\%$, the SV wrapping around the TV causing its rebound can be clearly seen in Fig. 4-9b. Likewise, the BSW in ground effect showed that the $v_{\theta peak}$ and ζ_{peak} varied similarly to the Γ_o decreasing persistently for $h/c_r > 12.5\%$, followed by a sharp increase and peaking at h/c_r around 11.25% due to the GV, and diminishing rapidly due to the SV (Fig. 4-9c). The ram pressure-induced outboard movement of the tip vortex and its rebound in extreme ground conditions were also observed (Fig. 4-9d). For the FSW, except for a slight outboard movement, no major changes were observed (Figs. 4-9e-f).

4.3 Variation of C_{Di} with h/c_r

In this section, the influence of the ground distance on the lift-induced drag coefficient $C_{Di} = D_i/½\rho U^2S$ will be discussed. The lift-induced drag coefficient was computed based on the vorticity distribution inferred from the measured *vw*-crossflow fields using the Maskell wake integral method (Maskell 1973) and also based on the inviscid lifting-line theory.

4.3.1 OGE

The Maskell wake integral model is expressed as below:

$$D_i = \frac{1}{2}\rho_\infty \iint_{S_2} \Psi\zeta dydz - \frac{1}{2}\rho_\infty \iint_{S_1} \phi\sigma dydz - \frac{1}{2}\rho_\infty \iint (1 - M_\infty^2)(\Delta u)^2 dydz \qquad (4.1)$$

where $\zeta = \partial w/\partial y - \partial v/\partial z$, $\sigma = \partial v/\partial y + \partial w/\partial z$, and $\psi(y,z)$ and $\phi(y,z)$ are stream function and velocity potential. Detailed discussion on C_{Di} computation can be found in Appendix B.

Figure 4-10 shows that the variation of C_{Di} (calculated based on the Maskell wake integral model) with α followed the same trend as the observed change in Γ_o with α (Fig. 4-5a), which met the expectation since C_{Di} is a direct reflection of the vorticity level contained in the vortical wake. For the RW and FSW, C_{Di} increased persistently with α owing to their root-stall characteristics resulted in an ever-growing wingtip vortex (Figs. 4-10a&c). In contrast, C_{Di} of the BSW was found to only increase up to $\alpha = \alpha_{ss}$, followed by a sharp reduction in C_{Di} due to the largely diffused tip vortex for $\alpha > \alpha_{ss}$. At $\alpha = 10°$ of the RW, a C_{Di} of 0.0301 in comparison with $C_{D,FB} = 0.062$, which translates into 48.5%, was achieved. $C_{D,FB}$ indicates the total drag coefficient measured with the force balance. However, for the SWs, because of their considerably smaller tip vortices, C_{Di} only accounted for a tiny portion of the total drag coefficient. For example, for the BSW (or FSW), at $\alpha = 8.5°$ (or 10.5°), the calculated $C_{Di} = 0.0026$ (or 0.0028) was only 3.2% (or 3.3%) of the total drag coefficient C_D. Also shown in Fig. 4-10 is the C_{Di} predicted directly using the inviscid lifting-line theory as follows:

$$C_{Di} = \frac{{C_{L,FB(OGE)}}^2}{\pi e AR_{eff}} \qquad (4.2)$$

where $C_{L,FB\ (OGE)}$ denotes the lift coefficient at different α measured with a force balance outside the ground effect, $AR_{eff} = 2b'^2/S$ is the effective aspect ratio, and $e = 0.9$ is the Oswald wing span efficiency factor. It is evident that Prandtl's classical inviscid lifting-line theory overpredicted

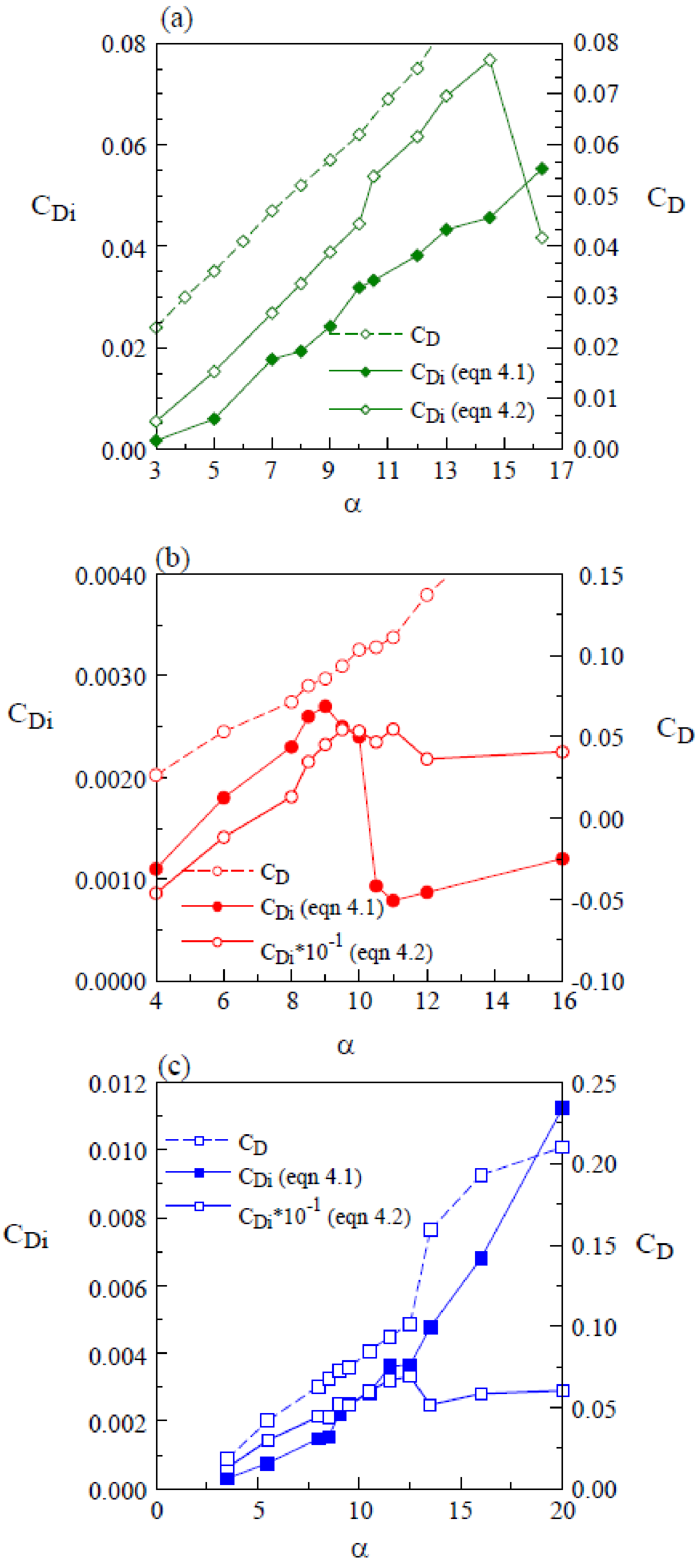

Figure 4-10 Variation of C_D and C_{Di} with α outside ground effect. (a) RW, (b) BSW, and (c) FSW.

lift-induced drag. Especially for the SWs, C_{Di} based on equation (4.2) was an order of magnitude larger than those computed based on equation (4.1). Therefore, C_{Di} from the lifting-line theory can only serve as an upper bound. The discrepancy found in the calculation of C_{Di} based on the two methods mentioned above can be attributed to the lifting-line theory assuming the flow is inviscid, whereas, in the current experiments, the Reynolds number was relatively low.

4.3.2 IGE

C_{Di} was also computed in ground effect and plotted against h/c_r in Fig. 4-11. For the RW, C_{Di} computed via the Maskell method (equation (4.1)) was found to increase slightly for $h/c_r >$ 30% and started to decrease rapidly for $h/c <$ 30% (Fig. 4-11a). The observed increase at $h/c_r >$ 30% can be credited to the presence of GV and the increased ground effect-produced ram pressure aiding the tip vortex strength. A significant reduction compared to its OGE counterpart was observed for $h/c <$ 20%, attributing to the ground effect-induced outboard movement and suppression of the tip vortex due to the SV. A 58% of C_{Di} reduction was observed at $h/c_r =$ 5%. The results matched the conclusion of Lu et al. (2019)'s work. Figure 4-11a also reveals that C_{Di} computed via equation (4.2) still overestimated C_{Di} inferred from the *vw*-crossflow measurements (via equation (4.1)) but had a similar trend.

Similarly, in ground effect, for $h/c_r >$ 19%, C_{Di} of the BSW reduced gradually compared to the OGE value and dropped rapidly between h/c_r = 19% and 9% (Fig. 4-11b). The observed reduction was consistent with the outboard movement (increase in AR_{eff}) and the reduced strength of the tip vortex in close ground proximity, as shown in Section 4.2. The rise at $h/c_r =$ 6.5% was caused by the co-rotating GV merging with the TV and adding vorticity to it. A maximum 61% C_{Di} reduction was discovered at $h/c_r =$ 4%. On the contrary, the variation of C_{Di} of the FSW was minor, increasing slightly for $h/c_r >$ 39%, which was blamed on the ground effect-induced ram pressure built-up underneath the wing's bottom surface resulting in a stronger tip vortex. Also, only a minor outboard movement was noticed for $h/c_r >$ 39%. The following slight decrease in C_{Di} can be attributed to the further outward movement of the tip vortex and the asymptotic Γ_o. C_{Di} of the SWs computed via equation (4.2) demonstrated the same decreasing trend with the reducing ground distance, but the value was still an order larger than C_{Di} computed via equation (4.1).

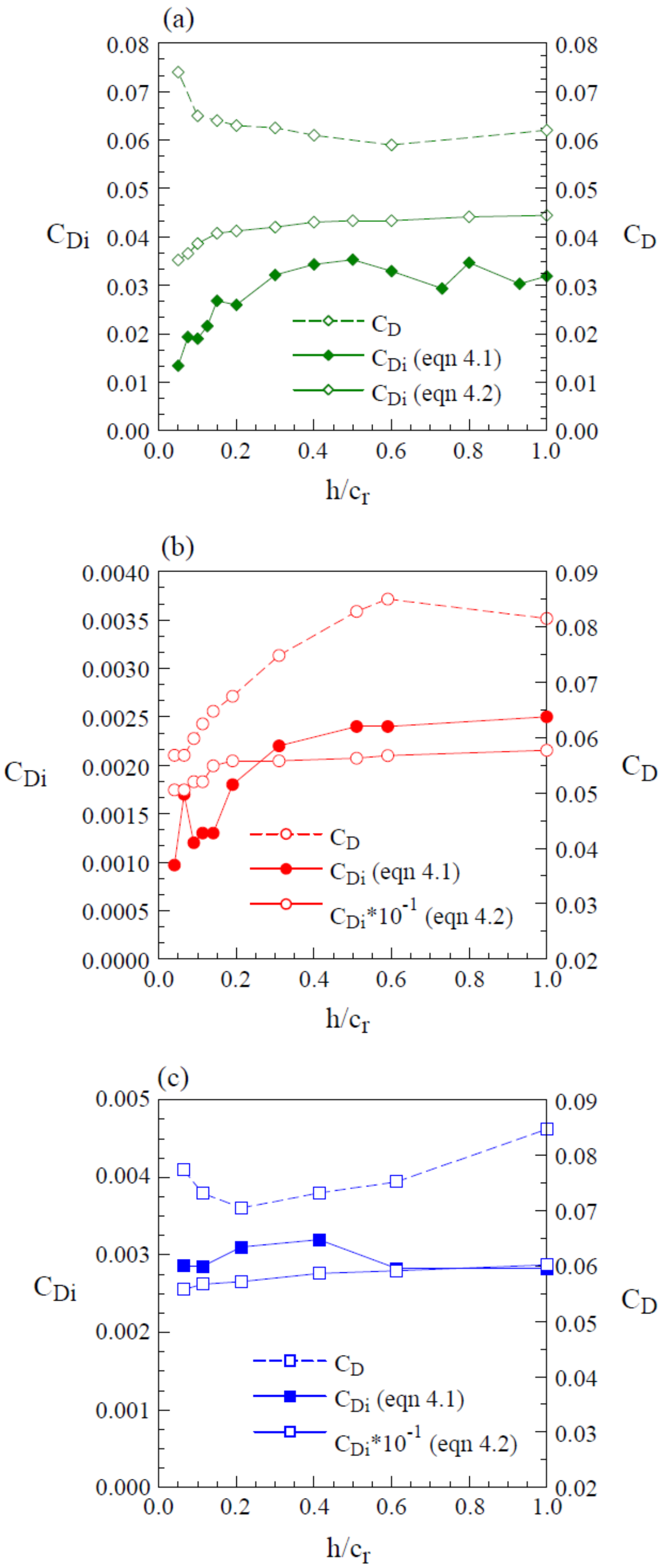

Figure 4-11 Variation of C_D and C_{Di} with h/c_r. (a) RW at $\alpha = 10°$, (b) BSW $\alpha = 8.5°$, and (c) FSW $\alpha = 10.5°$.

4.4 Variation of Spanwise Circulation Distribution with h/c_r

In this section, the characteristics of the normalized spanwise circulation $\Gamma(z)/c_rU$ distribution behind the three wings were discussed both outside and in ground effect. Prior to the discussion, we should emphasize the importance of the spanwise circulation distribution and introduce classical Prandtl’s lifting-line theory. The classical Prandtl’s lifting-line theory was the first practical theory for predicting the aerodynamic performance of a finite wing and was developed by Ludwig Prandtl in 1911. Prandtl stated that on any lifting body experiencing a force $L' = \rho_\infty V_\infty \Gamma$ from the Kutta-Joukowski theorem, there existed a vortex filament of strength Γ, called bound vortex fixed to a location in the flow as sketched in Figure 4-12. According to Helmholtz's theorem, the bound vortex cannot end at the wingtip and will continue as two trailing vortices downstream from the wingtips to infinity. Therefore, the finite wing can be replaced by a bound vortex of a shape of a horseshoe and is often mentioned as horseshoe vortex.

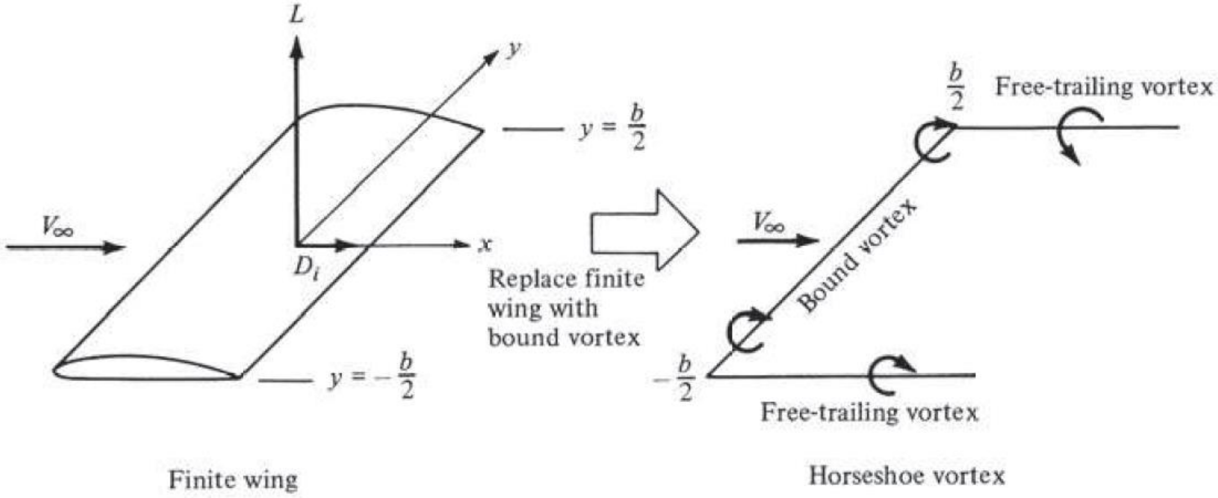

Figure 4-12 Schematic of bound vortex on a finite wing. (Anderson 2016)

However, a single horseshoe vortex was not able to represent a finite wing realistically, in that case, the downwash at the wingtip will become infinity. Prandtl solved this problem by superimposing an infinite number of horse vortices with a different length of the bound vortex coinciding along a straight line called the lifting line, as shown in Fig. 4-13.

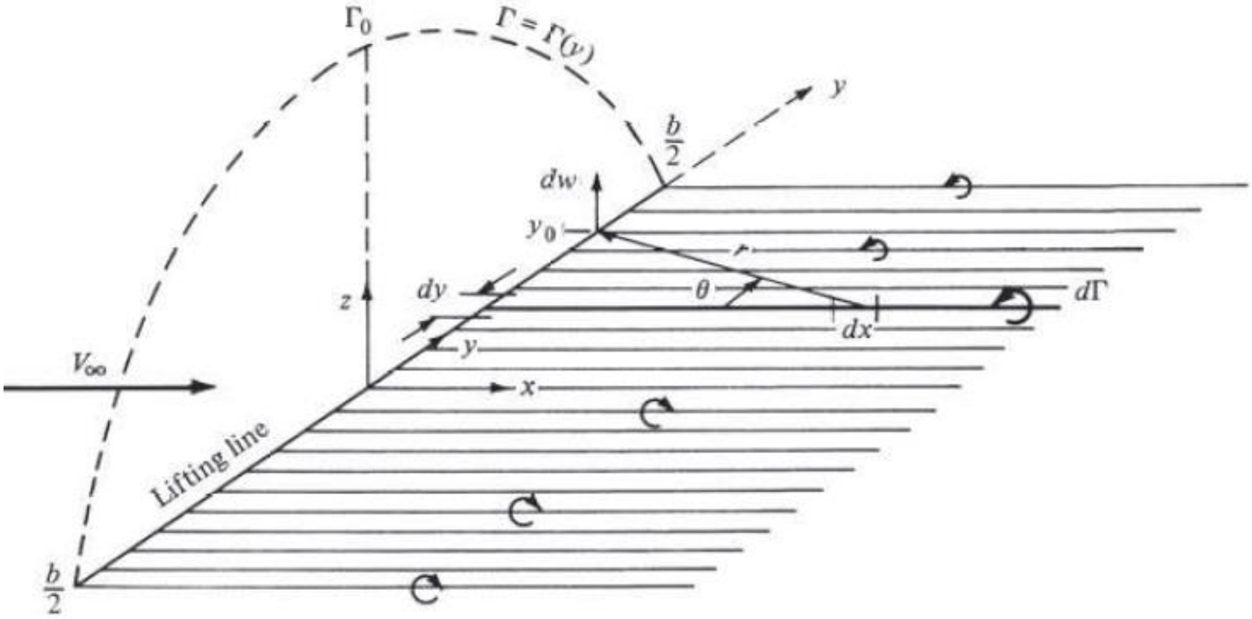

Figure 4-13 Superposition of an infinite number of horseshoe vortices along the lifting line. (Anderson 2016)

Each horseshoe vortex has a small vortex strength of dΓ. Now, the single bound vortex is substituted with a continuous distribution of Γ(z) along the wing span and the two trailing vortices become a continuous trailing vortex sheet downstream of the wing (Fig. 4-13). The circulation at an arbitrary z_o location $\Gamma(z_o)$ can be calculated by superimposing all the infinitesimal horseshoe vortices from $z = z_o$ to $z = b/2$, which can be expressed in equation (4.3):

$$\Gamma(z_o) = \int_{z_o}^{\frac{b}{2}} d\Gamma \tag{4.3}$$

The circulation at the origin is, therefore, the maximum as it is the superimposition of all the horseshoe vortices along the half span, and it is often called the root bound circulation $\Gamma_{b,m}$. According to the Kutta-Joukowski theorem, the lift distribution $L'(z) = \rho_\infty V_\infty \Gamma(z)$ can be obtained from the spanwise circulation distribution, and the total lift of the wing can be calculated by integrating the lift distribution over the entire span as follow:

$$L = \int_{-b/2}^{b/2} L'(z) dz$$

or

$$L = \rho_\infty V_\infty \int_{-b/2}^{b/2} \Gamma(z) dz \tag{4.4}$$

The significance of Prandtl’s lifting-line theory is that the trailing-vortex sheet described in theory is physically consistent with the actual flow downstream of a finite wing, implying the lifting-line theory can be applied experimentally to estimate the lift if the wake downstream the wing can be captured. In this research, the trailing vortex sheet was measured by the seven-hole pressure probe and the circulation was calculated based on the *vw*-crossflow via the Stokes Theorem by summing the vorticity multiplied by the incremental area of the measuring grid. The spanwise circulation $\Gamma(z)$ calculation was initiated from the freestream (away from the wingtip in the outboard direction) and progressed toward the wing root as indicated by the lifting-line theory. At each spanwise location, the circulation was the sum of all the circulation at the previous locations (summation of all the superimposed horseshoe vortices). Note that due to the limitation of the probe traversing mechanism, the present wake survey only encompassed 85% of the span from the wingtip. To facilitate the identification of the root bound circulation $\Gamma_{b,m}$ and calculate the total lift, the $\Gamma(z)$ distribution between z/b = 0 and 0.15 was extrapolated.

4.4.1 OGE

Figure 4-14 displays the $\Gamma(z)/c_rU$ distribution at h/c_r = 100% (or equivalently OGE) as a function of α along the three wings. The results show that regardless of wing platform and α, there was a persistent existence of a dip in the $\Gamma(z)$ distribution near the tip (z = b), demonstrating the existence of a tip vortex with a stronger circulation for $\alpha < \alpha_{ss}$ as compared to that of an elliptic wing (denoted by the open circle). The elliptic wing was named for having a circulation that varies elliptically with distance z along the span. The elliptic distribution was presented to serve as a comparison as it is theoretically the most efficient way to generate lift due to the following reason. The downwash is constant over the spanwise with such distributions, and consequently, the lift-induced drag is the minimum for a given lift since the lift-induced drag has a quadratic dependency on the downwash.

The RW had the steepest dip among the three wings since it rendered the strongest tip vortex. Figure 4-14a further indicates that outside the tip region, the value of $\Gamma(z)$ rose slowly and plateaued in the RW's root or inboard region, implying that the strength of the horseshoe vortex decreased gradually in the spanwise direction toward the root. In contrast, for the SWs,

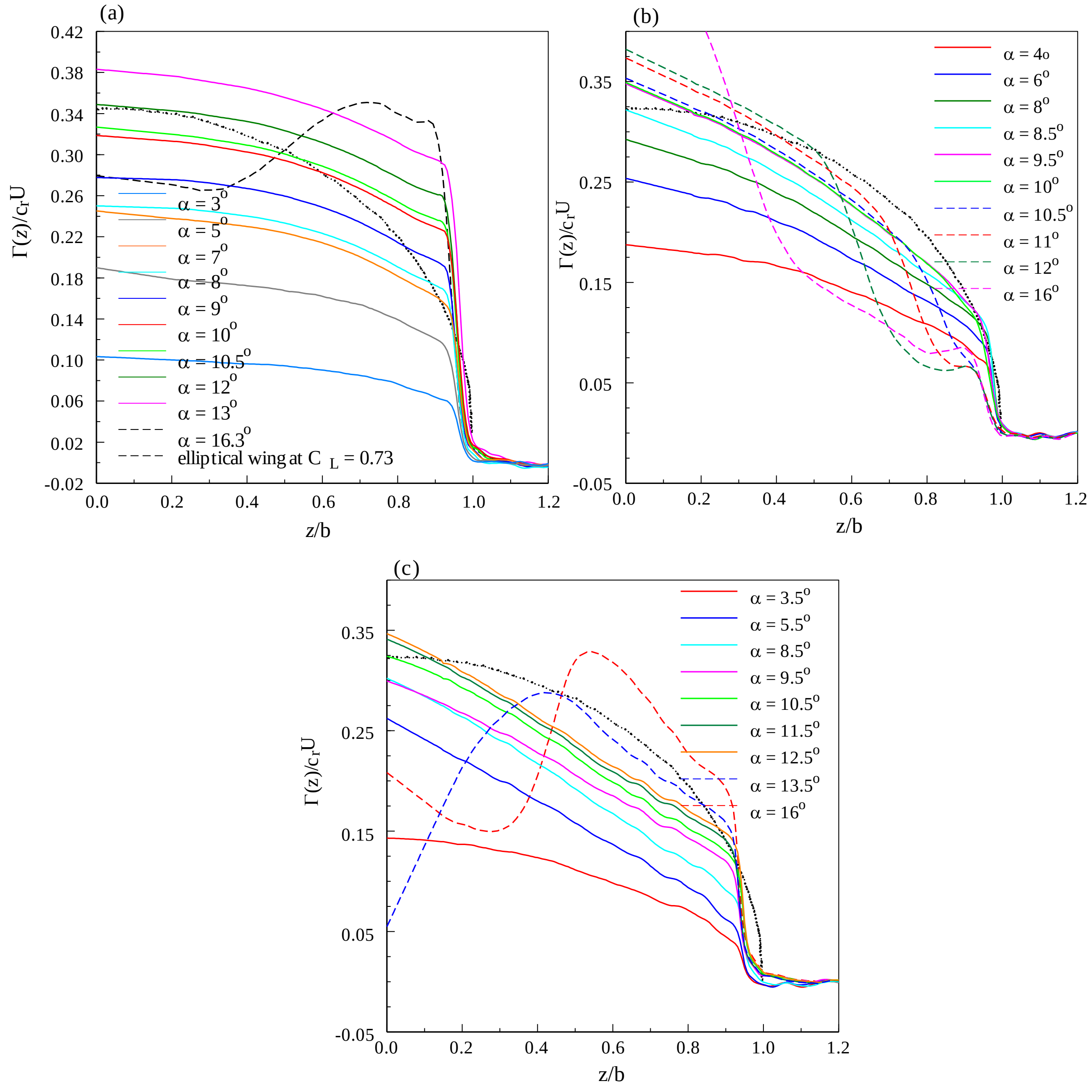

Figure 4-14 Variation of $\Gamma(z)/c_rU$ distribution with α outside the ground effect. (a) RW, (b) BSW, and (c) FSW. Dashed open circle line denotes the elliptic distribution.

the value of Γ(z) was found to increase persistently when passing the tip region (Figs. 4-14b-c). For $\alpha < \alpha_{ss}$, the extent of the dip increased continuously with increasing α regardless of the wing platforms. The difference showed up in the post stall-α region. For the BSW, a sharp reduction in the extent of the dip was observed for $\alpha > \alpha_{ss}$, attributed to the unique tip-stall characteristic of the BSW. The observed change in the extent of the dip in the $\Gamma(z)$ distribution is in agreement with the change in the total circulation of the tip vortex, as shown earlier in Fig. 4-5a. The tip stall of the BSW also translates into a persistent increase in the root bound circulation (i.e., $\Gamma(z = 0) = \Gamma_{b,m}$; see Fig. 4-15a).

Figures 4-14a&c, however, show that for the RW and FSW positioned at $h/c_r = 100\%$, the extent of the dip (indicative of the strength of Γ_o) was found to increase monotonically with increasing α attributing to the root stall characteristic, which allows the flow in the tip region remained unaffected by the massive separation flow. The stalling of the RW and FSW initiated in the root or inboard region of the FSW also led to a large drop in $\Gamma_{b,m}$ at $\alpha = 16.3°$ and 13.5°, respectively (see Fig. 4-15a). That is, at $h/c_r = 100\%$, there was a continuous increase in $\Gamma_{b,m}$ in the pre stall-α regime of the RW and FSW while a precipitous drop in $\Gamma_{b,m}$ in the post stall-α regime (Figs. 4-14a&c). Besides, the leading-edge vortex at $\alpha = 16°$ of the FSW can also be identified by the rise in $\Gamma(z)$ at around $z/b \approx 0.4$ or $z/c_r \approx 1$ (Fig. 4-14c), which is in agreement with the iso-ζ/c_rU contour displayed in Fig. 4-4t.

The $\Gamma(z)$ distributions presented in Fig. 4-14 were also integrated to compute the total lift coefficient $C_{L,\Gamma(z)}$ ($= L/½\rho U^2 S$ where L is the lift force, ρ is the density of the fluid, and S is the wing area). The lift L was computed via equation (4.4). Figure 4-15b shows that outside the ground effect, the $C_{L,\Gamma(z)}$ (computed based on equation (4.4)) of the RW was found to be in good agreement with the $C_{L,FB}$ (lift coefficient obtained directly with the force balance). At $\alpha = 10°$, the computed $C_{L,\Gamma(z)} = 0.6479$ accounts for 98% of $C_{L,FB} = 0.661$. The computed lift coefficient deviated slightly from the direct force balance data when α was close to the stalling. The computed $C_{L,\Gamma(z)}$ of the BSW, which increased continuously with increasing α for $\alpha < \alpha_{ss}$, followed by a slight reduction with a further increase in the angle of attack, also showed great consistency with the $C_{L,FB}$ (Fig. 4-15c). For $\alpha \geq \alpha_{ss}$, the computed C_L was found to be about 10% lower than the force-balance data, which can be due to the large dissipation of the tip vortex at $\alpha \geq \alpha_{ss}$.

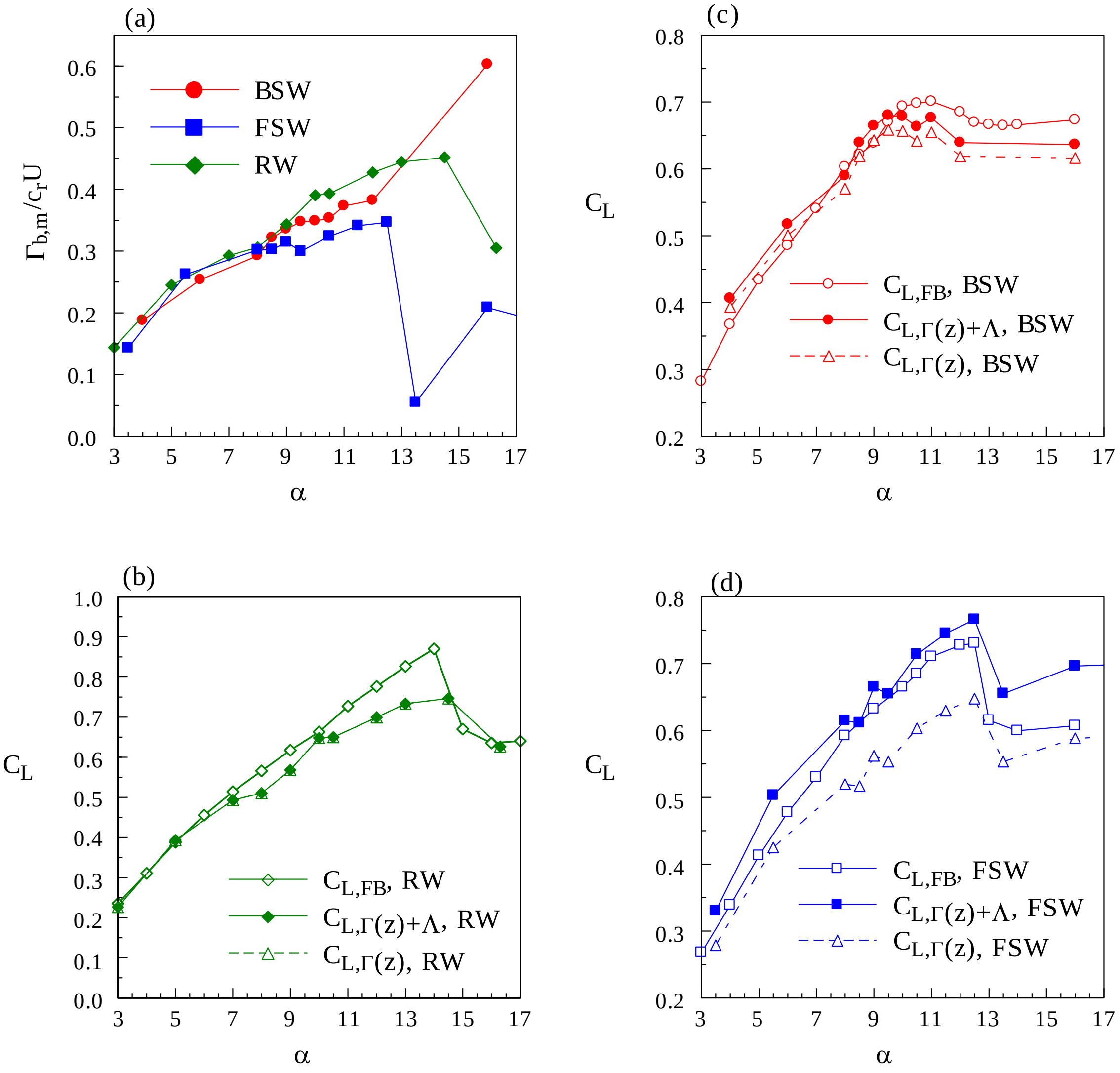

Figure 4-15 Variation of $\Gamma_{b,m}$, $C_{L,\Gamma(z)}$, and $C_{L,\Gamma(z)+\Lambda}$ with α outside ground effect.

Nevertheless, $C_{L,\Gamma(z)}$ of the FSW was, however, observed to be significantly lower than the $C_{L,FB}$ at the same α (Fig. 4-15d). The large discrepancy was due to the fact that the classic Prandtl lifting-line theory assumed a straight and horizontal sheet of trailing vortex segments to simplify the calculation. However, Smith (1996) concluded that the effect of the skewed wake vortex sheet (resulting from the Λ_{TE} as discussed in Section 4.2) is significant that the classical Prandtl lifting-line theory was not applicable for swept wings. Since the $\Lambda_{TE} = 32.3°$ of the FSW was almost 2.5 times larger than the BSW ($\Lambda_{TE} = 14.5°$), the computed $C_{L,\Gamma(z)}$ of FSW, therefore, failed to predict the lift. By considering the effect of the trailing edge sweep angle, the greatly underestimated $C_{L,\Gamma(z)}$ value of the FSW was improved via the modified lifting-line theory:

$$L = \rho U \int_{-\frac{b}{2}}^{\frac{b}{2}} \Gamma(z_\Lambda)\, dz_\Lambda \qquad (4.5)$$

where $z_\Lambda = z/\cos(\Lambda_{TE})$. As can be seen in Figs. 4-15c-d, the magnitude of $C_{L,\Gamma(z)+\Lambda}$ of the swept wing models (calculated based on equation (4.5)) was in agreement with the direct force balance measurement for $\alpha < \alpha_{ss}$. At $\alpha = 8°$, for example, the computed $C_{L,\Gamma(z)+\Lambda} = 0.589$ (or 0.615) of the BSW (or FSW) accounts for 97.6% (or 103.8%) of $C_{L,FB} = 0.603$ (or 0.592). The deviation between the computed $C_{L,\Gamma(z)+\Lambda}$ and the force balance data still existed in the post stall-α regime, which can be attributed to the largely dissipated (or the ever-growing) tip vortex for the BSW (or FSW). Since the modified approach (equation (4.5)) demonstrated better lift prediction, the modified approach will be applied to all the wings for the rest of this study.

4.4.2 IGE

In ground effect, the $\Gamma(z)$ distributions were also plotted against h/c_r = 5% to 100% at α = 10° of the RW, 8.5° of the BSW and 10.5° of the FSW (Fig. 4-16). Figure 4-16 shows that the tip vortex-produced dip in the $\Gamma(z)$ distributions observed outside ground effect persisted in ground effect for all wings. For the RW, the extent of the dip was found to increase persistently (agree with the change in Γ_o; see Fig. 4-8a) for h/c_r > 15% due to the presence of ground vortex (Fig. 4-16a). Consequently, the $\Gamma_{b,m}$ also increased continuously up to h/c_r = 15%. Accompanied by that was an outboard movement of the dip, suggesting an increased effective aspect ratio AR_{eff} and C_L. For h/c_r < 10%, negative $\Gamma(z)$ was observed for $z/b > 1$, which originated from the SV in close ground effect. The appearance of the secondary vortex also negated the vortex strength of the tip vortex, and the result was a sharp reduction in the $\Gamma_{b,m}$ (Fig. 4-17a).

As for the BSW, the $\Gamma(z)$ distributions were observed to be largely unaffected except for a small outboard movement of the dip for $h/c_r \geq 19\%$ (Fig. 4-16b), associated with which was a modest drop in $\Gamma_{b,m}$ (Fig. 4-17a). For 19% > h/c_r > 6.5%, the dip became sharper and was pushed outboard to a more considerable extent, consistent with the results in Fig. 4-9d, indicating an increased effective aspect ratio and, consequently, an increased C_L (Fig. 4-17c). Negative $\Gamma(z)$ was also observed for $z/b > 1$ and h/c_r < 9% of the BSW, resulting from the secondary vortex-caused vorticity reduction of the tip vortex. The consequence was a significant drop in the bound root circulation $\Gamma_{b,m}$ for h/c_r < 9% (Fig. 4-17a).

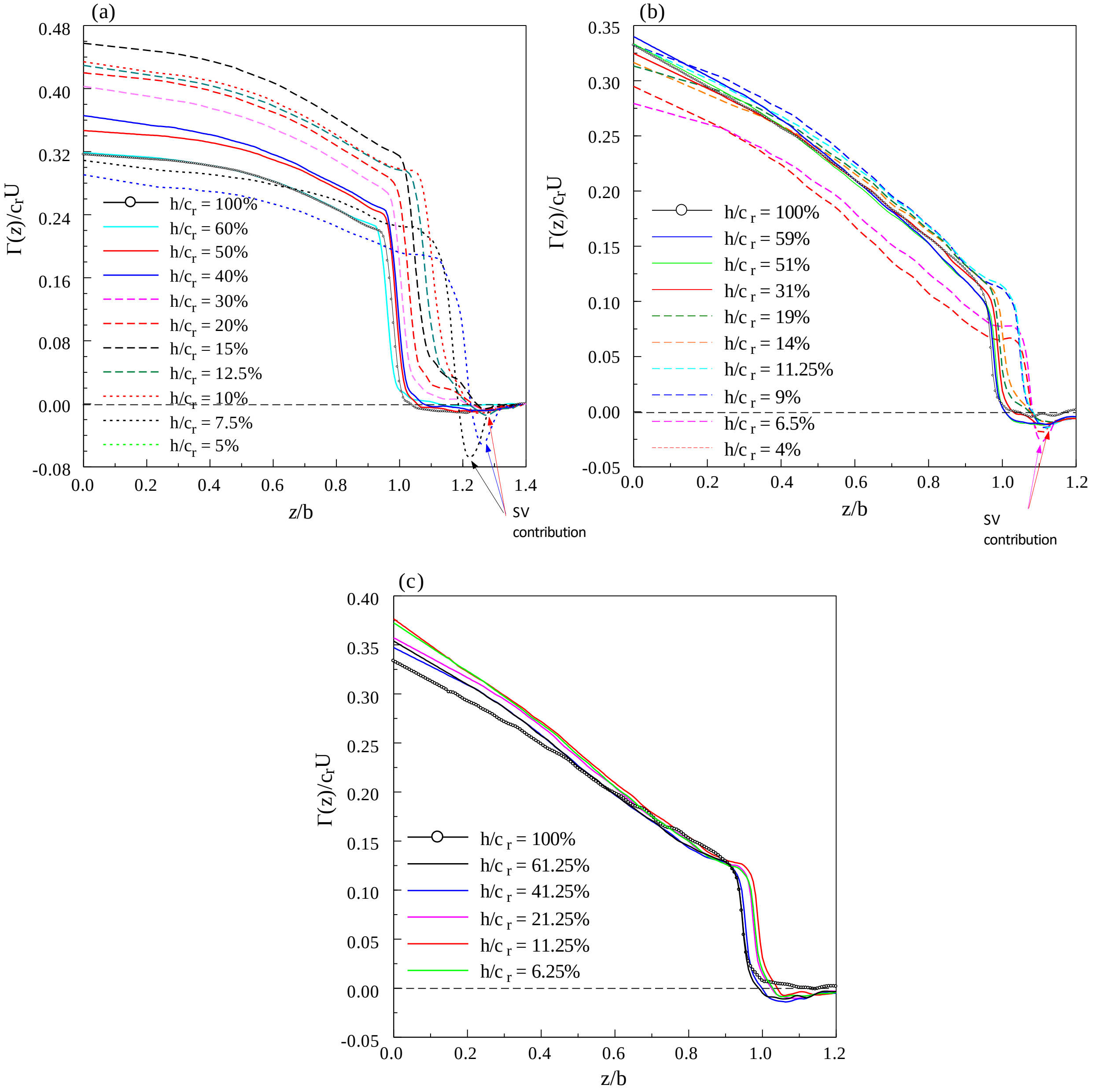

Figure 4-16 Variation of $\Gamma(z)/c_rU$ distribution with h/c_r at fixed α. (a) RW at α = 10°, (b) BSW α = 8.5°, and (c) FSW α = 10.5°.

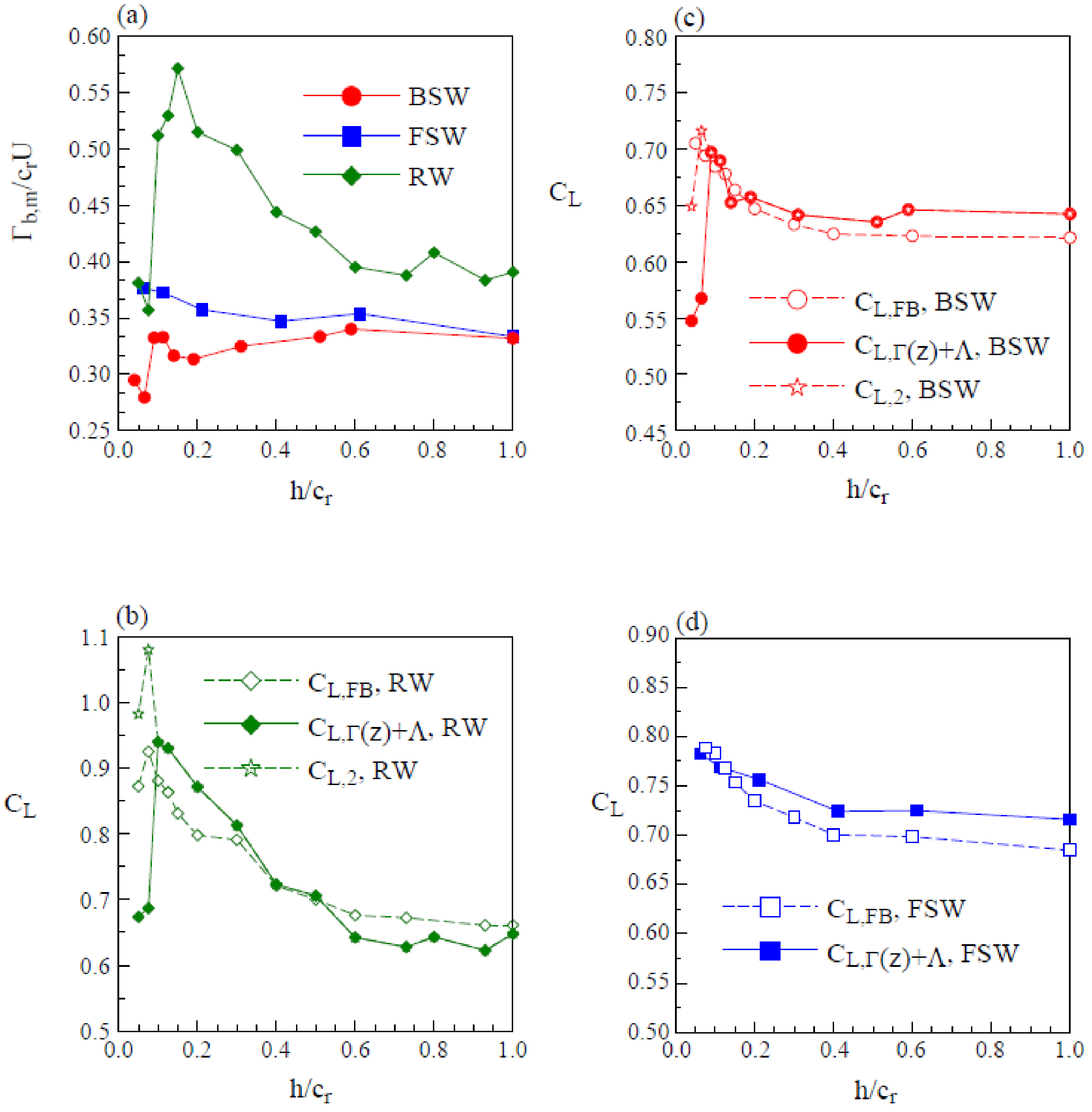

Figure 4-17 Variation of $\Gamma_{b,m}$, $C_{L,\Gamma(z)+\Lambda}$, and $C_{L,2}$ with h/c_r at fixed α. (b) RW at α = 10°, (c) BSW α = 8.5°, and (d) FSW α = 10.5°.

In contrast to the RW and BSW, the change in the $\Gamma(z)$ distribution of the FSW was less pronounced (Fig. 4-16c). With the decreasing h/c_r, the dip near the tip region was found to become steeper and shifted slightly outboard due to the wingtip vortex with stronger vortex strength, which also led to a higher $\Gamma_{b,m}$ (Fig. 4-17a).

The lift coefficient $C_{L,\Gamma(z)+\Lambda}$ was also computed based on equation (4.5) in ground effect and was plotted against h/c_r in Figs. 4-17b-d for the three wings. Figures 4-17b-c demonstrate that the calculated lift coefficient $C_{L,\Gamma(z)+\Lambda}$ for the RW and BSW were in great consistency with the direct force balance measurements for $h/c_r \geq 9\%$. For the BSW, at $h/c_r = 9\%$, the computed lift coefficient $C_{L,\Gamma(z)+\Lambda}$ was 0.697, which accounted for 101% of $C_{L,FB}$, whereas, for the RW, at $h/c_r = 10\%$, $C_{L,\Gamma(z)+\Lambda}$ was 0.94, which accounted for 106% of $C_{L,FB}$. However, the spanwise circulation integration greatly underestimated the force balance data for $h/c_r < 9\%$, which can be attributed to the secondary vortex with vorticity of the opposite sign adding negative vorticity to the tip vortex diminishing its vortex strength. As a result, the dip in the spanwise circulation distribution was shortened (Figs. 4-16a-b).

Besides, the presence of the SV shifted the entire spanwise circulation distribution downward toward the negative side. Both factors resulted in the significantly lowered computed $C_{L,\Gamma(z)+\Lambda}$ value. Therefore, since the impact of the SV was so significant in close ground proximity, the hypothesis was established that, rather than negating the vorticity, the absolute magnitude of the vorticity of the secondary vortex should be added back to the trailing vortex system in close ground proximity. Figure 4-18 displays the real normalized $\Gamma(z)/c_rU$ distribution ($\Gamma(z)_{total}$) and the circulation distribution with the hypothesis of considering the contribution of the SV additive ($\Gamma(z)_{TV+GV} + |\Gamma(z)_{SV}|$) for RW and BSW and $h/c_r < 9\%$. It is evident in Figs. 4-17b-c that the magnitude of $C_{L,2}$ (obtained through the integration of $\Gamma(z)_{TV+GV} + |\Gamma(z)_{SV}|$ distribution displayed in Fig. 4-18) significantly improved the lift estimation.

Lastly, The $C_{L,\Gamma(z)+\Lambda}$ of the FSW, whereas, followed the $C_{L,FB}$ for all h/c_r (i.e. at $h/c_r = 11.25\%$, $C_{L,\Gamma(z)+\Lambda} = 0.768$ accounted for 98% of $C_{L,FB}$; see Fig. 4-17d). The reason can be attributed to its unique wing configuration, which allowed the trailing wake vorticity sheet not to be affected by the multiple vortex system and the presence of the ground.

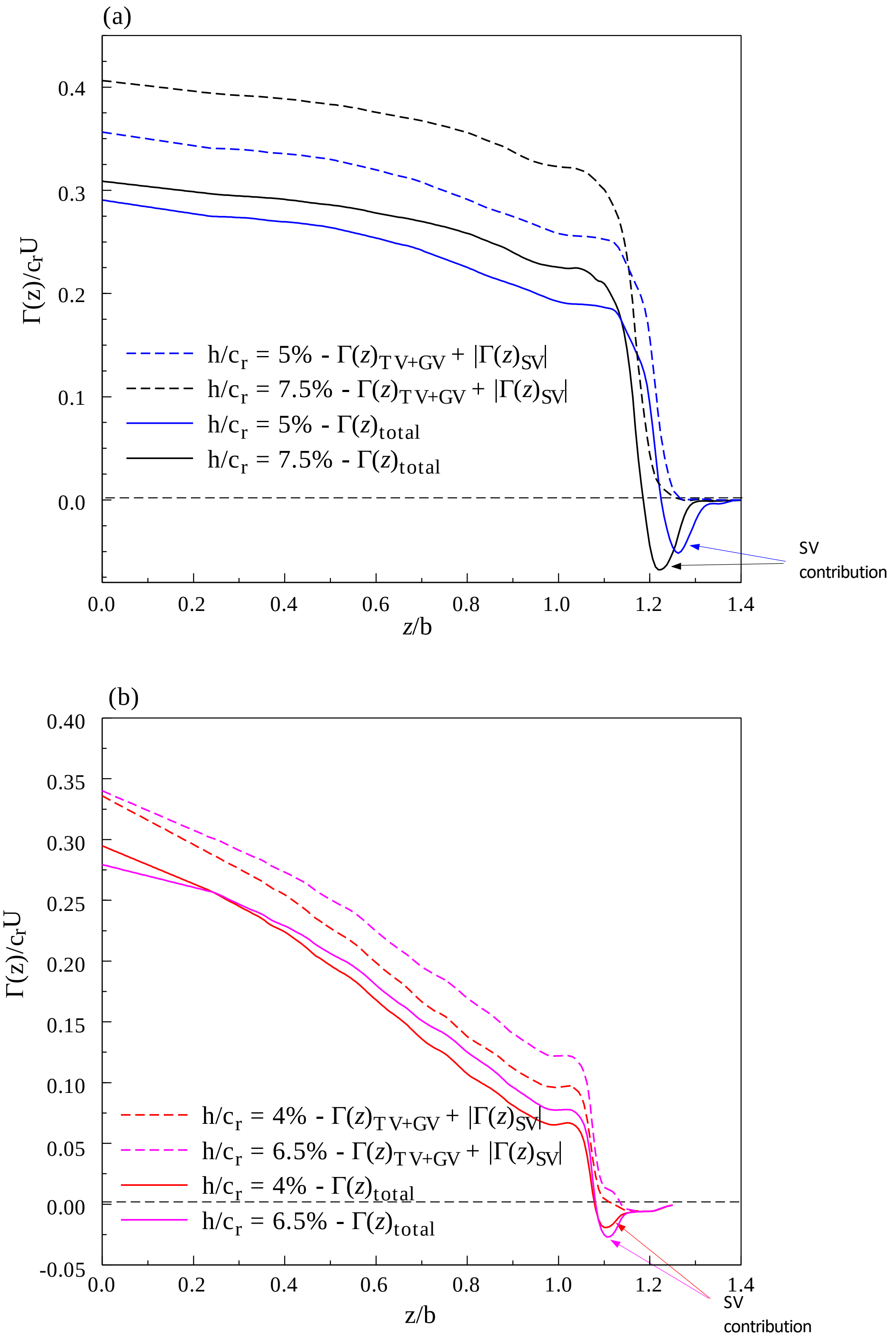

Figure 4-18 Normalized $\Gamma(z)_{total}$ and $\Gamma(z)_{TV+GV} + |\Gamma(z)_{SV}|$ distribution. (a) RW at $\alpha = 10°$, and (b) BSW at $\alpha = 8.5°$.

5 Conclusion

The objective of this thesis project was to investigate the impact of ground proximity on aerodynamics and the near-field vortical wake behind the rectangular wing, tapered backward swept wing, and tapered forward swept wing, that will facilitate the development of the ground effect vehicles in the future. In addition, the results measured outside ground effect were also presented to serve as a comparison.

Outside ground effect, the force balance measurements showed an abrupt reduction in the lift coefficient C_L when the angle of attack was larger than the static-stalling angle for the rectangular wing and forward swept wing owing to their root stall characteristic. Accompanied by that was a shoot-up in the drag coefficient for $\alpha > \alpha_{ss}$. Additionally, the seven-hole pressure probe measurements demonstrated that the tip vortex strength increased persistently with the angle of attack due to the root stall that allowed the outboard of the wing to remain attached. By contrast, the backward swept wing had a much more gradual C_L reduction in the post stall-α regime due to its outboard spanwise flow-induced unique tip stall. C_D was observed to increase rather linearly with increasing angle of attack. In addition, the tip stall resulted in a monotonic increase in the tip vortex strength only up to the static-stall angle, followed by a drastic drop in the post stall-α regime. The lift-induced drag coefficient C_{Di} was also computed based on the trailing vortical wake flow field. The variation of C_{Di} with α for the three wings followed the same trend as the total circulation of the tip vortex. However, C_{Di} of the swept wings was significantly smaller than that of the rectangular wing, which can be attributed to their weak tip vortex strength.

The lift force of the three wings was estimated based on the spanwise circulation distribution inferred from the *vw*-crossflow measurement as dedicated in the classic Prandtl lifting line theory. The computed lift force of the rectangular wing and backward swept wing was found to agree with the force balance data. However, the lifting line theory failed to predict the lift force of the forward swept wing, which was blamed on the large trailing-edge sweep angle skewing its lifting line. By considering the effect of the trailing-edge sweep angle, the calculated force of the forward sweep wing was found to match that of the force-balance data.

In ground effect, the lift of all wings was generally found to increase with decreasing ground distance, which mainly resulted from the chord-dominated ground effect-induced ram pressure increase on the wings' lower surface. In the meanwhile, the ground effect reduced the drag at the same lift conditions. The reduction in drag on the rectangular wing was primarily due to the reduction in C_{Di}, while on the backward swept wing and forward swept wing, it was attributed to the reduction in form drag, since C_{Di} was so small. However, a lower-than-OGE C_L value was observed at small angles of attack, which can be avoided by using a flat bottom wing. The increased adverse pressure gradient in close ground effect promoted the stalling of the rectangular wing and forward swept wing, whereas the stalling of the backward swept wing was delayed. For all wings, aerodynamic efficiency (lift-to-drag ratio) was improved significantly in close ground proximity, with the backward swept wing benefitting the most from the close ground effect.

At $x/c_r = 2.5$, the iso-vorticity contours showed that, in close ground proximity, there was the appearance of a multiple vortex system behind the rectangular wing and backward swept wing, consisting of a tip vortex, a co-rotating ground vortex and a counter-rotating secondary vortex. The ground vortex, which originated from the recirculation region underneath the wing, adds vorticity to the tip vortex, resulting in a sharp increase in the peak vorticity and peak tangential velocity at around $h/c_r = 10\%$. The counter-rotating secondary vortex is related to the rolling up of the longitudinal boundary layer, which negates the vorticity of the tip vortex and also causes a vortex rebound. In addition, the ground effect pushes the tip vortex outboard in the horizontal direction, implying an increase in the effect aspect ratio AR_{eff}. Similar to the OGE case, the lift-induced drag was also found to follow the change in the tip vortex strength. The induced drag of the rectangular wing and backward swept wing reduced drastically for ground distance less than 20% chord due to the ground effect-produced outboard movement and suppression of the tip vortex, while a minor change in the lift-induced drag was observed for the forward swept wing.

The computed force of the rectangular wing and backward swept wing also showed great consistency with the force-balance measurement for $h/c_r > 10\%$. The C_L computation, however, significantly underestimated the force-balance data for $h/c_r < 10\%$ due to the secondary vortex. By treating the contribution of the secondary vortex to the multiple vortex system as additives, the C_L computation in close ground proximity was significantly improved and agreed well with that of the force-balance data. On the other hand, the unique geometry of the forward swept wing kept the inboard region of the wing in close ground proximity but always left the tip region away from the close ground proximity, making the multiple vortex system almost indiscernible. Therefore, the C_L computation matched the force-balance data for all h/c_r.

To consolidate the present findings, a moving ground boundary condition, which a moving belt system can achieve, is needed since the moving ground and stationary ground boundary conditions lead to discrepancies in aerodynamic performance and the trailing vortical wake. Also, the moving ground can better simulate the realistic take-off and landing of the ground effect vehicle. Furthermore, the progression of the vortical wake in ground effect along the backward and forward swept wings in the streamwise direction is highly desired to find out the reason behind the drag reduction and the delayed stalling of the backward swept wing. Lastly, tests conducted at higher Reynolds numbers are also highly recommended.

References

Adhikari, Dibya Raj, Manoj Prabakar Sargunaraj, Carlos E. Soto, Samik Bhattacharya, George E. Loubimov, and Michael P. Kinzel. 2020. "Unsteady Ground Effects On A Rectangular And Swept Wing Undergoing Heaving And Pitching During Deceleration." In *AIAA Scitech 2020 Forum*, In AIAA SciTech Forum. American Institute of Aeronautics and Astronautics.

Ahmed, M. R., T. Takasaki, and Y. Kohama. 2007. "Aerodynamics of a NACA4412 Airfoil in Ground Effect." *AIAA Journal* 45 (1): 37-47. https://doi.org/10.2514/1.23872.

Anderson, Elgin A., and Todd A. Lawton. 2003. "Correlation Between Vortex Strength and Axial Velocity in a Trailing Vortex." *Journal of Aircraft* 40 (4): 699-704. https://doi.org/10.2514/2.3148.

Anderson. 2016. *Fundamentals of Aerodynamics*. 6th ed. Columbus, OH: McGraw-Hill Education.

Barber, T. J., E. Leonardi, and R. D. Archer. 2002. "Causes for discrepancies in ground effect analyses." *The Aeronautical Journal* 106 (1066): 653-668. https://doi.org/10.1017/S0001924000011726.

Barlow, J. B., Rae, W. H., and Pope, A. 1999. *Low-speed wind tunnel testing*. 3rd ed. New York, Wiley.

Birch, D., T. Lee, F. Mokhtarian, and F. Kafyeke. 2003. "Rollup and Near-Field Behavior of a Tip Vortex." *Journal of Aircraft 40* (3): 603-607. https://doi.org/10.2514/2.3137.

Black, Joseph. 1956. "Flow Studies of the Leading Edge Stall on a Swept-Back Wing at High Incidence." *The Aeronautical Journal* 60 (541): 51-60. https://doi.org/10.1017/S0368393100132390.

Bleischwitz, R., R. de Kat, and B. Ganapathisubramani. 2018. "Near-wake characteristics of rigid and membrane wings in ground effect." *Journal of Fluids and Structures* 80: 199-216. https://doi.org/10.1016/j.jfluidstructs.2018.03.007.

Bleischwitz, R. 2016. “Fluid-Structure Interactions of Membrane Wings in Free-Flight and in Ground-Effect.” Ph.D. thesis, University of Southampton.

Breitsamter, Christian, and Boris Laschka. 2001. "Vortical Flowfield Structure at Forward Swept-Wing Configurations." *Journal of Aircraft* 38 (2): 193-207. https://doi.org/10.2514/2.2758.

Chigier, N. and Corsiglia, V.. 1971. *Tip vortices - Velocity distributions*. Moffett Field: Ames Research Center, NASA-TM-X-62087.

Chow, Jim S., Gregory G. Zilliac, and Peter Bradshaw. 1997. "Mean and Turbulence Measurements in the Near Field of a Wingtip Vortex." *AIAA Journal* 35 (10): 1561-1567. https://doi.org/10.2514/2.1.

Chun, H., Park, I., Chung, K., and M. Shin. 1996. "Computational and experimental studies on wings in ground effect and a WIG effect craft." Workshop proceedings of Ekranoplans and very fast craft, University of New South Wales, 5 December, 38-60.

Coe, P. and Thomas, J. 1979. *Theoretical and Experimental Investigation of Ground-Induced Effects for a Low-Aspect-Ratio Highly Swept Arrow-Wing Configuration*. Washington D.C.: NASA Scientific and Technical Information Branch, NASA-TM-80041.

Corjon, Alexandra, and Thierry Poinsot. 1997. "Behavior of Wake Vortices Near Ground." *AIAA Journal* 35 (5): 849-855. https://doi.org/10.2514/2.7457.

Corsiglia, V. R., R. G. Schwind, and N. A. Chigier. 1973. "Rapid Scanning, Three-Dimensional Hot-Wire AnemometerSurveys of Wing-Tip Vortices." *Journal of Aircraft* 10 (12): 752-757. https://doi.org/10.2514/3.60301.

Curry, Robert, Bryan Moulton, and John Kresse. 1990. *An in-Flight investigation of ground effect on a forward-swept wing airplane*. Edwards: NASA Dryden flight research Center.

Deng, Ning, and Ramesh K. Agarwal. 2022. "Numerical simulation of DLR-F6 wing-body flow field in ground effect." *Computers & Fluids* 245: 105576. https://doi.org/10.1016/j.compfluid.2022.105576.

Devenport, William J., Michael C. Rife, Stergios I. Liapis, and Gordon J. Follin. 1996. "The structure and development of a wing-tip vortex." *Journal of Fluid Mechanics* 312: 67-106. https://doi.org/10.1017/S0022112096001929.

Doig, Graham, J. Barber Tracie, and J. Neely Andrew. 2012. "Aerodynamic Characteristics of a Swept Wing in Close Ground Proximity at High Subsonic Mach Numbers." *Journal of Aerospace Engineering* 25 (4): 600-612. https://doi.org/10.1061/(ASCE)AS.1943-5525.0000169.

El-Ramly, Z., W. J. Rainbird, and D. G. Earl. 1976. "Wind Tunnel Measurements of Rolling Moment in a Swept-Wing Vortex Wake." *Journal of Aircraft* 13 (12): 962-967. https://doi.org/10.2514/3.58736.

Gerontakos, P., and T. Lee. 2006. "Near-field tip vortex behind a swept wing model." *Experiments in Fluids* 40 (1): 141-155. https://doi.org/10.1007/s00348-005-0056-y.

Han, Cheolheui, and Jinsoo Cho. 2005. "Unsteady Trailing Vortex Evolution Behind a Wing In Ground Effect." *Journal of Aircraft* 42 (2): 429-434. https://doi.org/10.2514/1.6477.

Harper, C.W. and Ralph L. Maki. 1964. *A review of the stall characteristics of swept wings*. Moffett Field: Ames Research Center, NASA TN D-2373.

Harvey, J. K., and F. J. Perry. 1971. "Flowfield produced by trailing vortices in the vicinity of the ground." *AIAA Journal* 9 (8): 1659-1660. https://doi.org/10.2514/3.6415.

Hayashi, M., and E. Endo. 1978. "Measurement of flowfield around an airfoil section with separation. " *Japan Society of Aeronautics and Space Science Transactions* 21(52): 69-75.

Hsiun, Chih-Min, and Cha'o-Kuang Chen. 1996. "Aerodynamic characteristics of a two-dimensional airfoil with ground effect." *Journal of Aircraft* 33 (2): 386-392. https://doi.org/10.2514/3.46949.

Lee, Juhee, Chang-Suk Han, and Chang-Hwan Bae. 2010. "Influence of Wing Configurations on Aerodynamic Characteristics of Wings in Ground Effect." *Journal of Aircraft* 47 (3): 1030-1040. https://doi.org/10.2514/1.46703.

Lee, T., and S. Choi. 2015. "Wingtip Vortex Control Via Tip-Mounted Half-Delta Wings of Different Geometric Configurations." *Journal of Fluids Engineering* 137 (12). https://doi.org/10.1115/1.4030852.

Lee, T., and L. S. Ko. 2009. "Vortex Wake Generated Behind a Forward Swept Wing." *Journal of Aircraft* 46 (2): 717-721. https://doi.org/10.2514/1.39352.

Lu, A., and T. Lee. 2020. "Effect of Ground Boundary Condition on Near-Field Wingtip Vortex Flow and Lift-Induced Drag." *Journal of Fluids Engineering* 143 (3). https://doi.org/10.1115/1.4048875.

Lu, A., V. Tremblay-Dionne, and T. Lee. 2019. "Experimental Study of Aerodynamics and Wingtip Vortex of a Rectangular Wing in Flat Ground Effect." *Journal of Fluids Engineering* 141 (11). https://doi.org/10.1115/1.4043593.

Maskell, E. C. 1973. *Progress towards a method for the measurement of the components of the drag of a wing of finite span*. Royal Aircraft Establishment, RAE TR 72232.

Mcalister, K. W. and R. K. Takahashi. 1991. *NACA 0015 wing pressure and trailing vortex measurements.* Moffett Field: Ames Research Center, NASA-91-A-003

Moffat, R. J. 1982. "Contributions to the Theory of Single-Sample Uncertainty Analysis." *Journal of Fluids Engineering* 104 (2): 250-258. https://doi.org/10.1115/1.3241818.

Naik, D. A., and C. Ostowari. 1990. "Effects of nonplanar outboard wing forms on a wing." *Journal of Aircraft* 27 (2): 117-122. https://doi.org/10.2514/3.45906.

Nangia, R. K. 1982. "Aspects of forward swept wing research at the University of Bristol." Proceedings of the International Conference on Forward Swept Wing Aircraft, University of Bristol, Bristol, U.K.

Orloff, Kenneth L. 1974. "Trailing Vortex Wind-Tunnel Diagnostics with a Laser Velocimeter." *Journal of Aircraft* 11 (8): 477-482. https://doi.org/10.2514/3.60371.

Pate, David J., and Brian J. German. 2014. "Superposition of Spanwise Circulation Distributions: Accuracy Assessment and Application in Wing Design." *Journal of Aircraft* 51 (5): 1439-1454. https://doi.org/10.2514/1.C032313.

Paulson, J.W., Jr. and Kjelgaard, S. O. 1982. *An experimental and theoretical investigation of thick wings at various sweep angles in and out of ground effect*. NASA Langley Research Center Hampton, NASA-TP-2068.

Pereira, J. L. 2011. "Experimental investigation of tip vortex control using a half delta shaped tip strake. " Ph.D. Thesis, Montreal: McGill University.

Qu, Qiulin, Liewei Huang, Peiqing Liu, and Ramesh K. Agarwal. 2016. "Near-field Wingtip Vortex Characteristics of a Rectangular Wing in Ground Effect." In *54th AIAA Aerospace Sciences Meeting*, In AIAA SciTech Forum. American Institute of Aeronautics and Astronautics.

Qu, Qiulin, Wei Wang, Peiqing Liu, and Ramesh K. Agarwal. 2015. "Airfoil Aerodynamics in Ground Effect for Wide Range of Angles of Attack." *AIAA Journal* 53 (4): 1048-1061. https://doi.org/10.2514/1.J053366.

Ramaprian, B. R., and Youxin Zheng. 1997. "Measurements in Rollup Region of the Tip Vortex from a Rectangular Wing." *AIAA Journal* 35 (12): 1837-1843. https://doi.org/10.2514/2.59.

Ramasamy, M., B. Johnson, T. Huismann and J. D. Leishman. 2007. *An improved method for estimating turbulent vortex flow properties from stereoscopic DPIV measurements*. Moffet Field: Ames Research Center.

Shi, Xiaohang, Qiulin Qu, Peiqing Liu, Yiyuan Xun, Chen Bu, and Hao Chen. 2022. "Feasibility Analysis of Fixed Plates in Chord-Dominated Static Ground Effect Wind-Tunnel Experiment." *AIAA Journal* 60 (9): 5286-5298. https://doi.org/10.2514/1.J062014.

Skinner, S. N., R. B. Green, and H. Zare-Behtash. 2020. "Wingtip vortex structure in the near-field of swept-tapered wings." *Physics of Fluids* 32 (9): 095102. https://doi.org/10.1063/5.0016353.

Smith, S. C.. 1996. *A Computational and Experimental Study of Nonlinear Aspects of Induced Drag.* Moffet Field: Ames Research Center, NASA-TP-3598.

Thomas, Adrian L. R., and Graham K. Taylor. 2001. "Animal Flight Dynamics I. Stability in Gliding Flight." *Journal of Theoretical Biology* 212 (3): 399-424. https://doi.org/10.1006/jtbi.2001.2387.

Tremblay-Dionne, V., and T. Lee. 2020. "Discrepancy in the Aerodynamic Property and Flowfield of a Symmetric Airfoil Produced by the Stationary and Moving Ground Effect." *Journal of Fluids Engineering* 143 (2). https://doi.org/10.1115/1.4048290.

Vijgen, P. M. H. W., C. P. van Dam, and B. J. Holmes. 1989. "Sheared wing-tip aerodynamics - Wind-tunnel and computational investigation." *Journal of Aircraft* 26 (3): 207-213. https://doi.org/10.2514/3.45747.

Wenger, Christian W., and William J. Devenport. 1999. "Seven-Hole Pressure Probe Calibration Method Utilizing Look-Up Error Tables." *AIAA Journal* 37 (6): 675-679. https://doi.org/10.2514/2.794.

Westphal, Russell, and Rabindra Mehta. 1987. "Interaction of an oscillating vortex with a turbulent boundary layer." In *19th AIAA, Fluid Dynamics, Plasma Dynamics, and Lasers Conference*, In Fluid Dynamics and Co-located Conferences. American Institute of Aeronautics and Astronautics.

Yang, Zhigang, and Yang, Wei. 2010. "Complex Flow for Wing-in-ground Effect Craft with Power Augmented Ram Engine in Cruise." *Chinese Journal of Aeronautics* 23 (1): 1-8. https://doi.org/10.1016/S1000-9361(09)60180-1.

Zhang, Kai, Shelby Hayostek, Michael Amitay, Anton Burtsev, Vassilios Theofilis, and Kunihiko Taira. 2020. "Laminar separated flows over finite-aspect-ratio swept wings." *Journal of Fluid Mechanics* 905: R1. https://doi.org/10.1017/jfm.2020.778.

Zhang, Kai, and Kunihiko Taira. 2022. "Laminar vortex dynamics around forward-swept wings." *Physical Review Fluids* 7 (2): 024704. https://doi.org/10.1103/PhysRevFluids.7.024704.

Zhang, Zeyu, Dong Li, Jinxin Zhou, Weijun Pan, Ziming Xu, and Jinyan Cai. 2022. "Numerical simulation of wake vortex for the flight near the ground with different boundary conditions." *Engineering Applications of Computational Fluid Mechanics* 16 (1): 484-500. https://doi.org/10.1080/19942060.2022.2026819.

Zheng, Youxin and B.R. Ramaprian. 1993. *An Experimental Study of Wing Tip Vortex in the Near Wake of a Rectangular Wing*. WASHINGTON STATE UNIVERSITY, MME-TF-93-1.

Appendix A: Force Balance Calibration Procedure

The calibration procedure of the force balance summarized in this appendix, is referenced from the documentation of the previous research thesis carried out in the same laboratory using the same equipment (Pereira 2011).

The force balance used in this study consisted of two orthogonally set linear velocity differential transformers (LVDT). The LVDTs were set in directions normal (N-direction) and tangential (T direction) to the wing chord, as seen in Fig. 3-4. Figure 3-3 shows the set-up of the force balance below the wind tunnel. From these figures, it is apparent that any force acting on the wing was imparted through the mounting shaft, which was mounted on the sensor plate. This sensor plate was supported by two sets of cantilever-type spring steel flexures that deflected as the force was applied to the sensor plate. In the N-direction, the flexures had a thickness of 0.9 mm, while the flexures in the T-direction were much thinner at 0.3 mm. These two sets were chosen to account for the fact that the normal force is generally one or two orders of magnitude higher than the tangential force. The sensor plate was also connected to the LVDTs, which converted the deflection into a voltage. The advantage of using an LVDT is its precision and high resolution, as it is able to sense very small deflections. The LVDT itself consists of three coils and a ferromagnetic core. The central (or primary) coil induces a magnetic field in the core. As the core moves along an axis, it induces a voltage in the secondary coils, much in the same way a solenoid works. The difference in the voltages induced by each secondary coil is the output, which varies linearly with displacement. Accordingly, calibration of the force balance required accurate calibration of each LVDT through its linear range. For the force balance measurements, the wing was mounted at its quarter chord. This, unfortunately, did not correspond to the center of gravity on the wing. In order to compensate for this imbalance, the wing was mounted on the force balance during all calibration.

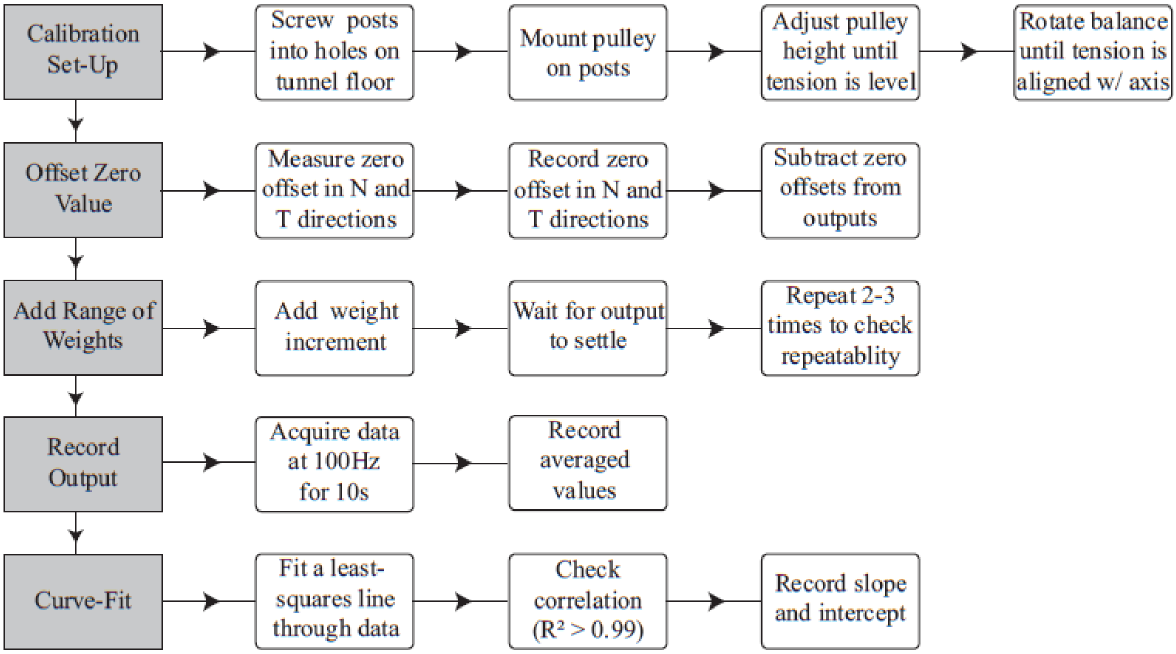

Figure A-1 Flow chart of the force balance calibration procedure

Figure A-1 is the flowchart of the steps involved in the force balance calibration. For the calibration phase, known weights were used to create a tension force along either the normal or tangential directions. The weights were hung over a pulley system and attached to the wing mounting shaft via aluminum wire. The aluminum wire was found to provide sufficient strength in order to support the various weights and remain rigid while having a minimal weight so as to not overwhelm for low weights. During calibration, careful attention was given to ensuring that the tension was perfectly aligned with the LVDT being calibrated. In order to achieve this, the pulleys were attached to posts which were screwed into holes aligned with the freestream on the tunnel floor. The height of the pulley was first set using both a height gauge and bubble-type level to ensure that the tensioned string was level. The pulley height was finely adjusted until the output in the particular direction was maximized. In the yaw direction, the force balance was rotated on the turntable until the output along the axis being calibrated was maximized, and the output along the orthogonal axis remained unchanged as weight was added. This portion of the calibration procedure was found to be the most time-consuming. However, once set up, weights ranging from 10g to 1kg (0.1N to 9.8N) were used to calibrate each LVDT. It was also found that the calibration curve was similar but not exactly the same in the positive and negative N directions. Thus three calibration curves (two in the N-direction, one in the T-direction) were obtained and are plotted in Fig. A-2, showing that the curves are linear to within 1%. The sensitivity of the curves was 120, 93 and 0.6 Newtons/Volt in the positive N-direction, negative N-direction and positive T-direction, respectively.

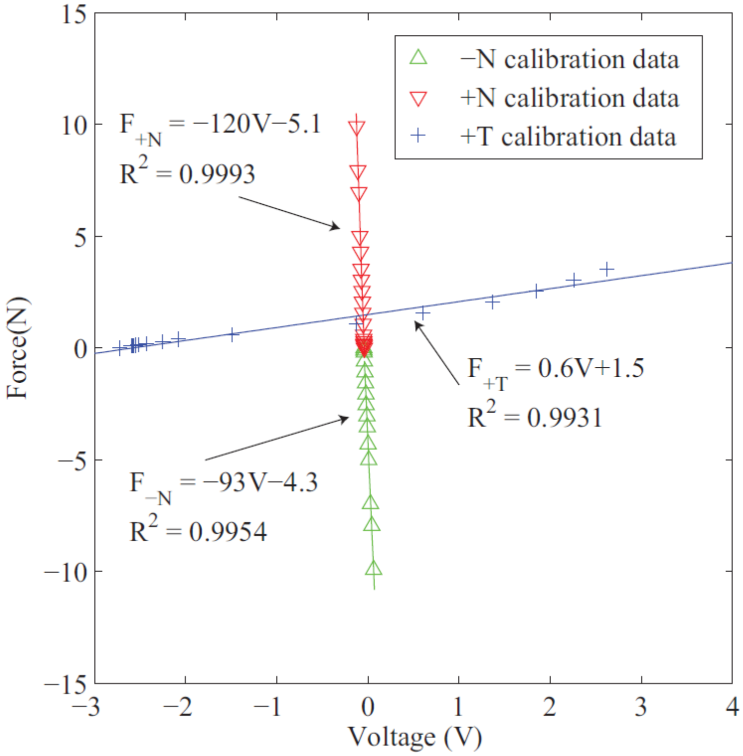

Figure A-2 Force balance calibration fitted curves.

Appendix B: C_{Di} Calculation

The lift-induced drag $C_{Di} = D_i/½\rho U^2 S$ was calculated based on the method introduced by Maskell (1973), and the calculation process was referenced from the previous thesis work performed in the same laboratory (Pereria 2010).

Maskell (1973) simplified the drag into the following form:

$$D = \iint_S (p_1 - p_2)dS + \frac{1}{2}\rho \iint_S (u^* - u)(u^* + u - 2u_\infty)dS + \frac{1}{2}\rho \iint_S (v^2 + w^2 - u'^2)dS \tag{B-1}$$

$$u^{*2} = u^2 + \frac{2}{\rho}(p_1 - p_2) \tag{B-2}$$

where p_1 and p_2 are the static pressure at the upstream and downstream planes of the control volume, S is the surface area of the cross-plane, u, v, w are the velocity component in the freestream, $u' = u^* - u_\infty$ is the perturbation velocity. The first term in equation (B-1) is the pressure drag, the second term is the profile drag, and the third term is the induced drag.

Maskell interpreted the velocity perturbation term in the induced drag relation as a wake blockage correction factor. If the wind tunnel walls are far away from each other, the u'^2 term becomes negligible, which simplifies the induced drag to the following:

$$D_i = \frac{1}{2}\rho \iint_S (v^2 + w^2)dS \tag{B-3}$$

where the integral becomes small outside the vortical wake region. The v and w components of the velocity can be written in terms of the stream function ψ and velocity potential ϕ as the following:

$$v = \frac{\partial\phi}{\partial y} + \frac{\partial\psi}{\partial z} \tag{B-4}$$

$$w = \frac{\partial\phi}{\partial z} - \frac{\partial\psi}{\partial y} \tag{B-5}$$

giving the lift-induced drag in the form:

$$D_i = \frac{1}{2}\rho \iint_S \left(\frac{\partial\phi}{\partial y} + \frac{\partial\psi}{\partial z}\right)^2 + \left(\frac{\partial\phi}{\partial z} - \frac{\partial\psi}{\partial y}\right)^2 dS \tag{B-6}$$

Maskell demonstrated that the equation (B-6) could be further reduced to the following using Green's theorem and divergence.

$$D_i = \frac{1}{2}\rho \iint_{wake} \psi\zeta - \phi\sigma \, dS \tag{B-7}$$

where ζ is the vorticity and σ is the source term. The boundary conditions applied to equation (B-7) are:

1. Tunnel walls are streamlined, $\psi(wall) = 0$
2. No flow through the walls, $\frac{\partial\phi}{\partial n} = 0$

Therefore, if the ψ,ζ,ϕ, and σ can be determined at each point (i,j) in the vortical wake, one can then calculate the induced drag. In this thesis project, the vorticity and source terms were calculated based on the velocity field measured by the seven-holes pressure probe via the centred-difference formula:

$$\zeta_{i,j} = \frac{\Delta w}{\Delta y} - \frac{\Delta v}{\Delta z} = \left(\frac{w_{i-1,j} - w_{i+1,j}}{2\eta}\right) - \left(\frac{v_{i,j+1} - v_{i,j-1}}{2\eta}\right) \tag{B-8}$$

$$\sigma_{i,j} = \frac{\Delta v}{\Delta y} + \frac{\Delta w}{\Delta z} = \left(\frac{v_{i-1,j} - v_{i+1,j}}{2\eta}\right) - \left(\frac{v_{i,j+1} - v_{i,j-1}}{2\eta}\right) \tag{B-9}$$

where $\eta = \Delta y = \Delta z$, $i = 2,3, \dots, n-1$, $j = 2,3, \dots, m-1$.

The stream function and velocity potential can then be calculated using Poisson's equation and centred-difference formula:

$$\zeta_{i,j} = -\nabla^2 \psi_{i,j} \approx -\frac{1}{\eta^2}(\psi_{i+1,j} + \psi_{i-1,j} - 4\psi_{i,j} + \psi_{i,j+1} + \psi_{i,j-1}) \tag{B-10}$$

$$\sigma_{i,j} = \nabla^2 \phi_{i,j} \approx \frac{1}{\eta^2}(\phi_{i+1,j} + \phi_{i-1,j} - 4\phi_{i,j} + \phi_{i,j+1} + \phi_{i,j-1}) \tag{B-11}$$

Along the edge of the control volume, the following were applied accordingly:

$$\zeta_{i,2} \approx -\frac{1}{\eta^2}(\psi_{i+1,2} + \psi_{i-1,2} - 4\psi_{i,2} + \psi_{i,3}) \tag{B-12}$$

$$\sigma_{i,2} \approx \frac{1}{\eta^2}(\phi_{i+1,2} + \phi_{i-1,2} - 3\phi_{i,2} + \phi_{i,3}) \tag{B-13}$$

$$\zeta_{i,m-1} \approx -\frac{1}{\eta^2}(\psi_{i+1,m-1} + \psi_{i-1,m-1} - 4\psi_{i,m-1} + \psi_{i,m-2}) \tag{B-14}$$

$$\sigma_{i,m-1} \approx \frac{1}{\eta^2}(\phi_{i+1,m-1} + \phi_{i-1,m-1} - 3\phi_{i,m-1} + \phi_{i,m-2}) \tag{B-15}$$

$$\zeta_{n-1,j} \approx -\frac{1}{\eta^2}(\psi_{n-2,j} - 4\psi_{n-1,j} + \psi_{n-1,j+1} + \psi_{n-1,j-1}) \tag{B-16}$$

$$\sigma_{n-1,j} \approx \frac{1}{\eta^2}(\phi_{n-2,j} - 3\phi_{n-1,j} + \phi_{n-1,j+1} + \phi_{n-1,j-1}) \tag{B-17}$$

$$\zeta_{2,j} \approx -\frac{1}{\eta^2}(\psi_{3,j} - 4\psi_{2,j} + \psi_{2,j+1} + \psi_{2,j-1}) \tag{B-18}$$

$$\sigma_{2,j} \approx \frac{1}{\eta^2}(\phi_{3,j} - 3\phi_{2,j} + \phi_{2,j+1} + \phi_{2,j-1}) \tag{B-19}$$

Equations (B-10)-(B-19) then formed a system of equations of $(n-2) \times (m-2)$ with $(n-2) \times (m-2)$ unknowns, which can be expressed as $A\vec{x} = \vec{b}$. A is a $(n-2) \times (m-2)$ by $(n-2) \times (m-2)$ matrix of coefficient, $\vec{x}$ (unknowns) is the vector of ψ or ϕ and $\vec{b}$ (knowns) is the vector of σ or ζ. The unknowns can be solved easily by calculating the inverse of A and multiplying it by $\vec{b}$. However, due to the massive scan area and high grid resolution, the size of matrix A quickly grew to a large size and can not be inverted by a laptop. To speed up the process, an iterative successive over-relaxation (SOR) technique based on the Gauss-Seidel method was used. The process starts with an initial estimate of the solution, which was calculated at a coarser resolution of 25.4 cm resulting in a 1632×1632 A matrix. The A matrix was inverted and multiplied by $\vec{b}$ to obtain a close initial guess. In order to accelerate the rate of convergence, an over-relaxation parameter was used:

$$\omega = \frac{4}{\sqrt{2 + \left[4 - \cos\left(\frac{\pi}{m}\right) + \cos\left(\frac{\pi}{n}\right)\right]^2}} \tag{B-20}$$

The vector of unknowns $\vec{x}$ was then solved using:

$$x_i = (1-\omega)XO_i + \frac{\omega\left(-\sum_{j=1}^{i=1} a_{i,j}x_j - \sum_{j=i+1}^{n\times m} a_{i,j}XO_j + b_i\right)}{a_{i,j}} \tag{B-21}$$

where x_i is the value of $\vec{x}$, XO_i is the initial guess, $a_{i,j}$ is the coefficient in the A matrix, and b_i is the value in $\vec{b}$. The iteration was repeated until the difference between the runs was less than 0.01. Difference tolerance values were selected; however, only a 0.5% difference was observed. Therefore, the 0.01 tolerance was selected to minimize the run time. Once the unknowns $\vec{x}$ were solved, the induced drag can then be calculated as the following:

$$D_i \approx \frac{\rho}{2}\sum_{i=2}^{n-1}\sum_{j=2}^{m-1}\left(\psi_{i,j}\zeta_{i,j} - \phi_{i,j}\sigma_{i,j}\right)\eta^2$$

(B-22)

Appendix C: Circulation Determination of the Multiple Vortex System in Close Ground Proximity

Outside the ground effect, the total circulation Γ_o of the tip vortex was determined based on the radial distribution of the Γ starting from the vortex core where the peak vortex strength was located (Figs. C-1a-b). The total circulation Γ_o plateaued when it reached the outer region. Consequently, the asymptotic value was set as the total circulation Γ_o.

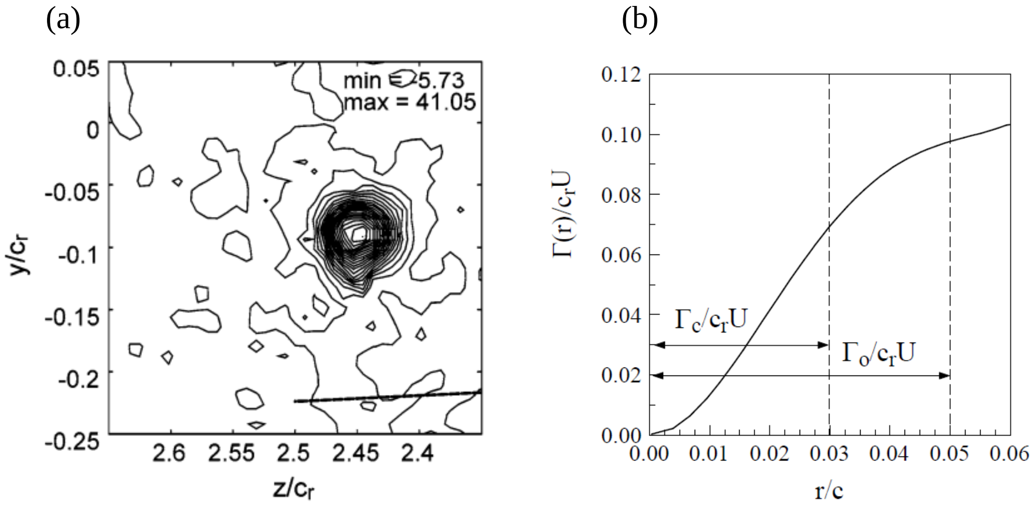

Figure C-1 (a) Iso-$\zeta c_r/U$ *contour of the tip vortex (BSW) at* $\alpha = 8^o$ *outside ground effect and (b) the radial circulation distribution.*

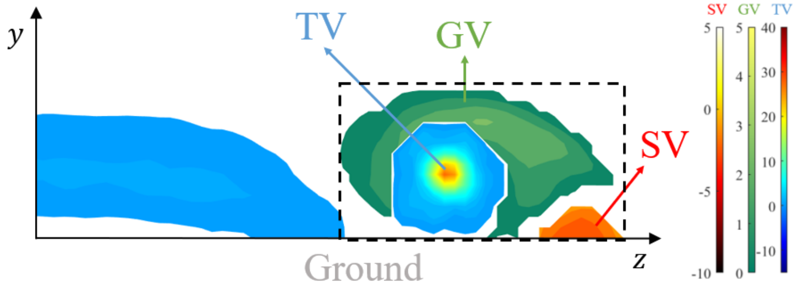

Figure C-2 Multiple-vortex system for BSW at $\alpha = 8.5°$ *and* $h/c_r = 11.25\%$

In ground effect, the ground vortex and secondary vortex wrapped around the tip vortex and distorted its shape. The total circulation distribution of the tip vortex in the radial direction did not level off. Therefore, a modified approach was introduced as the following. When calculating the circulation for each vortex, the first step is to identify the border or region of each vortex. Shown in Table C-1 is the matrix containing the vorticity inside the dashed line region in Fig. C-2. The horizontal axis (A-AB) corresponded to the axis in the spanwise direction, and the vertical axis (1-16) corresponded to the axis in the vertical direction. Each cell contained the iso-vorticity value at each grid location in Fig. C-2. The empty cell is where the absolute vorticity level was lower than a threshold of 0.05 and was, therefore, ignored. The secondary vortex was readily identified as it contained negative vorticity compared to the ground and tip vortices.

Table C-1 Iso-$\zeta c_r/U$ matrix of the multiple-vortex system. Blue and red lines indicate the tip vortex and secondary vortex region, respectively.

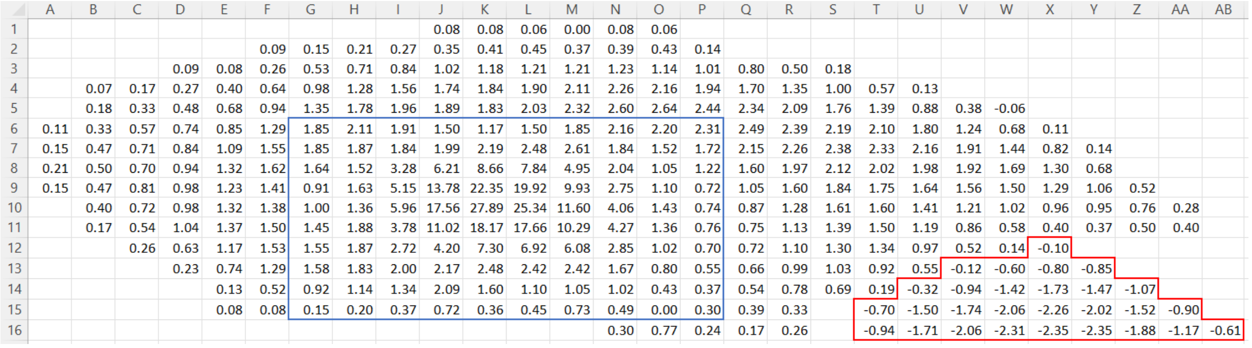

	A	B	C	D	E	F	G	H	I	J	K	L	M	N	O	P	Q	R	S	T	U	V	W	X	Y	Z	AA	AB
1										0.08	0.08	0.06	0.00	0.08	0.06													
2						0.09	0.15	0.21	0.27	0.35	0.41	0.45	0.37	0.39	0.43	0.14												
3				0.09	0.08	0.26	0.53	0.71	0.84	1.02	1.18	1.21	1.21	1.23	1.14	1.01	0.80	0.50	0.18									
4		0.07	0.17	0.27	0.40	0.64	0.98	1.28	1.56	1.74	1.84	1.90	2.11	2.26	2.16	1.94	1.70	1.35	1.00	0.57	0.13							
5		0.18	0.33	0.48	0.68	0.94	1.35	1.78	1.96	1.89	1.83	2.03	2.32	2.60	2.64	2.44	2.34	2.09	1.76	1.39	0.88	0.38	-0.06					
6	0.11	0.33	0.57	0.74	0.85	1.29	1.85	2.11	1.91	1.50	1.17	1.50	1.85	2.16	2.20	2.31	2.49	2.39	2.19	2.10	1.80	1.24	0.68	0.11				
7	0.15	0.47	0.71	0.84	1.09	1.55	1.85	1.87	1.84	1.99	2.19	2.48	2.61	1.84	1.52	1.72	2.15	2.26	2.38	2.33	2.16	1.91	1.44	0.82	0.14			
8	0.21	0.50	0.70	0.94	1.32	1.62	1.64	1.52	3.28	6.21	8.66	7.84	4.95	2.04	1.05	1.22	1.60	1.97	2.12	2.02	1.98	1.92	1.69	1.30	0.68			
9	0.15	0.47	0.81	0.98	1.23	1.41	0.91	1.63	5.15	13.78	22.35	19.92	9.93	2.75	1.10	0.72	1.05	1.60	1.84	1.75	1.64	1.56	1.50	1.29	1.06	0.52		
10		0.40	0.72	0.98	1.32	1.38	1.00	1.36	5.96	17.56	27.89	25.34	11.60	4.06	1.43	0.74	0.87	1.28	1.61	1.60	1.41	1.21	1.02	0.96	0.95	0.76	0.28	
11		0.17	0.54	1.04	1.37	1.50	1.45	1.88	3.78	11.02	18.17	17.66	10.29	4.27	1.36	0.76	0.75	1.13	1.39	1.50	1.19	0.86	0.58	0.40	0.37	0.50	0.40	
12			0.26	0.63	1.17	1.53	1.55	1.87	2.72	4.20	7.30	6.92	6.08	2.85	1.02	0.70	0.72	1.10	1.30	1.34	0.97	0.52	0.14	-0.10				
13				0.23	0.74	1.29	1.58	1.83	2.00	2.17	2.48	2.42	2.42	1.67	0.80	0.55	0.66	0.99	1.03	0.92	0.55	-0.12	-0.60	-0.80	-0.85			
14					0.13	0.52	0.92	1.14	1.34	2.09	1.60	1.10	1.05	1.02	0.43	0.37	0.54	0.78	0.69	0.19	-0.32	-0.94	-1.42	-1.73	-1.47	-1.07		
15					0.08	0.08	0.15	0.20	0.37	0.72	0.36	0.45	0.73	0.49	0.00	0.30	0.39	0.33		-0.70	-1.50	-1.74	-2.06	-2.26	-2.02	-1.52	-0.90	
16														0.30	0.77	0.24	0.17	0.26		-0.94	-1.71	-2.06	-2.31	-2.35	-2.35	-1.88	-1.17	-0.61

Meanwhile, even though the ground vortex wrapped around the tip vortex, the tip vortex remained distinguishable with a nearly circular shape, which implied that the vorticity distribution inside the tip vortex continued to behave similarly to the one outside ground effect with the vortex strength peaked at the center and decreasing in the radial direction. As can be seen in Table C-1, the vorticity peaked at K-10 ($\zeta_{peak}c_r/U = 27.89$) and, consequently, K-10 is the core of the tip vortex. Passing through the core, two core axes can be defined: core y-axis (column K) and core z-axis (row 10). Since the vortex strength inside the tip vortex should continuously decrease in the radial and outboard direction, by examining each data point along the two core axes, four borders can be identified for the tip vortex (indicated by the blue lines). The tip vortex region can be further refined by comparing each grid with its neighbour in the inboard direction. The strength of each grid must be weaker than its adjacent in the radial and inboard direction. For example, J-8 was smaller than J-9, K-8 and K-9 and was thus included in the tip vortex, whereas H-7 was larger than H-8, it therefore should be excluded and added to the ground vortex. Table C-2 shows the refined tip vortex region and, by subtracting the tip vortex and secondary vortex from Table C-1, the remaining will be the ground vortex as shown in Table C-2.

Table C-2 Refined tip vortex matrix

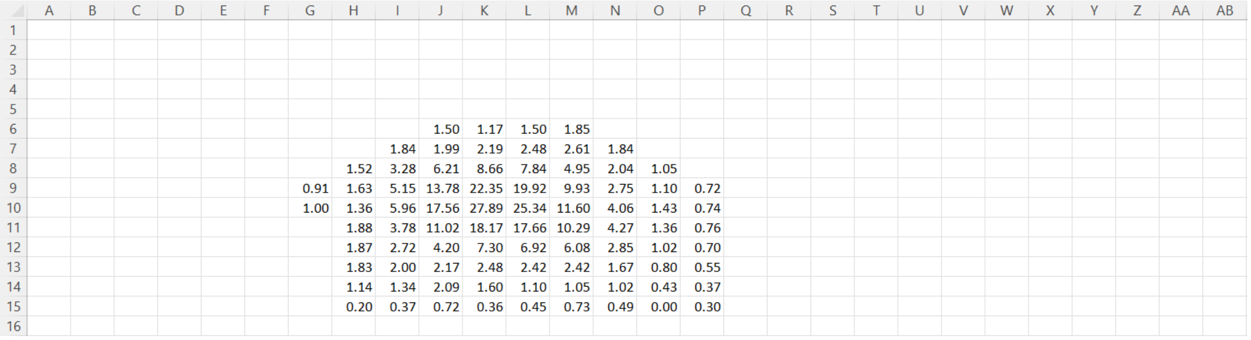

	A	B	C	D	E	F	G	H	I	J	K	L	M	N	O	P	Q	R	S	T	U	V	W	X	Y	Z	AA	AB
1																												
2																												
3																												
4																												
5																												
6										1.50	1.17	1.50	1.85															
7									1.84	1.99	2.19	2.48	2.61	1.84														
8								1.52	3.28	6.21	8.66	7.84	4.95	2.04	1.05													
9							0.91	1.63	5.15	13.78	22.35	19.92	9.93	2.75	1.10	0.72												
10							1.00	1.36	5.96	17.56	27.89	25.34	11.60	4.06	1.43	0.74												
11								1.88	3.78	11.02	18.17	17.66	10.29	4.27	1.36	0.76												
12								1.87	2.72	4.20	7.30	6.92	6.08	2.85	1.02	0.70												
13								1.83	2.00	2.17	2.48	2.42	2.42	1.67	0.80	0.55												
14								1.14	1.34	2.09	1.60	1.10	1.05	1.02	0.43	0.37												
15								0.20	0.37	0.72	0.36	0.45	0.73	0.49	0.00	0.30												
16																												

Table C-3 Refined ground vortex matrix

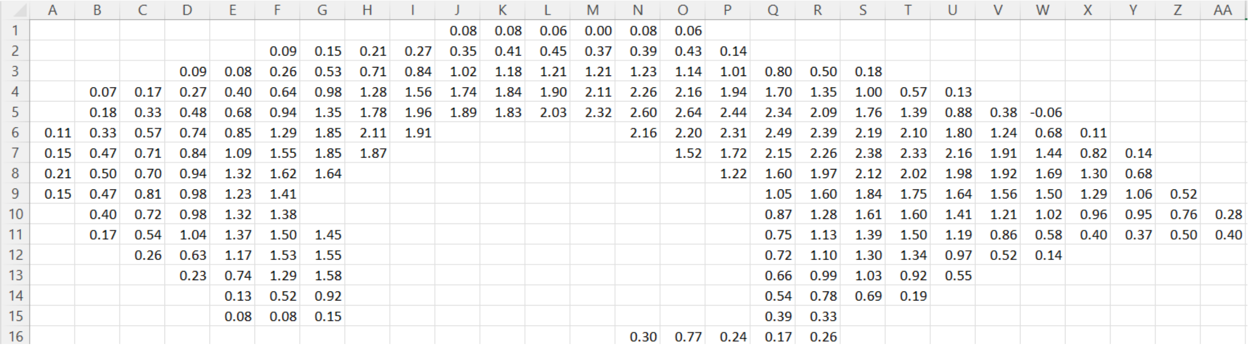

	A	B	C	D	E	F	G	H	I	J	K	L	M	N	O	P	Q	R	S	T	U	V	W	X	Y	Z	AA
1										0.08	0.08	0.06	0.00	0.08	0.06												
2						0.09	0.15	0.21	0.27	0.35	0.41	0.45	0.37	0.39	0.43	0.14											
3				0.09	0.08	0.26	0.53	0.71	0.84	1.02	1.18	1.21	1.21	1.23	1.14	1.01	0.80	0.50	0.18								
4		0.07	0.17	0.27	0.40	0.64	0.98	1.28	1.56	1.74	1.84	1.90	2.11	2.26	2.16	1.94	1.70	1.35	1.00	0.57	0.13						
5		0.18	0.33	0.48	0.68	0.94	1.35	1.78	1.96	1.89	1.83	2.03	2.32	2.60	2.64	2.44	2.34	2.09	1.76	1.39	0.88	0.38	-0.06				
6	0.11	0.33	0.57	0.74	0.85	1.29	1.85	2.11	1.91					2.16	2.20	2.31	2.49	2.39	2.19	2.10	1.80	1.24	0.68	0.11			
7	0.15	0.47	0.71	0.84	1.09	1.55	1.85	1.87							1.52	1.72	2.15	2.26	2.38	2.33	2.16	1.91	1.44	0.82	0.14		
8	0.21	0.50	0.70	0.94	1.32	1.62	1.64									1.22	1.60	1.97	2.12	2.02	1.98	1.92	1.69	1.30	0.68		
9	0.15	0.47	0.81	0.98	1.23	1.41											1.05	1.60	1.84	1.75	1.64	1.56	1.50	1.29	1.06	0.52	
10		0.40	0.72	0.98	1.32	1.38											0.87	1.28	1.61	1.60	1.41	1.21	1.02	0.96	0.95	0.76	0.28
11		0.17	0.54	1.04	1.37	1.50	1.45										0.75	1.13	1.39	1.50	1.19	0.86	0.58	0.40	0.37	0.50	0.40
12			0.26	0.63	1.17	1.53	1.55										0.72	1.10	1.30	1.34	0.97	0.52	0.14				
13				0.23	0.74	1.29	1.58										0.66	0.99	1.03	0.92	0.55						
14					0.13	0.52	0.92										0.54	0.78	0.69	0.19							
15					0.08	0.08	0.15										0.39	0.33									
16														0.30	0.77	0.24	0.17	0.26									

However, in extreme ground proximity (e.g., $h/c_r = 6.5\%$; Fig. C-3), when the ground vortex almost completely merged into the tip vortex, the border between the ground vortex and the tip vortex became vague. In this case, all the positive vorticity inside the dash line region was simply treated as tip vortex since the remaining ground vortex can hardly be discriminated from the tip vortex.

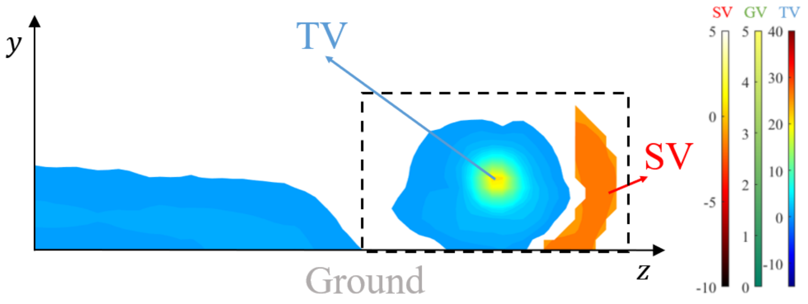

Figure C-3 Multiple-vortex system for BSW at $\alpha = 8.5^o$ and $h/c_r = 6.5\%$